DELAWARE BAY: HYDRODYNAMICS AND SEDIMENT TRANSPORT IN THE ANTHROPOCENE

by

LUIS FERNANDO PAREJA ROMAN

A dissertation submitted to the

School of Graduate Studies

Rutgers, The State University of New Jersey

In partial fulfillment of the requirements

For the degree of

Doctor of Philosophy

Graduate Program in Oceanography

Written under the direction of

Robert J. Chant

and approved by

_____

_____

_____

_____

New Brunswick, New Jersey

October 2019

ABSTRACT OF THE DISSERTATION

DELAWARE BAY: HYDRODYNAMICS AND SEDIMENT TRANSPORT IN THE ANTHROPOCENE

by LUIS FERNANDO PAREJA ROMAN

Dissertation Director:

Robert J. Chant

One of the main characteristics of the Anthropocene in estuaries is the modification of basin morphology through the creation of navigational channels. Although the benefits of these channels are evident from an economic perspective, the associated response of the wave climate, tidal flows, salinity intrusion, and sediment dynamics is scarcely studied. Since estuaries can be classified in several categories depending on parameter spaces dictated by hydrodynamic and morphological features, it is key to assess how the barotropic, baroclinic, and sediment dynamics respond to channel modifications in multiple urbanized systems. This dissertation focuses on the impact of channel deepening on waves, tides, and sediment transport in urbanized estuaries. The study region here is the Delaware Estuary, which has been dredged for over a century to ensure navigation into the ports of Wilmington, Philadelphia, and Trenton.

First, we explore the impact of locally generated wind waves on the momentum budget and subtidal exchange in the bay. We use a numerical model to diagnose the role of wind waves on surface drag, momentum budget, and residual circulation in the estuary. Model

results reveal that wave induced forces (Stokes-Coriolis, breaking, and vortex forces) did not significantly add to the mean momentum budget during a typical storm. However, when we accounted for the spatially variable wave height and age in the wind stress formulation, and the wave-induced Stokes drift, we found that the subtidal bay-ocean exchange increased by about 30%. We also highlight that wind and wave direction are also critical for the magnitude of the depth-integrated exchange. Part of this study on waves included an adjustment of the wave model to prevent whitecapping wave dissipation from creating breaking forces since that contribution is already included in the wind stress. Results from this part are generalizable to young seas in estuaries where the wave field is modulated by topography.

Second, we examine how historical channel deepening altered barotropic dynamics in the estuary and tidal river. Model results with historical and modern bathymetry reveal a doubling in tidal range near the head of the tides, consistent with a reduction in hydraulic drag in the shipping channel and relatively unchanged width convergence. Tidal current amplitude along the channel doubled in some areas and were strongly modulated by undulations in channel topography. Channel deepening also increased the tidal phase speed, with implications for the arrival time of high water in the system, especially in the tidal river where high water arrives about an hour earlier now than in the mid 1800s. In terms of wave dynamics, the tidal wave became more progressive after deepening and tidal energy fluxes increased. We also found that the tidal amplification caused by a doubling in channel depth is similar to the projected change in tides under 1 m of sea level rise and shoreline hardening reported recently by other authors.

The last part is a modeling study on the effect of channel deepening on suspended sediment concentration and fluxes (pumping and mean advection). Since sediment dynamics are closely tied to density-driven circulation, we briefly examined the baroclinic response to channel deepening under mean river discharge. The model revealed that the salt intrusion increased by a factor of 1.3 and that the magnitude of the exchange flow increased only locally in the lower bay by no more than 25%. Areas of enhanced sediment trapping were located in the saline reaches of each modeled scenario (historical and modern), and at lateral bathymetric transitions from channels to shoals due to the influence of salinity fronts. Channel deepening led to the landward migration of these trapping zones, consistent with the increase in salt intrusion. The mean advection of sediment closely mimics the residual circulation patterns in both the stratified and fresh segments of the system, while pumping fluxes were strongly landward in both scenarios but especially in the modern one due to the velocity asymmetry caused by tidal distortion.

ACKNOWLEDGMENTS

I would like to thank the National Science Foundation (Coastal Science, Engineering, and Sustainability Program, grant #1325136.) and the Department of Marine and Coastal Sciences at Rutgers University for support through graduate and teaching assistantships and also for the opportunity to attend conferences and professional development events. I have been fortunate to share this journey with people of outstanding human and professional qualities: friends and colleagues I met in the program and that I will continue to cherish after my stay at Rutgers. In my motivation essay for admission into the Ph.D., I wrote that the mentoring of Bob Chant and John Wilkin would be challenging and enjoyable. Five years later, not only that proved to be true but I grew personally and professionally in ways I had not anticipated. I also want to acknowledge Scott Glenn and David Ralston who provided valuable guidance, quality time, and good humor especially in critical moments of the Ph.D. process. The Ocean Modeling Group (Alex, Chuning, Jack, Julia, Piero, Eli, and Phil) provided friendship and technical help over the years. I also want to thank colleagues in the broader oceanographic community who were incredibly supportive, especially during my research on wind waves and air-sea interaction in estuaries: Maitane Olabarrieta, Nirnimesh Kumar, Yusuke Uchiyama, John Warner, Greg Gerbi, and Melissa Moulton. Thanks also to Rocky Geyer and again to David Ralston for welcoming me at the Woods Hole Oceanographic Institution for a brief visit to work on my research proposal. Jia-Lin (Julie) Chen, Neil Ganju, and Christopher Sommerfield (and his group) retrieved and digitized historical and modern depth soundings of the Delaware Estuary and interpolated them on a model grid. This thesis would not have been possible without their valuable help.

Last but not least, thanks to my mother, father, sister, and to my friends from Colombia and United States for their continuous patience and support. They listened to long ramblings and rants on sediment transport, coastal storms, and vintage maps over the course of five years. I dedicate this work to them.

TABLE OF CONTENTS

ABSTRACT OF THE DISSERTATION ii

ACKNOWLEDGMENTS v

TABLE OF CONTENTS vii

LIST OF FIGURES x

LIST OF TABLES xvi

Chapter 1 – Introduction 1

1.1 Estuaries in the Anthropocene 1

1.2 The Delaware Estuary 2

1.3 Thesis Goals 7

Chapter 2 - Effects of Locally Generated Wind Waves on the Momentum Budget and Subtidal Exchange in Delaware Bay 9

2.1 Abstract 9

2.2 Introduction 10

2.2.1 Surface Layer 11

2.2.2 Bottom Layer 15

2.2.3 Wave-induced forces in the water column 15

2.2.4 Study goals and approach 16

2.3 Observations of Winds and Waves 18

2.4 Modeling Framework....21
2.4.1 Coupled Modeling System....21
2.4.2 Idealized simulations and model evaluation....24
2.4.3 Numerical experiments with realistic bathymetry....29
2.5 Results and discussion....31
2.5.1 Wind waves and surface stress....32
2.5.2 Wind waves and bottom stress....39
2.5.3 Water column momentum budget....41
2.5.4 Subtidal exchange....46
2.6 Summary and conclusions....50
Chapter 3 - Impact of Historical Channel Deepening on Tidal Hydraulics in the Delaware Estuary....53
3.1 Abstract....53
3.2 Introduction....53
3.2.1 Tidal amplification, damping, and distortion....56
3.2.2 Tidal energy flux....58
3.2.3 Study goals....59
3.3 Methods and hydrodynamic model....60
3.4 Results and discussion....62
3.4.1 Channel deepening, tidal elevation amplitude, and asymmetries....63
3.4.2 Channel deepening and tidal currents....68
3.4.3 Analytical framework for tidal elevation....71
3.4.4 Elevation-velocity phase and energy fluxes....74

3.5 Summary and conclusions 78

Chapter 4 - Changes to Suspended Sediment Concentration and Trapping in the Delaware Estuary Associated with Dredging 80

4.1 Abstract 80

4.2 Background 80

4.2.1 Dredging and Sediment Dynamics in Estuaries 82

4.2.2 Salinity and SSC in the Delaware Estuary 84

4.3 Methods 85

4.3.1 Coupled Hydrodynamic and Sediment model 85

4.3.2 Sediment flux decomposition 86

4.4 Results and discussion 87

4.4.1 Effect of dredging on along-channel salinity, bed stress, and SSC 88

4.4.2 Dredging and cross-estuary patterns of SSC, erosion, and deposition 91

4.4.3 Impact of dredging on the advection and tidal pumping of sediment 96

4.5 Summary and conclusions 101

Chapter 5 - Conclusions 102

Acknowledgement of Previous Publications 104

References 105

LIST OF FIGURES

Figure 1.1. (a) Delaware Bay bathymetry in meters for the historical scenario (1848) and along-thalweg coordinates from the mouth to the head of tides near Trenton. (b) Highlight of deepened areas with respect to the digitized bathymetry from 2014. The location of cities, rivers, and states are also shown.....4

Figure 1.2. (a) Thalweg and mean depth in the historical and modern Delaware Estuary, starting at the mouth near Lewes (km 0) to the head of the tides near Trenton (km 190). (b) Changes in basin hypsometry for the lower bay (Lewes to Bombay Hook, 'BH') and in the upper estuary and tidal river (BH to Trenton). 6

Figure 1.3. (a) Yearly averaged M2 tidal elevation amplitude in Philadelphia from historical records at NOAA stations 8545530 and 8545240 (National Oceanic and Atmospheric Administration), and (b) shipping channel depth over time (U.S. Army Corps of Engineers). 7

Figure 2.1 Delaware Bay. (a) location on the east coast of the United States, (b) topography with color-coded depth (meters) and along-thalweg distance from the mouth of the bay to the head of the tides, (c) mooring locations C1, C2, C4, NOAA waverider buoy R, and wind station W at Ship John Shoal (NOAA #853712). The 10 m isobath is shown in (c). 17

Figure 2.2. Wind statistics in Delaware Bay based on observations at Ship John Shoal (NOAA #853712, station W in fig. 2.1) from January 2006 to November 2015. (a) wind rose with magnitude at 10 m above the surface ($U10$) and direction distribution, (b) probability density function, and (c) cumulative probability. Wind rose highlights the

predominance of down-estuary and up-estuary wind direction during the observation period. 19

Figure 2.3 Observations of wind, waves, and currents in Delaware Bay during a fall storm from 28-Oct-2014 to 7-Nov-2014. (a) wind speed from Ship John Shoal station W, (b) wind and mean wave direction, (c) significant wave height, (d) peak wave period, and (e) depth-averaged along-channel current velocity in the navigational channel (positive velocity denotes flood). Station locations are the same as in figure 2.1 21

Figure 2.4 Idealized model basin with linearly sloping bottom. Depth units are in meters (colors and contours) 25

Figure 2.5 Idealized model results. (a) wave height and period for the coupled case, (b) surface currents including the Stokes drift, (c) leading-order steady momentum balance terms: bottom stress, surface stress, pressure gradient force, and breaking force (BSTR, SSTR, PGF, and BRK, respectively), (d) wave dissipation terms in the coupled run, (e) along-basin transport at each grid point, and (f) effect of whitecapping on transport when included in the breaking force scheme. All results are shown as a function of cross-channel distance in the middle of the basin. Positive values for the momentum and transport terms denote downwind direction. 26

Figure 2.6 Modeled spatial patterns of tidally averaged (a) significant wave height, (b) peak period, and (c) ratio of water depth to wavelength from the coupled model and up-estuary winds. The black contour in (c) denotes the basin-wide median value of h/Lw, and the colorbar highlights values for deep water waves 33

Figure 2.7 Air-sea wave coupling in Delaware Bay. (a) Wind input for the wave action balance, (b) inverse wave age, (c), wave frequency, surface drag coefficient according to

(d) the COARE 3.0 algorithm and (e) the inverse wave age and height (Drennan) parameterization. The ratio between drag coefficients is shown in (f).....35

Figure 2.8 (Left) Surface drag coefficient for down-estuary winds based on the Drennan parameterization. (Right) increment factor with respect to the COARE 3.0 formulation. 39

Figure 2.9 Root-mean-squared (a) current bed stress τc and (b) wave-induced bed stress τw under up-estuary winds.....40

Figure 2.10 Tidally-averaged surface Stokes velocity (arrows) with magnitude in colors (m/s) for the coupled, up-estuary wind run. 42

Figure 2.11 Leading order momentum balance terms in the bay. (Top row) tidally and depth averaged surface stress, pressure gradient force, and bottom stress terms (SSTR, PGF, and BSTR) in the scenario of up-estuary winds with no waves. (Bottom row) increment factor for each term when waves are included in the model. The magnitude of each term is color coded (m/s^2). 43

Figure 2.12 Wave induced momentum budget terms in the bay: horizontal vortex forces, breaking force, and Stokes-Coriolis force (HJVF, BRK, StkCOR). The magnitude of each term is color coded (m/s^2). Note these terms are $O(10^{-5})$. 45

Figure 2.13 Modeled residual circulation (arrows) for the up-estuary (a, b) and down-estuary wind and wind-wave scenarios (c, d). Residual transport magnitude is shown in colors.....48

Figure 2.14 Depth-integrated residual exchange at two cross-bay transects for the modeled up-estuary (a, b) and down-estuary (c, d) wind scenarios. Transect locations are shown on the map. Transport values are plotted for the coupled scenario (wind, wave and tide) and for the uncoupled one (wind and tide). The residual transport in the absence of wind and waves (labeled as tide-only) is shown in all panels for reference.....50

Figure 3.1 Comparison of modeled and observed tidal elevation at six locations in the Delaware estuary (meters). Station locations are shown on the map. The solid black line on the panels has slope equal to 1.....61

Figure 3.2 (a) Modeled M2 elevation amplitude along the channel. Amplitudes in 1901 and 2014 are plotted for reference based on harmonic analysis of NOAA data (stations 8545530 and 8545240), (b) ratio between modern and historical amplitude (a_{2014}/a_{1848}), and (c) travel time of high water in hours. The location of Lewes, Bombay Hook (BH), Wilmington, Philadelphia, and Trenton (head of the tides) are also shown. 65

Figure 3.3 Effect of river discharge (Qr) at the head of the tides near Trenton on (a) M2 tidal elevation amplitude and (b) mean elevation. 67

Figure 3.4 (a) Modeled along-channel tidal current amplitude in the thalweg (solid lines) and shoals (triangles) for both modeled scenarios. (b) Tidal current amplitude ratio between modeled scenarios (thalweg). 70

Figure 3.5 Modeled along-channel tidal current phase in the thalweg (solid lines) and on shoals (triangles) (b) Difference in current phase between modeled scenarios (thalweg). 70

Figure 3.6 (a) Along-estuary phase lag between velocity and elevation in the thalweg (solid lines) and over shoals (triangles) for both modeled scenarios. (b) Departure in the elevation-velocity phase lag after channel deepening (thalweg). 75

Figure 3.7 (a) Cross-section integrated tidal energy flux as a function of distance from the mouth. (b) Close-up of fluxes between kilometers 140 and 160 through Philadelphia. (c) rate of change of energy flux along the estuary, and (d) rate of change of flux in the same segment show in (b). 76

Figure 3.8 Spatial structure of the tidal energy flux in (a) 1848 and (b) 2014. Energy fluxes into and out of the river segments are also shown. The 10m isobath is drawn in both figures to highlight the role of channel deepening on energy flux transmission. Note significantly shallower conditions and reduced flux transmission in 1848. 77

Figure 4.1 Mean along-channel salinity and SSC (colors, psu and mg/L) in 1848 and 2014 under median river discharge at Trenton (350 m3/s).....89

Figure 4.2 (Top) spatial structure of the mean stress magnitude τb and near-bed SSC Cbed for each modeled scenario. Blue lines denote transects near Bombay Hook and Wilmington, and black circles highlight the location of turbidity maxima (Cbed>150 mg/l). (Bottom) root-mean-squared bed stresses in the thalweg from the mouth to the head of the tides. 90

Figure 4.3 Modeled cross-estuary SSC (colors, mg/l) and salinity (contours, psu) at Bombay Hook in 1848 during (a) late flood, (b) mid ebb and (c) late ebb. Tidal stage (m) is shown in all panels.....92

Figure 4.4 Same legend as figure 4.3 but in the 2014 scenario. 93

Figure 4.5 Change in bed thickness after a 1-month run in (a) 1848 and (b) 2014. Blue and red denote erosion and deposition, respectively (mm). Two green arrows are drawn to highlight enhanced deposition in the 2014 scenario, but are also plotted in (a) for reference. (c) Cross-section integrated net sediment deposition along the estuary in ton/km (i.e. deposition – erosion). Peaks in sediment trapping (green arrows) are the same shown on (a) and (b).....94

Figure 4.6 Observed shoreline retreat and modeled changes to sediment supply near Marshall Island wetland. (a) Coordinates of a tidal gauge in Leipsic creek (Delaware coastline) in 1882, (b) same coordinates in 2019 from Google Earth, (c-d) modeled bed

change in 1848 and 2014, and (e-f) modeled mud fraction in 1848 and 2014. The purple marker denotes the location of the tidal gauge in 1882. Snapshot in (a) was retrieved from the U.S. National Archives and Records Administration. 96

Figure 4.7 Mean along-channel velocity in (a) 1848 and (b) 2014 in the estuary. (c) subtidal shear (ΔU) in each modeled scenario (see text for definition).....97

Figure 4.8 (Top) Mean sediment concentration, (middle) residual velocity, and (bottom) mean advection of sediment in Bombay Hook in (left) 1848 and (right) 2014 Positive values of velocity and flux denote the landward direction. 99

Figure 4.9 Same legend as figure 4.8 but in Wilmington. 99

Figure 4.10 Tidal pumping fluxes in (left) Bombay Hook and (right) Wilmington for the (top) 1848 and (bottom) 2014 scenarios. 100

LIST OF TABLES

Table 3.1 Effect of channel deepening and river discharge on tidal asymmetries in the tidal river near Trenton.....68

Chapter 1 – Introduction

1.1 Estuaries in the Anthropocene

The industrial revolution marked the onset of the Anthropocene, an era in which humans can measurably impact large scale earth processes (Waters et al., 2016). Anthropogenic signatures can be detected in recent ocean acidification trends, shifts in marine food web interactions, and changes in underwater morphology (Wallace et al., 2014; Levin & Möllmann, 2015; van Maren et al., 2015). In the coastal ocean, urbanized estuaries undergo accentuated anthropogenic stresses due to nutrient pollution, channel deepening, stream bank disturbances, and dam construction (Senior & Green, 2002; Wang et al., 2015). To varying degrees, such human-induced alterations to estuarine basins can significantly impact the stratification dynamics, salt intrusion, sediment trapping, and flushing rates of waterborne material of public health interest such as sewage, heavy metals, and microorganisms.

Estuaries are often close to areas of constant human activity, and the trajectory of these systems in response to anthropogenic forcing is strongly influenced by hydrodynamic processes that drive transport and exchange. The comprehensive study of estuarine hydrodynamics, which dates back to the seminal works by Pritchard (1956) and Hansen and Rattray (1965, 1966), describes the water exchange mechanisms based on variables such as the river discharge, stratification, depth, width, and eddy viscosity. As a whole, these variables span the 'parameter space' in estuarine physics. Regime diagrams based on parameters that describe estuarine flows have provided valuable insight in their

classification over the last decades (MacCready & Geyer, 2010). However, since humans may now appreciably change the geometry of an estuary in time scales much faster than the geological, it is essential to better understand the influence of these changes on, for example, circulation, stratification and the transport and fate of suspended material.

The most conspicuous example of a direct human intervention of an estuarine basin is the creation and maintenance of navigational channels (Oliveira et al., 2006; Liria et al., 2009; Morelli & Gasparon, 2015; Marmin et al., 2016; Wang et al., 2016). In the United States, estuaries such as the Hudson River, Puget Sound, and the bays in San Francisco, Delaware, Tampa, Mobile, and Galveston feature channels that connect ports of commercial importance with oceanic cargo ship routes. The frequency of maintenance dredging in these channels depends largely on the erosion and deposition rates of sediment, which are inextricably linked to the location of topographic features, the estuarine turbidity maximum, tidal asymmetries in mixing, density fronts, and to the sediment trapping efficiency in tidal rivers. Dedicated studies on the human impacts in estuarine dynamics are relatively scarce, with the possible exceptions of the Ems-Dollard and Scheldt systems in the Netherlands (van Maren et al., 2015; Wang et al., 2015).

1.2 The Delaware Estuary

The Delaware Estuary is located on the Atlantic coast of the United States and consists of three segments as shown in figure 1: (1) a 'lower' polyhaline estuary from the mouth (Lewes) to Bombay Hook, (2) a convergent, 'upper' mesohaline estuary from Bombay Hook to Wilmington; and (3) and a tidal freshwater river that extends from the mean location of

the salt front (2 psu isohaline, km ~100) to the head of the tides near Trenton. The bottom morphology consists of subtidal flats, linear sand ridges, and a deep (>10 m) shipping channel that extends the full length of the estuary. The estuary as a whole is classified as strongly convergent and moderately dissipative in terms of tidal energy (Lanzoni & Seminara, 1998). The tidal regime is predominately semidiurnal where the M2 and S2 tidal constituents account for up to 96% of the tidal variability (Aristizabal & Chant, 2013). The main freshwater sources are the Delaware (330 m^3/s mean annual discharge), Schuylkill (77 m^3/s) and Christina (19 m^3/s) rivers (figure 3.1a).

Bathymetric grids for historical and modern estuary scenarios were constructed for this study. The historical bathymetry was based on soundings plotted in an electronic version of an engraved nautical chart entitled “Map of Delaware Bay and River”, published in 1848 by the predecessor agency of the Office of Coast Survey. This is the first nautical chart available for the entire Delaware Estuary, and was constructed from lead-line soundings collected between 1840 and 1844 by the U.S. Navy. A total of 9828 of the charted soundings, referenced to mean lower low water, were digitized in a geographic information system (GIS), and then interpolated and georeferenced to create a bathymetric grid. The shoreline drawn on the chart was digitized and used as the spatial limit of the grid.

For the modern estuary it was necessary to construct a composite bathymetric grid from available hydrographic survey data. For the area of the recently deepened shipping channel, soundings collected by the U.S. Corps of Engineers between 2012 and 2014 were used. These soundings were obtained shortly after the channel was dredged to a uniform depth of 45 ft (13.7 m). For all other areas of the estuary, digitally archived soundings

from the Office of Coast Survey were used for the grid. Most of these soundings were obtained by surveys conducted after 2001. In total, 772,449 soundings were interpolated and gridded in a GIS using a 2001 National Oceanic and Atmospheric Administration (NOAA) digital shoreline for the grid boundary. To account for sea-level rise between the historical and modern periods, both sets of soundings were normalized to the Mean Tide Level (MTL) datum for the 1983-2001 epoch using tidal datums reported with the original surveys. In other words, differences in 1848-2014 bathymetry discussed in this thesis reflect natural (sediment accumulation, erosion) and human impacts (dredging) on estuarine morphology over time.

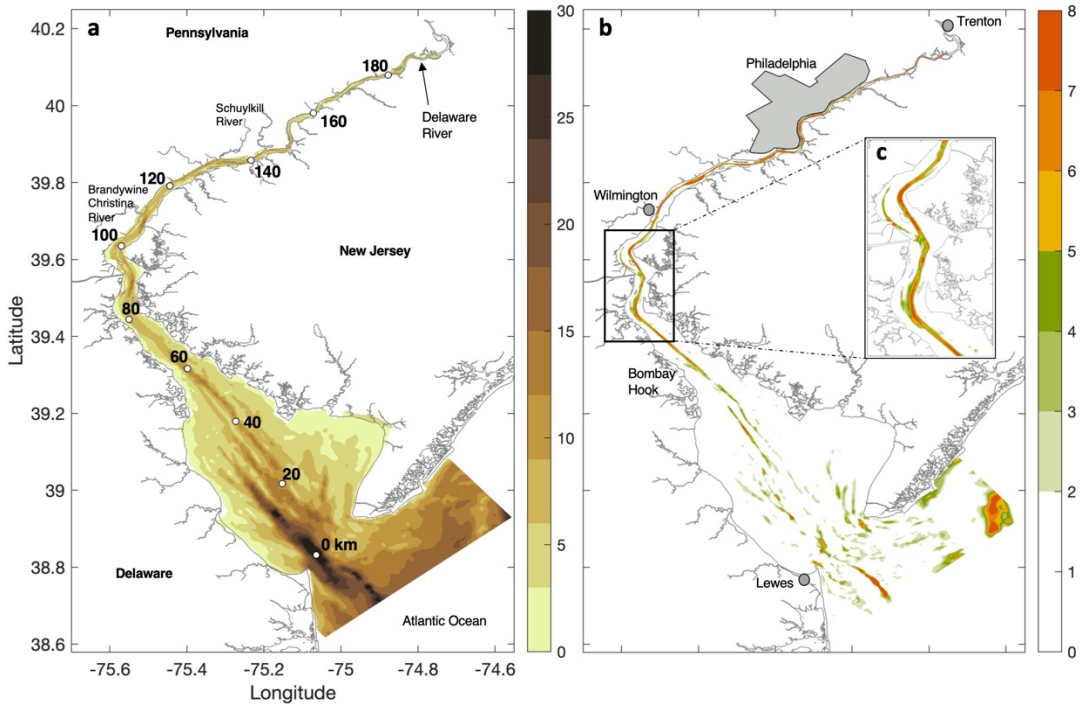

Figure 1.1. (a) Delaware Bay bathymetry in meters for the historical scenario (1848) and along-thalweg coordinates from the mouth to the head of tides near Trenton. (b) Highlight of deepened areas with respect to the digitized bathymetry from 2014. The location of cities, rivers, and states are also shown.

Comparison of historical (1848) and modern (2014) bathymetry reveals that channel deepening by dredging increased the thalweg of the estuary from roughly 8 m to 15 m over time, in contrast to relatively unchanged depths elsewhere in the subtidal estuary (Figure 1.2). The width is maximum in the bay (45 km cross-estuary) and drops to 10 km at Bombay Hook, to 2 km at Wilmington, and to 0.3 km at Trenton. The width of the dredged channel in the modern estuary is approximately 150 m, therefore the impact of channel deepening on hydraulics should become increasingly important up-estuary as the width of the channel becomes a significant fraction of the total width. Near Philadelphia, the width of the shipping channel is about 25% of the total width while in the widest region of the lower bay the fraction is only 0.04%. Channel deepening has had a negligible effect on the hypsometry of the lower bay (Lewes to Bombay Hook), but the change is conspicuous in the upper estuary and tidal river segments from Bombay Hook to Trenton (Figure 1.2b). About 20% of the subtidal area in these segments was below 10 m in 2014 compared to only 2% in 1848. This change is due to dredging within the shipping channel, combined with erosional bottom scour immediately adjacent to the channel.

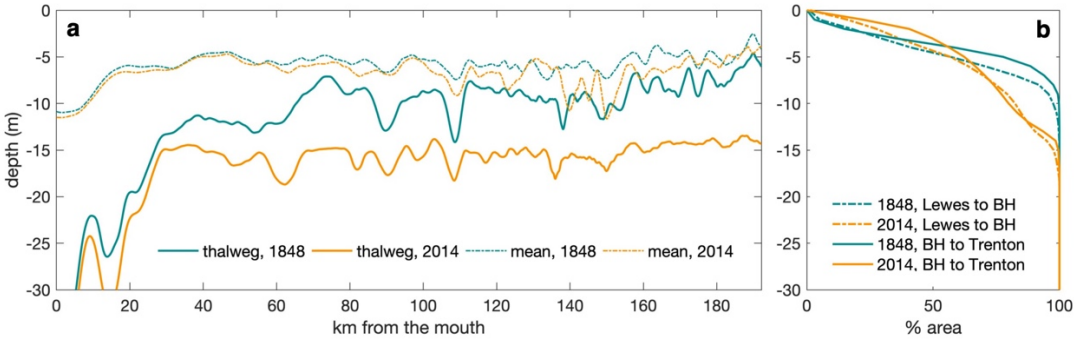

Figure 1.2. (a) Thalweg and mean depth in the historical and modern Delaware Estuary, starting at the mouth near Lewes (km 0) to the head of the tides near Trenton (km 190). (b) Changes in basin hypsometry for the lower bay (Lewes to Bombay Hook, 'BH') and in the upper estuary and tidal river (BH to Trenton).

Before 1890, the maximum depth near Philadelphia was about 20 ft (6 m). The increasing need for a deeper shipping channel became evident in the early 1900s when Hog Island, currently Philadelphia's international airport, featured one of the largest shipyards in the world (Blood, 1918). According to the U.S. Corps of Engineers, channel deepening and maintenance dredging along the full length of the estuary started in the early 20th Century and continued over the ensuing decades to accommodate vessels bound for the ports of Wilmington and Philadelphia. Authorized depths of the shipping channel increased from 26 ft (7.9 m) in 1898 to 45 ft (13.7 m) in 2014 (figure 3.3b) in-step with vessels of increasing size. A period of dredging between 1920 and 1960, when channel depth increased by about 30% in Philadelphia (figure 1.3b), coincides with a 1.2-fold increase in M2 elevation amplitude based on harmonic analysis of tide observations (figure 1.3a). A modeling study by DiLorenzo et al. (1993) indicates that tidal amplification in the Delaware between the late 1900s and the late 1980s, including the observed shifts in Philadelphia, were likely due to the reduced hydraulic drag caused by channel deepening. Although that study offers some insight into the role of deepening on amplification, the

focus was site-specific due to an interest in the engineering of the shipping channel. As in DiLorenzo et al. (1993), we study the impact of dredging on elevation and phase in the estuary, but explore additional barotropic wave dynamics such as tidal energy fluxes and quantify historical shifts that altered the competition between friction and convergence.

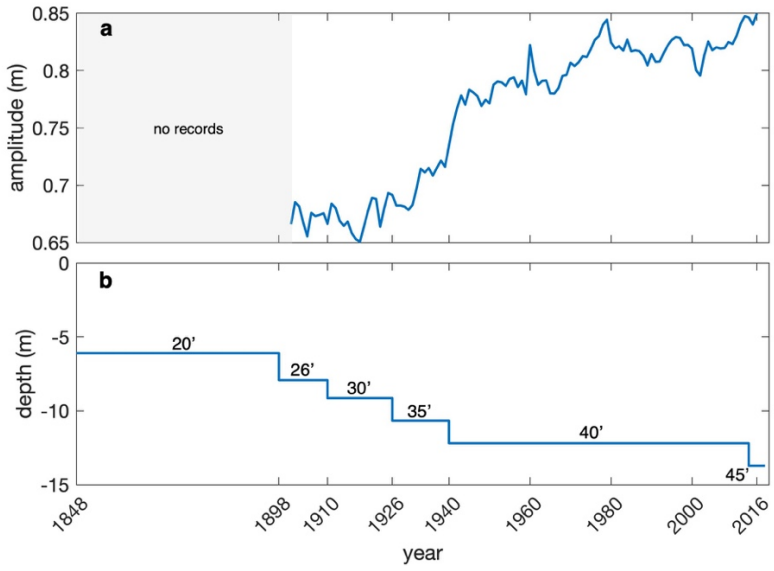

Figure 1.3. (a) Yearly averaged M2 tidal elevation amplitude in Philadelphia from historical records at NOAA stations 8545530 and 8545240 (National Oceanic and Atmospheric Administration), and (b) shipping channel depth over time (U.S. Army Corps of Engineers).

1.3 Thesis Goals

This work is part of the project titled 'Toward Sustainable Urban Estuaries in the Anthropocene' funded by the National Science Foundation (NSF grant 1325258) under the Coastal Science, Engineering and Education for Sustainability (Coastal SEES) program. The overarching goal of this study is to explore the role of human induced changes in morphology in the hydrodynamics of a coastal plain estuary, and the consequences of such changes in hydrodynamics and sediment transport. This work is based mainly on numerical

modeling with realistic bathymetry and idealized forcing in the Delaware Estuary and the principal objectives are:

i. To explore the role of topography on the wave climate of the bay as well as the impact of wind waves on the momentum budget and subtidal exchange during coastal storms.
ii. To study the impact of channel deepening on barotropic tidal dynamics in an urbanized, convergent estuary.
iii. To evaluate the response of sediment transport patterns to historical dredging in an urbanized estuary.

Each scientific objective motivates a dissertation chapter as follows:

- Chapter 2: Effects of Locally Generated Wind Waves on the Momentum Budget and Subtidal Exchange in Delaware Bay.
- Chapter 3: Impact of Historical Channel Deepening on Tidal Hydraulics in the Delaware Estuary.
- Chapter 4: Changes to Suspended Sediment Concentration and Trapping in the Delaware Estuary Associated with Dredging.

Chapter 2 - Effects of Locally Generated Wind Waves on the Momentum Budget and Subtidal Exchange in Delaware Bay

2.1 Abstract

A numerical model with a vortex force formalism is used to study the role of wind waves in the momentum budget and subtidal exchange of Delaware Bay. Wave height and age in the bay have a spatial distribution that is controlled by bathymetry and fetch, with implications for the surface drag coefficient in young, underdeveloped seas. Inclusion of waves in the model leads to increases in the surface drag coefficient by up to 30% with respect to parameterizations in which surface drag is only a function of wind speed, in agreement with recent observations of air-sea fluxes in estuaries. The model was modified to prevent whitecapping wave dissipation from generating breaking forces since that contribution is integrally equivalent to the wind stress. The proposed adjustment is consistent with previous studies of wave-induced nearshore currents, and with additional parameterizations for breaking forces in the model. The mean momentum balance during a simulated wind event was mainly between the pressure gradient force and surface stress, with negligible contributions by vortex, wave breaking (i.e. depth-induced), and Stokes-Coriolis forces. Modeled scenarios with realistic Delaware bathymetry suggest that the subtidal bay-ocean exchange at storm time scales is sensitive to wave-induced surface drag coefficient, wind direction, and mass transport due to the Stokes drift. Results herein are applicable to shallow coastal systems where the typical wave field is young (i.e. wind seas) and modulated by bathymetry.

2.2 Introduction

The dynamics of shallow bays are mainly governed by the interaction of density gradients and tides, but episodic wind events can also have an important role in flushing and circulation (Geyer, 1997; Scully et al., 2005; Whitney & Codiga, 2011). Studies of wind-driven circulation in systems such as lakes provide insight into how estuaries can respond to wind events. In a large lake, Csanady (1973) found that axial winds led to a laterally sheared flow with a downwind current in shallow water and return flow over deeper regions. In the case of rotating basins with more complicated (e.g. multi-channel) bathymetry, the Coriolis effect can introduce transverse circulation in the form of gyres and lead to asymmetries in the upwind and downwind currents (Sanay & Valle-Levinson, 2005). Rotation-induced flow asymmetries in estuaries can develop in response to Ekman straining through the lateral advection of the along-channel momentum (Scully et al., 2009). Winds can also induce dynamic responses in estuaries through non-local effects. For example, along-shore winds on the shelf can drive Ekman transport into or out of bays, leading to adjustments in the subtidal sea level as observed in Delaware Bay (Wong & Garvine, 1984). A simple barotropic model of shelf-estuary coupling reveals that such a response to remote winds is significant when estuaries are short relative to subtidal elevation wavelengths, which can be up to 10 times the typical basin length (Garvine, 1985; Henrie & Valle-Levinson, 2014).

Although the aforementioned contributions to the literature denote an initial success in understanding the effects of local and remote wind stresses on circulation in shallow bays, an aspect that is often overlooked is the impact of local, wind-generated waves on

circulation and boundary layer drag. For example, Signell et al. (1990) reported that wind-driven flushing in a long embayment is modulated by near-bed wave-current interactions, but the wave field considered in that study was prescribed and uniform instead of wind-generated. Similarly, Bricker et al. (2004) used a model with wave-current interactions in the bottom layer to study the impact of waves and circulation in San Francisco Bay, but considered no feedback between waves and surface drag. In terms of hurricanes in coastal plain estuaries, Li et al. (2006) reported the impact of storm surges on the layered circulation in Chesapeake Bay and omitted wind-wave forcing in the model. The mechanisms of wave generation and dissipation are now relatively well understood and have informed the creation of coupled wave and circulation models (Warner et al., 2008), whose output can be used to fully assess the impact of wind generated waves on shallow water circulation. In the following sections we describe how waves may play a role in the transfer of energy, mass, and momentum across the air-sea and bed interfaces, as well as through the water column with a focus on implications for the momentum budget and subtidal exchange in coastal plain estuaries.

2.2.1 Surface Layer

At the surface layer, wind waves influence the mechanical coupling between the ocean and the atmosphere by altering the surface drag coefficient for the wind stress, the energy transfer from winds to the wave field, and the injection of turbulence. The drag coefficient (C_D) that is used to calculate wind stress (τ_s) is often expressed as a function of wind speed at a reference height of 10 meters (U_{10}). The established bulk formula for the wind stress magnitude in a neutrally stable atmosphere takes the form $\tau_s = \rho_a C_D U_{10}^2$ where ρ_a is the air density. Examples of widely used parameterizations for C_D include the works of Wu

(1982) and Large and Pond (1981) in which the drag coefficient is proportional to the wind speed. Following those and other studies, significant advances in understanding air-sea momentum fluxes resulted from the Tropical Ocean Global Atmosphere, Coupled Ocean Atmosphere Response Experiment (TOGA-COARE) program (Fairall et al., 1996). The extensive datasets from those experiments improved the parameterizations for C_D and retained the general trend wherein drag increases with U_{10}; see, for example, the COARE 3.0 and 3.5 algorithms (Fairall et al., 2003; Edson et al., 2013).

Parallel to the developments of TOGA-COARE, other authors reported that calculating C_D based on wind speed alone may be inadequate since drag is also communicated by the spatially variable sea surface roughness, which depends on factors such as fetch, wave phase speed, and wind duration (Drennan et al., 2005). Accounting for these details can be achieved by expressing the drag coefficient as a function of the surface roughness length (z_0) as $C_D = (\kappa/\ln(z_{ref}/z_0))^2$, where κ is the von-Karman constant and z_{ref} is a reference height above the surface. For the previous C_D expression, $z_0 = z_s + z_r$, where z_s and z_r are the smooth and rough (turbulent) components of surface roughness. The rough contribution can be expressed as (Charnock, 1955):

$$z_r = \alpha \frac{u_*^2}{g} \tag{2.1}$$

where α is referred to as Charnock's alpha, $u_* = \sqrt{\tau_s/\rho_a}$ is the surface shear velocity, and g is the gravitational acceleration. Kitaigorodskii (1973) and later other authors (Johnson & Vested, 1992; Oost et al., 2002) proposed that the effect of both winds and waves on

roughness can be accounted for by making α depend on the wave age, or the ratio between the wave phase speed and the surface shear velocity, c_p/u_*. One of the advantages of considering the wave age to model Charnock's alpha is that it incorporates the roughness' sensitivity to depth, fetch, and duration, which may not be appropriately captured by the bulk wind speed (Fisher et al., 2015). As will be shown later, the wave age in shallow, fetch limited environments is typical of underdeveloped young seas ($c_p/u_* < 33$, (Donelan, 1990)) for which some authors have proposed special roughness parameterizations. For instance, Drennan et al. (2003) reported that the turbulent roughness length is a function of the inverse age and significant wave height H_s in young seas according to

$$z_r = 3.35 H_s \left(\frac{u_*}{c_p}\right)^{3.4} \tag{2.2}$$

which indicates that the roughness evolves with the wave field instead of taking a static value based on U_{10}. In a typical estuary or shallow embayment with shoals and a relatively deep channel, one might expect a heterogeneous spatial distribution of z_r given its dependence on c_p and H_s, which are sensitive to topography (Holthuijsen, 2010). Moreover, salient bathymetric features such as sills and ridges may cause highly localized reductions in phase speed and wave height, which would add to the inherent complexity of the wave age field.

The concept of wave age has also been suitable in modeling the air-sea energy transfer that leads to wind wave generation and growth. The wind input, or S_{in} in the parlance of Komen et al. (1984), is the source term in the wave action balance that represents the

energy transfer from the wind to the wave field. Measurements and theoretical analyses (Cavaleri & Malanotte-Rizzoli, 1981; Snyder et al., 1981; Komen et al., 1984) show that $S_{in} = A + B \cdot E$ where A and B are linear and exponential growth coefficients and E is the wave energy spectrum as a function of frequency and direction. The exponential growth term B quickly dominates over the linear and is a function of the inverse age and frequency σ (Komen et al., 1984; Holthuijsen, 2010):

$$B = \max\left[0, 0.25\frac{\rho_a}{\rho}\left(28\frac{u_*}{c_p}\cos(\theta - \theta_w) - 1\right)\right]\sigma \tag{2.3}$$

ρ is the water density, and θ, θ_w are the wave and wind direction, respectively. According to (2.3), the net energy input to the wave field is proportional to wave frequency, inverse age, and also wave height since $E \sim H_s^2$. The dependencies of the wind input to these variables also suggest that wave growth in bays and estuaries may be sensitive to topography and wind-wave misalignment caused by refraction.

In addition to modulating surface drag and wave growth, wave breaking releases energy that enhances turbulence in the surface layer (Craig & Banner, 1994). This process is particularly important in estuaries where wall-layer theory predictions can underestimate observed dissipation rates of turbulent kinetic energy under wind waves. For example, Jones and Monismith (2008) observed that about 90% of the turbulent kinetic energy injected to the water column was provided by wave whitecapping in San Francisco Bay. An important effect of turbulence injection is a reduction in vertical shear and surface velocities (Carniel et al., 2009).

2.2.2 Bottom Layer

In the bottom boundary layer, the effective drag is modulated by waves, currents, or both. If wave and current velocities are not negligible near the bed, the effective bed roughness can be larger than that determined by physical elements such as sediment and ripples (Grant & Madsen, 1982; Styles & Glenn, 2002; Scully et al., 2018). In collinear wave-current flow, the maximum bed stress $\tau_{\mathrm{b,max}}$ is the sum of the current stress (τ_{c}) and the maximum wave-induced stress (τ_w). In this case, the vertical eddy viscosity scales with $\sqrt{\tau_{\mathrm{b,max}}/\rho}$ in the wave-current boundary layer, and with $\sqrt{\tau_c/\rho}$ in the current boundary layer (Styles & Glenn, 2000). The main effect of waves in the bottom layer is then an increase in turbulence production and bed drag and a reduction in the near-bed velocity and transport. This was the case for example in San Francisco Bay where the inclusion of a wave-current interaction scheme led to a 10% reduction in the shallow water, root-mean-squared current speeds (Bricker et al., 2004). A similar case was modeled in Massachusetts Bay where wave-induced bed drag reduced alongshore transport by 10%-50% (Signell & List, 1997).

2.2.3 Wave-induced forces in the water column

In terms of forces outside boundary layers, initial formulations for the wave-induced momentum flux refer to a formalism based on the radiation stress gradient (Mellor, 2010). This approach is grounded on a seminal paper by Longuet-Higgins and Stewart (1964) in which the phase averaged vertical integrals of hydrostatic and wave-induced pressures are considered in the momentum budget (Kumar et al., 2011). Spatial differences in horizontal momentum fluxes (e.g. due to wave breaking) lead to local changes in elevation known as wave setups and set downs (Dean & Dalrymple, 2001). An alternative method to compute

the effect of waves on 3D currents is the vortex force formalism, which can be derived by using a Helmholtz decomposition of the advective acceleration in the Navier-Stokes equations (Uchiyama et al., 2010). A convenient feature of the vortex approach is that it cleanly separates conservative wave forces (the gradient of the Bernoulli head, the vortex force, and the Stokes-Coriolis force) from non-conservative wave forces (the acceleration induced by wave breaking). Vortex forces arise from the interaction between the current shear and the Stokes drift (Craik & Leibovich, 1976; Nepf & Monismith, 1991), while Stokes-Coriolis forces result from the effects of the earth's rotation on the Stokes velocity. The non-conservative force corresponds to the highly turbulent momentum transfer that occurs during wave breaking. The vortex force formalism has been successfully applied in numerical models of coastal wave-current interaction. For example, the breaking-induced acceleration was a leading order momentum balance term in the inlet of Willapa Bay (Olabarrieta et al., 2014), while both breaking and vortex forces were important in a sandy beach in North Carolina (Uchiyama et al., 2010). The same approach was employed in a circulation model of a coral reef where the breaking acceleration was the same order of magnitude as the pressure gradient force and the vertical stress divergence (Rogers et al., 2017).

2.2.4 Study goals and approach

The main goal of this study is to evaluate how the inclusion of wind generated waves impacts the momentum budget and subtidal exchange of a realistic coastal plain estuary with complex topography, Delaware Bay (figure 2.1). We use a numerical model to characterize (i) the role of wave dissipation mechanisms on wave induced forces, (ii) the impact of wind waves on surface and bed stresses over shallow, complex topography, and

(iii) the contribution of wave-induced forces to the momentum budget and subtidal exchange in the bay. One of the salient bathymetric features of the study region is its shipping channel, which has been dredged for over a century to ensure navigability into the Wilmington-Philadelphia port complex (DiLorenzo et al., 1993). Results herein allow comparison of wave dynamics with other coastal systems where wave-current interactions have been studied more thoroughly such as tidal inlets, inner continental shelves, beaches, and coral reefs.

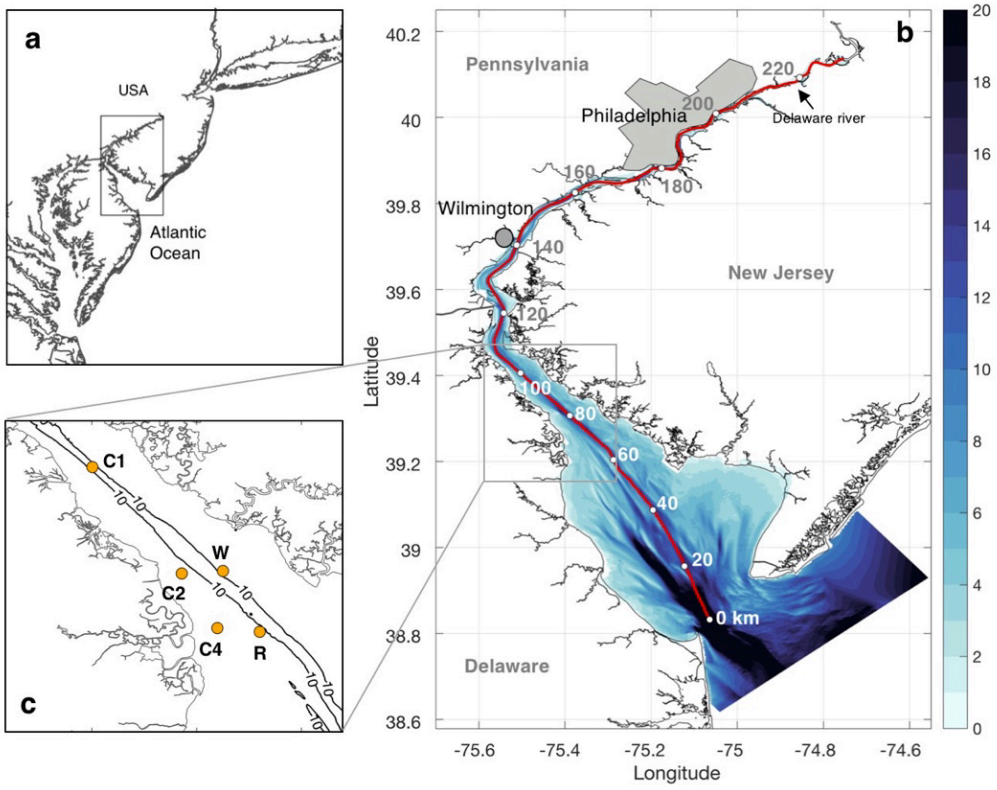

Figure 2.1 Delaware Bay. (a) location on the east coast of the United States, (b) topography with color-coded depth (meters) and along-thalweg distance from the mouth of the bay to the head of the tides, (c) mooring locations C1, C2, C4, NOAA waverider buoy R, and wind station W at Ship John Shoal (NOAA #853712). The 10 m isobath is shown in (c).

This chapter is organized as follows: section 2.3 describes the main features of the wind-wave climate in the bay. Section 2.4 outlines the governing equations of a numerical model that computes the effect of waves on currents. Section 2.5 presents the model results and a discussion. Model results include a series of idealized simulations in a long channel with sloping bathymetry to assess the effect of waves on currents, as well as simulations with the realistic Delaware bathymetry and idealized forcing. Section 2.6 contains a summary and conclusions.

2.3 Observations of Winds and Waves

Wind data from Ship John Shoal (NOAA station # 853712, marked as W in figure 2.1) between January 2006 and November 2015 indicate that the average wind speed is in the order of 6 m/s, and that the dominant wind directions are aligned with the main axis of the bay (figure 2.2a). The strongest winds usually come from the northwest (down-estuary) and may exceed 12 m/s, although there is an important contribution of southeasterly (up-estuary) winds to the wind rose. A probability density function (figure 2.2b) indicates that the most frequent speeds in the bay are in the 4 m/s to 6 m/s range. Storms and weather events whose speed exceeds 10 m/s were observed 10% of the time (Figure 2.2c). Mean wind speeds are maximum during winter months (~8 m/s) and minimum during summer (~5 m/s) according to a detailed study of wind climate in the bay and adjacent continental shelf (Hughes & Veron, 2015). Remote winds along the continental shelf also increase or decrease subtidal elevation in the bay depending on the direction of the resulting Ekman transport as demonstrated by Wong and Garvine (1984).

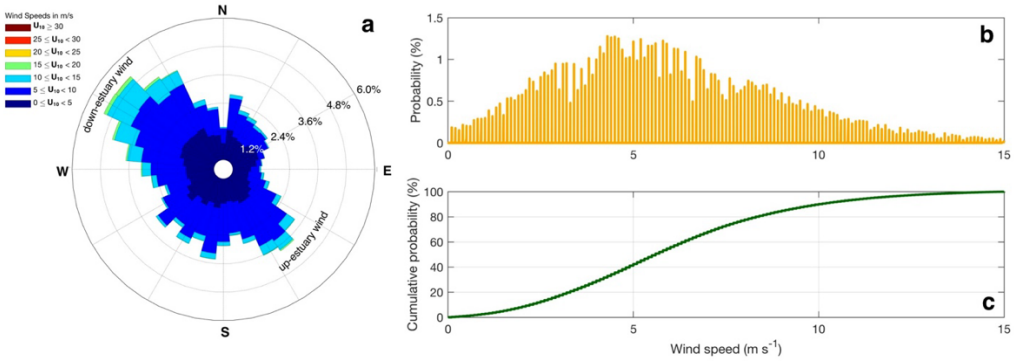

Figure 2.2. Wind statistics in Delaware Bay based on observations at Ship John Shoal (NOAA #853712, station W in fig. 2.1) from January 2006 to November 2015. (a) wind rose with magnitude at 10 m above the surface (U_{10}) and direction distribution, (b) probability density function, and (c) cumulative probability. Wind rose highlights the predominance of down-estuary and up-estuary wind direction during the observation period.

In addition to a focus on wind forcing, a number of authors studied wave dynamics in the bay from multiple perspectives that include the role of waves on mesoscale beach behavior (Jackson, 1995), air-sea interactions under light winds (Savtchenko et al., 1999), water level and velocities in marsh channels (Dzwonkowski et al., 2014), surface wave modeling (Jenkins, 2015), and Hurricane Sandy impacts on salt marshes of New Jersey (Elsey-Quirk, 2016). One of the main consequences of the bay's geometric and bathymetric configuration is a restriction on the up-estuary propagation of Atlantic swell. Kukulka et al. (2017) used a wave ray analysis to demonstrate that bathymetric refraction plays a key role in sheltering the lower bay from swell, and that current induced refraction at the mouth is complicated by the spatial heterogeneity of tidal currents. The study concluded that remotely generated waves cannot deeply propagate into the bay, and therefore that waves are predominantly generated by local wind. The latter is in agreement with findings by Chen et al. (2018) who concluded that local winds constitute the main source of wave

energy in much of the bay. However, these studies did not evaluate the role of waves in the momentum budget, surface stresses, and subtidal exchange.

For insight into the evolution of waves and currents during storm events, we deployed instruments at locations C1 (AWAC 1000kHz), C2, and C4 (RDI ADCP 1200kHz) during fall 2014 (figure 2.1c). Hourly measurements of wind speed and direction were extracted from the Ship John Shoal lighthouse (W), and additional wave data was obtained from a NOAA waverider buoy (location R). A summary of wind, wave, and current observations during a down-estuary wind event from October 28th to November 7th is shown in figure 2.3. Peak storm winds on November 2 reached 15 m/s at Ship John Shoal and generated waves (0.5 m – 1.0 m height, 3 s – 5 s period) in locations C1, C2, C4 and R. The maximum wave height (~1.2 m) was registered at location R and was slightly greater than the measured waves in the other stations, possibly due to a longer fetch. Wave height records between November 1st and November 3rd suggest that tidal currents weakly modulated wave amplitude by up to 25 cm. These observations reveal that the tidal variability of wave height and period in the bay is small relative to their mean value during the storm, which is in agreement with results presented by Kukulka et al. (2017) who also found weak interactions waves and tides in the bay through numerical modeling.

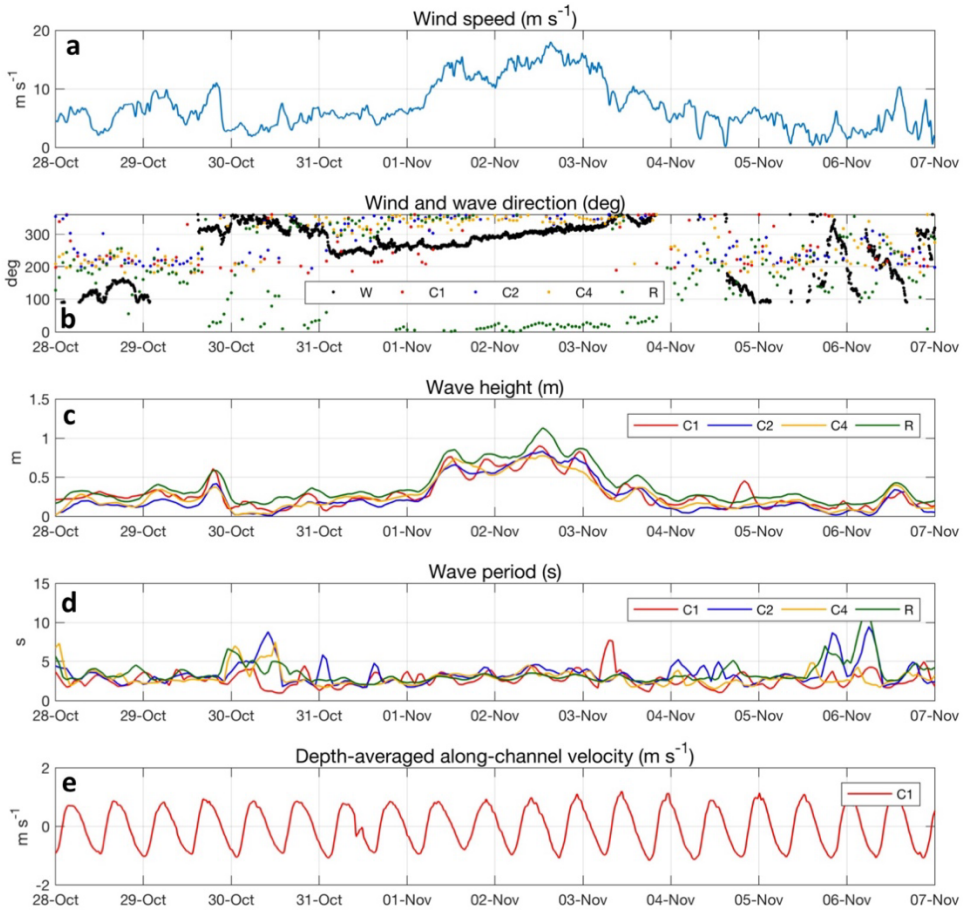

Figure 2.3 Observations of wind, waves, and currents in Delaware Bay during a fall storm from 28-Oct-2014 to 7-Nov-2014. (a) wind speed from Ship John Shoal station W, (b) wind and mean wave direction, (c) significant wave height, (d) peak wave period, and (e) depth-averaged along-channel current velocity in the navigational channel (positive velocity denotes flood). Station locations are the same as in figure 2.1

2.4 Modeling Framework

2.4.1 Coupled Modeling System

In this study we use the Coupled Ocean Atmosphere Wave Sediment Transport Modeling System, COAWST (Warner et al., 2010). COAWST couples a terrain-following hydrodynamic model, the Regional Ocean Modeling System ROMS (Shchepetkin &

McWilliams, 2005) with a spectral wave model, Simulating Waves Nearshore SWAN (Booij et al., 1999). SWAN (v41.20) calculates the wave action density (Holthuijsen, 2007):

$$\frac{\partial N}{\partial t} + \frac{\partial \left(\vec{u} + \overrightarrow{c_g}\right) N}{\partial x^{\alpha}} + \frac{\partial (c_{\theta} N)}{\partial \theta} + \frac{\partial (c_{\sigma} N)}{\partial \sigma} = S \tag{2.4}$$

where N is the wave action or energy per unit frequency, $\vec{u}$ is the surface current vector, $\overrightarrow{c_g}$ is the wave group velocity, x^{α} denotes 2D spatial coordinates, c_{θ} is the refraction velocity, and c_{σ} is the frequency shift velocity. The source term S includes wind generation S_{in}, dissipation due to whitecapping (i.e. deep water breaking) S_{wc}, bottom friction S_{bf}, depth-limited breaking S_{br}, and two nonlinear redistribution processes (triad S_{nl3} and quadruplet S_{nl4} wave-wave interactions). A full expression of the source term is then

$$S = S_{in} + S_{wc} + S_{bf} + S_{br} + S_{nl3} + S_{nl4} \tag{2.5}$$

The energy transfer from the wind to the wave field is calculated following Cavaleri and Malanotte-Rizzoli (1981) and Komen et al. (1984). Energy dissipation by whitecapping, bottom friction, and depth-limited breaking are computed with the parameterizations by Komen et al. (1984), Madsen et al. (1988), and Battjes and Janssen (1978), respectively. Within the COAWST framework, ROMS incorporates output data from SWAN and employs a vortex force formalism to compute the wave effects on currents as implemented by Kumar et al. (2012). The Navier-Stokes equation with phase-averaged wave-induced momentum terms can be written in compact form as (boldface denotes vector quantities):

$$\frac{\partial \boldsymbol{u}}{\partial t} + (\boldsymbol{u} \cdot \nabla_{\perp})\boldsymbol{u} + w\frac{\partial \boldsymbol{u}}{\partial z} + f\hat{\boldsymbol{z}} \times \boldsymbol{u} + \nabla_{\perp}\varphi - \boldsymbol{F} - \boldsymbol{D} + \frac{\partial}{\partial z}\left(\overline{\boldsymbol{u}'w'} - \nu\frac{\partial \boldsymbol{u}}{\partial z}\right) = -\nabla_{\perp}K + \boldsymbol{J} + \boldsymbol{F_w} \quad (2.6)$$

where $\boldsymbol{u} = u, v$; w are the horizontal and vertical components of the Eulerian velocity, z is the vertical coordinate, f is the Coriolis factor, φ is the normalized dynamic pressure, $\boldsymbol{F}$ is the non-wave non-conservative force, $\boldsymbol{D}$ is the diffusive term, $\overline{\boldsymbol{u}'w'}$ is the Reynolds stress, ν is the kinematic viscosity, K is the Bernoulli head or the wave kinetic energy density (McWilliams et al., 2004), $\boldsymbol{J}$ is the vortex force, and $\boldsymbol{F_w}$ is the non-conservative wave force. The gradient term $\nabla_{\perp}\varphi$ contains the non-wave barotropic and baroclinic pressure gradients, and the gradient of the quasi-static sea level (ζ). The latter includes an inverse barometric response term and a wave-averaged setup:

$$\zeta = -\frac{P_{\text{atm}}}{\rho g} - \frac{H_{rms}^2 k}{8\sinh(2\mathcal{H})} \quad (2.7)$$

P_{atm} is the atmospheric pressure, H_{rms} is the root-mean-squared wave height, g is the gravitational acceleration, and $\mathcal{H}$ is the normalized vertical length. The expression for the vortex force $\boldsymbol{J}$ is:

$$J = -\hat{\boldsymbol{z}} \times \boldsymbol{u^{st}}[(\hat{z} \cdot \nabla_{\perp} \times \boldsymbol{u}) + f] - w^{st}\frac{\partial \boldsymbol{u}}{\partial z} \quad (2.8)$$

where $\boldsymbol{u^{st}} = u^{st}, v^{st}; w^{st}$ are the components of the Stokes drift. The default algorithm for $\boldsymbol{F_w}$ incorporates whitecapping and depth-limited breaking dissipation from SWAN and converts them into forces in ROMS according to:

$$\boldsymbol{F_w} = \frac{(S_{wc} + S_{br})}{\rho\sigma} f^b(z)\boldsymbol{k} \tag{2.9}$$

in which $f^b(z)$ is a surface-enhanced vertical distribution function, and $\boldsymbol{k}$ is the wavenumber vector. Regarding the conservation of mass, the total water transport depends on the Lagrangian velocity field $\boldsymbol{u^l}$ given by the sum of the Eulerian and wave-induced Stokes velocities:

$$\boldsymbol{u^l} = \boldsymbol{u} + \boldsymbol{u^{st}} \tag{2.10}$$

For details on the implementation of equations 2.6-2.10 in ROMS, the reader is referred to Kumar et al. (2012), sections 2 and 3. We will refer to the 2D (depth- and tidally averaged) momentum terms as:

$$\text{ACC} + \text{HADV} = \text{PGF} + \text{COR} + \text{SSTR} + \text{BSTR} + \text{HJVF} + \text{StkCOR} + \text{BRK} \tag{2.11}$$

where each term denotes, respectively, the magnitude of the local acceleration, horizontal advection, the forces associated to pressure gradients, Coriolis, surface stress, bottom stress, the horizontal vortex force, the Stokes-Coriolis force, and the breaking force. Equation (2.11) neglects the horizontal mixing term, while PGF contains the contributions of both $\nabla_\perp \varphi$ and $\nabla_\perp K$ (see equation 2.6).

2.4.2 Idealized simulations and model evaluation

Prior to running the model with realistic bathymetry, we prepared a series of runs in an idealized basin with linearly sloping bottom and depth values similar to Delaware Bay

(2 m – 18 m). The goal of this preliminary assessment is to examine the differences in the wind-driven momentum budget with and without waves under the default implementation of the vortex force formalism presented in Kumar et al. (2012). Results will then be used to inform the more computationally expensive simulations in the bay. The setup consists of a closed basin forced with axial, constant wind (12 m/s) until steady state. The depth distribution $h(x, y)$ is similar to that used in Signell et al. (1990):

$$h(x, y) = H_{max} - (H_{max} - H_{min})\left(\frac{W - y}{W}\right) \tag{2.12}$$

where the depth limits are $H_{max} = 18\ m$, $H_{min} = 2\ m$; $W = 10\ km$ is the basin width, and x, y are the along and across-basin coordinates. The horizontal domain has 50 x 30 grid points and the length of the channel is $L_b = 50\ km$ (figure 2.4).

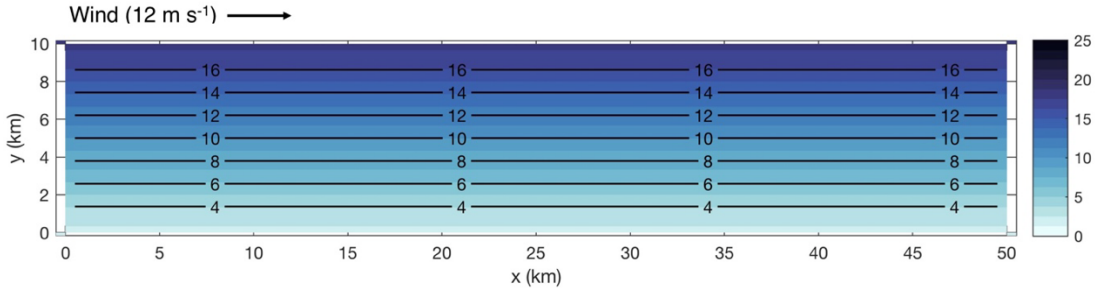

Figure 2.4 Idealized model basin with linearly sloping bottom. Depth units are in meters (colors and contours)

The first idealized simulation is conducted with ROMS without wave coupling and is referred to as 'uncoupled'. The wind stress is calculated according to the COARE 3.0 formulation (Fairall et al., 2003), bottom friction is computed based on a log profile with a roughness length of 1 mm, and turbulent mixing is parameterized according to the $k - \varepsilon$

closure scheme (Warner et al., 2005). The second run is a 'coupled' ROMS and SWAN (COAWST) simulation in which waves are generated by the same axial winds. The effect of waves on currents is considered by activating both the vortex force formalism and the Signell-Sherwood-Warner (SSW_BBL) scheme for bottom boundary layer flows (Warner et al., 2008). Both setups are run until a steady wind-driven circulation is obtained. Results for the wave height, period, surface currents, along-channel transport, and momentum balance terms are presented in figure 2.5.

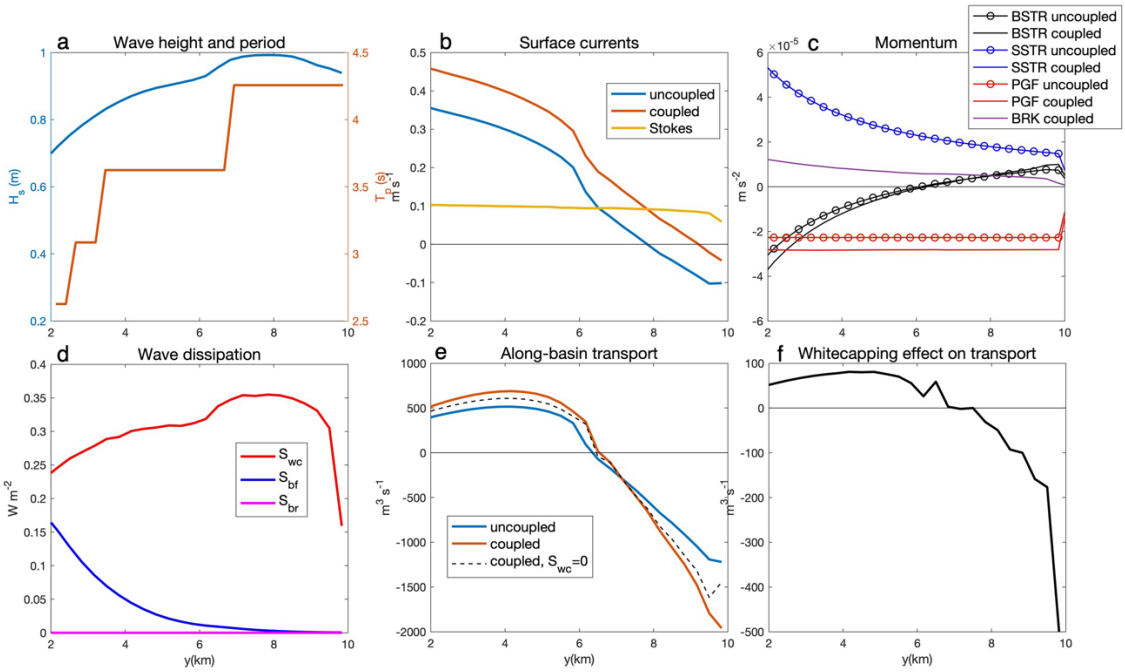

Figure 2.5 Idealized model results. (a) wave height and period for the coupled case, (b) surface currents including the Stokes drift, (c) leading-order steady momentum balance terms: bottom stress, surface stress, pressure gradient force, and breaking force (BSTR, SSTR, PGF, and BRK, respectively), (d) wave dissipation terms in the coupled run, (e) along-basin transport at each grid point, and (f) effect of whitecapping on transport when included in the breaking force scheme. All results are shown as a function of cross-channel distance in the middle of the basin. Positive values for the momentum and transport terms denote downwind direction.

For the coupled run, H_s and T_p are respectively between 0.7 m – 1.0 m and 2.5 s – 4.25 s with values increasing with depth (figure 2.5a). The effect of wave coupling on surface

currents is shown in figure 2.5b. For the uncoupled case, the maximum downwind (i.e. positive) surface current was approximately 0.35 m/s and increased by 29% (0.45 m/s) when waves were included. Note that the plotted surface velocity for the coupled case considers both the Eulerian and Stokes components. The surface Stokes velocity was ~0.1 m/s across the basin (roughly 1% of the wind speed) consistent with wind-generated waves propagating in the downwind direction. Regarding the momentum balance, the downwind SSTR opposes the upwind PGF for both modeled scenarios. However, note that the PGF in the coupled case is 1.25 times higher than the uncoupled PGF. By examining the coupled downwind momentum terms, the increase in PGF is likely due to the BRK term whose net effect is to contribute to the SSTR. The interplay of SSTR, PGF, and BRK over the sloping bottom generates a laterally sheared circulation with downwind depth-averaged flow in shallow water and upwind in the deeper areas, indicative of a topographically induced gyre as reported by Csanady (1973) in long lakes. The separation depth between downwind and upwind transport (6.5 m) is a function of the standard deviation of the cross-channel depth normalized by the mean depth (Hunter & Hearn, 1987). For both scenarios, this sheared circulation pattern is evident in the change of sign in the BSTR term and along-basin transport (figure 2.5e). The overall momentum analysis here indicates that the BRK term may play a key role in wave-driven flows (vortex forces were about two orders of magnitude smaller than the leading terms, and are not shown). According to equation 2.9, the non-conservative wave force (i.e. BRK) depends on both S_{br} and S_{wc}. We show in figure 2.5d that S_{br} is zero while S_{wc} ranges from 0.15 W/m^2 to 0.35 W/m^2, therefore whitecapping is the only dissipation term that contributes to BRK. The impact of full wave coupling on the horizontal circulation can be assessed by calculating the steady downwind transport (T) for each run (Signell et al., 1990):

$$T = \frac{1}{2} \int_{-h(x_*,y)}^{\eta} \int_{0}^{W} \left| u^l(y,z) \right| dydz \tag{2.13}$$

where η is the free surface and $x_* = L_b/2$. Note that the uncoupled scenario considers no wave-induced Stokes velocity and thus u^l reduces to the Eulerian u in that case. Results show that $T = 9.94 \cdot 10^3$ m^3/s for the coupled case, and $T = 7.31 \cdot 10^3$ m^3/s for the uncoupled, therefore the incorporation of waves increased transport by a factor of 1.36. This discrepancy between model runs prompts a closer look at the role of waves on circulation.

Given the results of the momentum analysis, we first consider the BRK term. The notion that a wave-induced force is proportional to dissipation can be traced to a coastal engineering study by Dingemans et al. (1987), who calculated the driving force directly from dissipation instead of differentiating the radiation stress tensor. However, their model setup consisted of a mild-slope nearshore environment in which the leading dissipation terms are expected to be S_{br} and S_{bf} and not S_{wc} since waves were not generated by winds but prescribed at the ocean boundary. Further research on the role of wave energy dissipation on circulation continued over three decades (see e.g. Perrie et al. (2003), Ardhuin et al. (2004), and more recently Aiki and Greatbatch (2014)), but there is some consensus, albeit preliminary, that whitecapping is integrally equivalent to the wind stress under wind-wave equilibrium (Sullivan et al., 2007; Uchiyama et al., 2010). In the light of this evidence, we surmise that including whitecapping as a vertically distributed body force in the budget is unsuitable because the contribution is already included in the wind stress.

Therefore we modify the coupling in ROMS to retain S_{br} as the only contributor for the non-conservative wave force (i.e. we propose to set $S_{wc} = 0$ in equation 2.9). This modification has no impact on wave-induced surface mixing and drag, and is consistent with additional options within the COAWST framework in which the breaking force is computed only based on S_{br} according to formulas by Thornton and Guza (1983) or Church and Thornton (1993) without incorporating wave dissipation from SWAN. For the coupled case considered here, removal of whitecapping led to an adjusted $T = 8.86 \cdot 10^3$ m^3/s and thus the excess wave-induced transport decreased from 36% to 21%. The cross-channel distribution of the whitecapping-induced transport is shown in figure 2.5f. The remaining 21% increase in T with respect to the uncoupled case is then approximately due to the Stokes drift. We consider that this adjustment to the model is appropriate in general for future applications with wind-generated waves.

2.4.3 Numerical experiments with realistic bathymetry

After removing whitecapping from the breaking force, we proceeded with the realistic Delaware Bay runs. We prepared four realistic model configurations to study the role of waves on drag, momentum budget, and circulation in the bay. All model setups use a structured curvilinear grid (20 vertical levels and 1276 by 184 horizontal points with spatial resolution ranging from 440 m at the mouth to 6 m in the river), and bathymetry from a composite of recent soundings by NOAA and the U.S. Army Corps of Engineers (last updated 2014, depth distributions shown in figure 2.1). The oceanic open boundary is located on the inner continental shelf while the northern edge of the domain corresponds to the head of the tides (km 220 in figure 2.1b).

ROMS benchmark runs:

The goal of the benchmark runs is to explore the role of winds in the momentum balance and subtidal exchange of the bay without waves. Two cases are considered here, one with up-estuary and another with down-estuary winds according to the wind rose in figure 2.2a (13 m/s with directions 124° and 304° respectively). Tidal forcing (M2 constituent) is obtained from the ADCIRC database (Luettich et al., 1992). The surface stress is calculated according to the COARE 3.0 algorithm in which the surface drag coefficient is a function of wind speed (Fairall et al., 2003).

Coupled ROMS and SWAN (COAWST) runs:

The coupled runs employ the same parameters and forcing as the benchmark (M2 tides, 124° and 304° winds), and incorporate a previously validated SWAN configuration of the bay to compute the effect of waves on currents and drag (Chen et al., 2018). The coupled model has several options to consider waves on air-sea drag. The steepness-based parameterization of Taylor and Yelland (2001) was found to perform well with many datasets except in short-fetch and young sea conditions (Drennan et al., 2005). Since the Delaware wave field has fetch-limited shadow zones, we considered that option unsuitable. The wave age-based parameterization from Oost et al. (2002) was found to overpredict surface currents under hurricane winds (Olabarrieta et al., 2012). In this study, we used Drennan's parameterization (2), which had a good performance in wind-sea rough flows (Drennan et al., 2003; Drennan et al., 2005). The bottom friction algorithm (SSW_BBL) includes wave-current interactions (Warner et al., 2008), and the wave-induced forces are computed with the vortex force formalism without whitecapping. Surface mixing accounts for wave breaking according to Craig and Banner (1994) as implemented by Carniel et al.

(2009). Since previous studies have shown that the bay is sheltered from remote swell (Kukulka et al., 2017; Chen et al., 2018), we neglect wave forcing at the open boundary.

To perform the runs with a realistic spatial density distribution, a climatological salinity field (Levin et al., 2018) is ramped up under median river discharge in the Delaware River (350 m^3/s) for 60 tidal cycles. The evolved salt field is then used as initial condition for the runs we analyze here. Wind forcing (with wave generation for the coupled runs) is then prescribed for 5 days, consistent with previous studies of wind driven circulation in a similar coastal environment (Whitney & Codiga, 2011). We use input parameters and advection schemes from a previously validated model setup of the bay (Chen et al., 2018), and further details can be found there.

2.5 Results and discussion

In this section we will investigate the role of wind waves in drag and momentum budget of Delaware Bay. The focus here is to illustrate how waves change the magnitude of drag and momentum budget terms, therefore we will consider the up-estuary wind case in most of the discussion for brevity. We will then explore the impact of waves on the bay-ocean exchange and will consider both wind and wave directions.

2.5.1 Wind waves and surface stress

The wind input for wave energy S_{in} and the surface drag coefficient C_D (equations 2.1-2.3) involve dependencies on the wave age, phase speed, height, and frequency. Since the bay features a complex bathymetric and geometric configuration with channels, ridges, and a narrow river, it is important to discuss the extent of wind-wave equilibrium under typical wind conditions. To assess the wave equilibrium in the study region, Chen et al. (2018) obtained the stationary, infinite-fetch wave height for a range of depths typical of the bay and compared the results against the simulated heights in a realistic Delaware domain under up and down-estuary winds. The authors identified that fetch and steeply sloping bathymetry were the main factors that lead to local disequilibrium. In terms of fetch, the study indicates that at least 10 km are necessary for local wind waves to fully saturate in a water column 4 m deep. The latter explains the relatively small wave heights in the narrow river north of 39.5 N (about 0.5 m as shown in figure 2.6a). In the lower bay, the study indicates that wave heights are in equilibrium and near-equilibrium with local wind and depth during typical storm conditions, with the exception of highly localized steep ridges where the depth profile changes more rapidly than waves can adjust. While the assessment of wave equilibrium from Chen et al. (2018) did not incorporate tidal forcing, the impact of wave-current interactions on wave height and near-equilibrium conditions is expected to be modest according to Kukulka et al. (2017), who reported that currents modulated average wave statistics by about 15% in Delaware Bay.

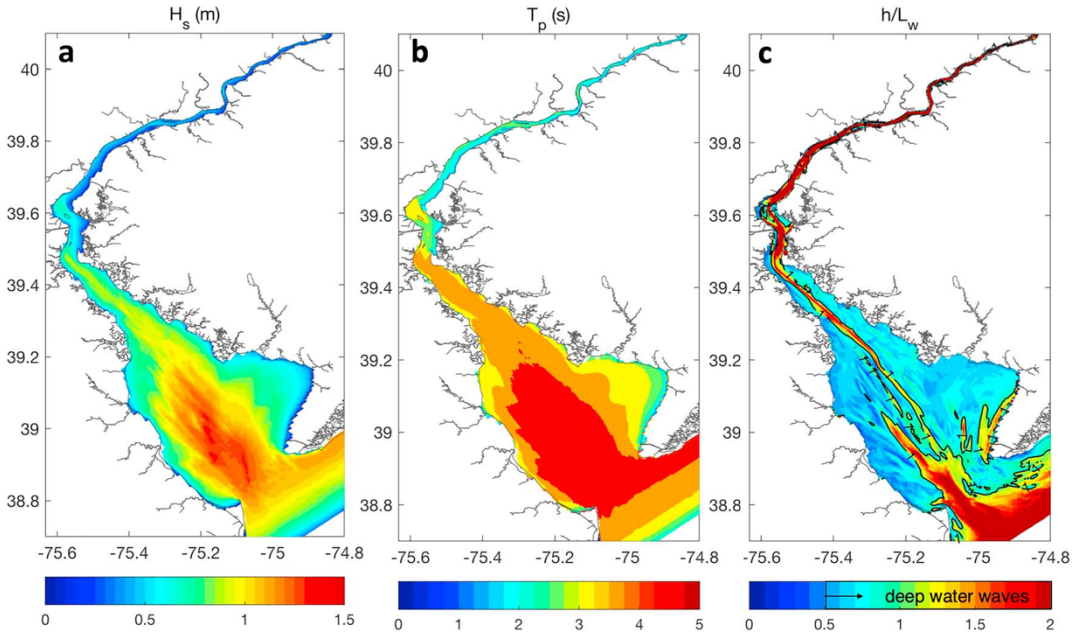

Figure 2.6 Modeled spatial patterns of tidally averaged (a) significant wave height, (b) peak period, and (c) ratio of water depth to wavelength from the coupled model and up-estuary winds. The black contour in (c) denotes the basin-wide median value of h/L_w, and the colorbar highlights values for deep water waves.

In the present study, the tidally-averaged significant wave height (H_s) mirrors the broad basin topography with maximum values in the deepest regions of the lower bay ($H_s \sim 1.5$ m, figure 2.6a), and reflects the findings by Chen et al. (2018) regarding equilibrium and disequilibrium conditions. Wave heights at shoreline edges in the lower bay were relatively small ($H_s \sim 0.25$ m), which is indicative of enhanced energy dissipation through bottom friction and whitecapping as waves propagate onshore. Note that the slight reduction of wave height and period from the mouth to the oceanic boundary of the model (figure 2.6a) is indicative of a fetch artificially limited by the model grid for up-estuary winds rather than a physical response. Topography also modulated the peak wave period T_p (figure 2.6b), which ranged from 3 s to 4 s in the lower bay to 1-3 s in relatively shallow regions. The basin-wide median ratio of local depth to wavelength (h/L_w) was 1.03 with a minimum 0.12, which indicates that waves in the estuary are predominately dispersive ($h/L_w > 0.5$,

figure 2.6c), and therefore that the phase speed is mainly a function of wavelength, $c_p \approx \sqrt{gL_w/2\pi}$.

The topography and fetch-controlled wave height field was also reflected in the spatial structure of the S_{in}, which ranged from 0.8 W/m^2 on subtidal flats and to ~1.3 W/m^2 in the lower bay (figure 2.7a). A close examination of the wind input expression can provide insight into the nature of these results. As shown in equation 2.3, S_{in} depends on an exponential growth term (B) that is proportional to inverse age, wind and wave direction, and frequency. Model results indicate that the wind-wave direction misalignment due to topographic and current-induced refraction ($\theta - \theta_w$, not shown) was about 15°, which modulates B spatially by 5%. Values of B in the bay therefore decrease with increasing depth following the drop in σ and u_*/c_p as waves become older, longer, and more dispersive (figure 2.7 b, c). Values of the inverse age in the bay (figure 2.7b) are ~0.13 in deep water and ~0.2 over subtidal flats, (ages ~7.7 and ~5, respectively), therefore the sea is underdeveloped (age < 33, or 'young'). However, S_{in} is greatest in deeper water where the older, longer waves are located, suggesting that wave height is the main controlling variable in the energy transfer from winds to waves. Note that in the wind input term, B is multiplied by the energy spectrum E, which is proportional to H_s^2. Simulation results then indicate that under spatially homogeneous wind speed and direction the net wind energy transfer to the wave field in the bay depends largely on depth and fetch through their controlling effect on wave height.

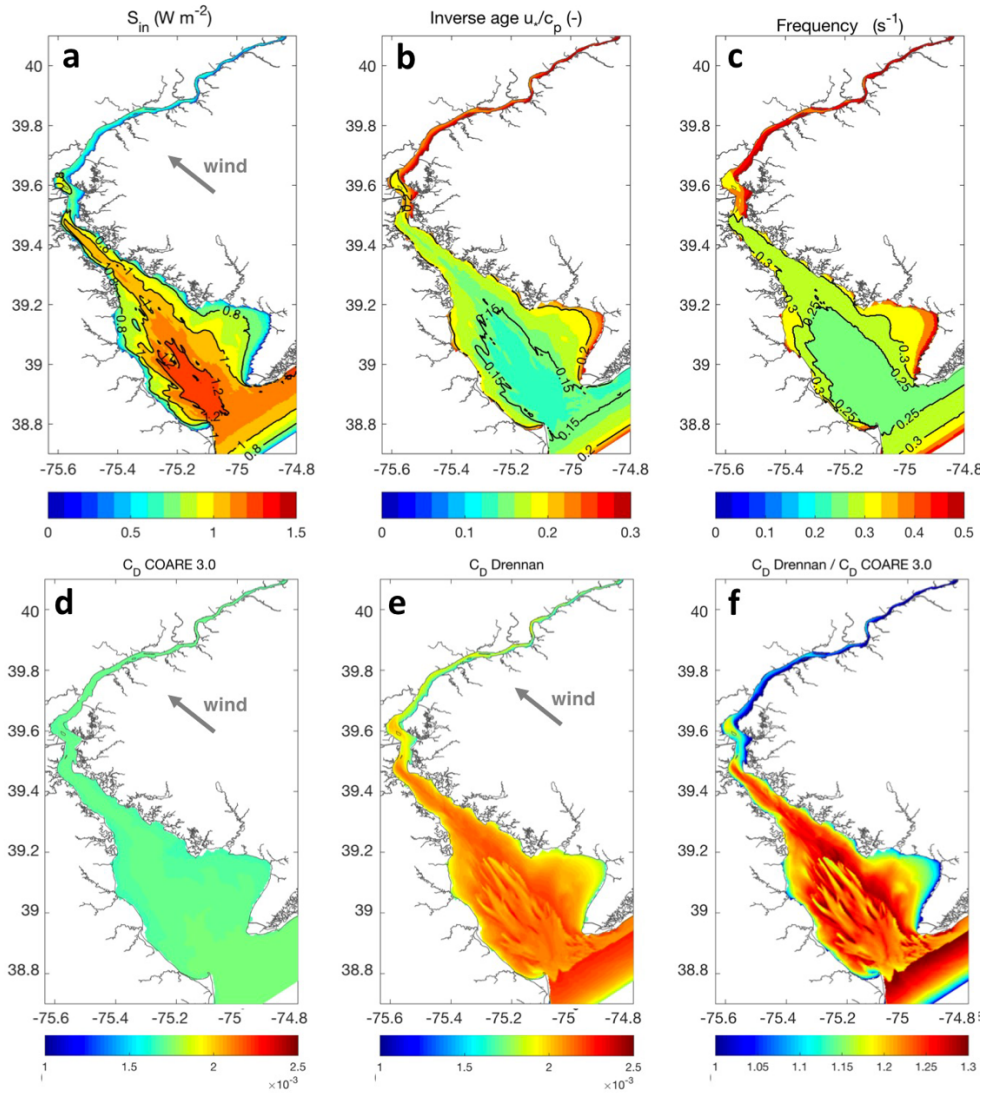

Figure 2.7 Air-sea wave coupling in Delaware Bay. (a) Wind input for the wave action balance, (b) inverse wave age, (c), wave frequency, surface drag coefficient according to (d) the COARE 3.0 algorithm and (e) the inverse wave age and height (Drennan) parameterization. The ratio between drag coefficients is shown in (f).

While the simulation under constant wind speed and direction allows a basic analysis of the variables that control wave growth, it is relevant to note that wind direction can also change rapidly and increase wind-wave misalignment during certain weather events. Field observations (figure 2.3) indicate that the wind-wave direction misalignment was approximately 60° between October 31st and November 2nd when the wind vector changed

direction from 250° to 300°. Intuitively, increasing values of misalignment would reduce B through the cosine term in equation 2.3, damping wave growth. However, there are additional wave dynamics that can result from veering winds, especially in estuaries and similar environments where wind direction and coastline configuration determine fetch. For instance, a changing wind direction can increase the fetch (Donelan et al., 1985) and bring local wind seas closer to saturation. In estuaries such as Chesapeake Bay, the misalignment between wind and waves due to the basin geometry is translated into a wind stress divergence at the air-sea surface (Fisher et al., 2017).

In addition to exploring air-sea wave energy coupling, we now present results of the surface drag coefficient for modeled scenarios without and with waves. In the uncoupled scenario, C_D was calculated according to the COARE 3.0 algorithm in which Charnock's alpha is only a function of wind speed (figure 2.7d). As expected, the drag coefficient for that case was spatially homogeneous ($C_D \sim 1.6 \cdot 10^{-3}$). In contrast, the coefficient in the coupled run ranged from $1.6 \cdot 10^{-3}$ in relatively shallow water to $2.3 \cdot 10^{-3}$ in the main channel and adjacent continental shelf (figure 2.7e). The spatial pattern of C_D in the coupled scenario is complicated by the counteracting effects of wave height and age in the bay. As described in the discussion on S_{in}, wave heights are maximum where the inverse age is minimum, which explains the slight reduction of drag towards the lower bay where the sea is relatively older. The ratio between the two drag coefficients (figure 2.7f) indicates that C_D was up to 30% higher in the coupled run. In the upper tidal river where fetch limitation and a narrow channel severely limit wave growth, the drag coefficient remained nearly unchanged with the wave coupling.

The effect of waves on surface drag in estuaries was also studied in regions where basin geometry and prevailing wind direction are more conducive to fetch limited wave growth compared to Delaware Bay. An example is Chesapeake Bay, where Fisher et al. (2015) analyzed the impact of wave age on C_D based on observations and numerical modeling. Their study reports that the turbulent roughness length in the Chesapeake follows the relationship $z_r g/u_*^2 = A_c\left(u_*/c_p\right)^{B_c}$ with $A_c = 0.137$ and $B_c = 0.928$ as empirical constants, in contrast to deep ocean, unlimited fetch conditions where $A_c = 0.114$ and $B_c = 0.622$ (Edson et al., 2013). While Fischer's roughness parameterization does not explicitly include wave height as in Drennan's model (2.2), the spatial distribution of the wave-influenced C_D was comparable to that in Delaware Bay, as it also ranged from $1 - 2.5 \cdot 10^{-3}$ under slightly lower wind speeds (~10 m/s). Similarly, they found departures in the wave-induced C_D of up to 20% with respect to a drag formulation that depends only on wind speed. Other authors found that the measured drag coefficient at a nearshore tidal inlet was 2.5 times higher than the predicted open ocean 'bulk' value under moderate (> 5 m/s) winds (Ortiz-Suslow et al., 2015). The discrepancy in the Delaware model results was less, perhaps because the model grid does not spatially resolve the surf zone. Both the observational evidence in other systems and our model results indicate that waves can play an important role in the surface drag distribution of shallow, fetch limited environments.

Although the up-estuary wind case illustrates the typical response of C_D to the wave field, it is important to briefly address the role of wind direction in the spatial distribution of surface drag. The modeled C_D for the down-estuary wind-wave scenario and the increment factor with respect to the COARE 3.0 formulation are shown in figure 2.8. The spatial distribution is similar to the modeled up-estuary C_D (figure 2.7 e, f) in that the drag

increases from the shorelines to the middle of the bay, with finer spatial patterns imposed by bathymetry through its control on H_s and u_*/c_p. Another similarity between the two cases is the dominance of below-equilibrium conditions in the narrow river where fetch-limited waves also had a modest (<10%) impact on drag. The main difference between the up-estuary and down-estuary wave-induced C_D distribution is in the region between the mouth and the oceanic boundary of the model. Since the wind blows towards the open boundary in this case, the wave field is not affected by artificial fetch limitations. The slight decrease in drag from the mouth towards the shelf in this case is not due to the proximity of the model boundary but because wind waves in the inner shelf are able to grow older than inside the bay. The seaward reduction of C_D is this area (about 22% from mid-bay to the shelf) therefore suggests that wave age and not height dominates the surface roughness. While the model captures the basic roughness dynamics that would take place on the inner shelf under purely wind-driven conditions, the surface drag in a more realistic situation would be affected by swell (e.g. mixed sea conditions). In that case, swell would complicate the purely wind-sea drag by accepting or releasing momentum at the air-sea boundary as a function of wind speed (Garcia-Nava et al., 2012). However, the transition from mixed conditions to swell-sheltered estuarine wind seas is beyond the scope of the present work. Later we will examine the implications of the extra wave-induced surface drag for the momentum budget and residual circulation in the bay.

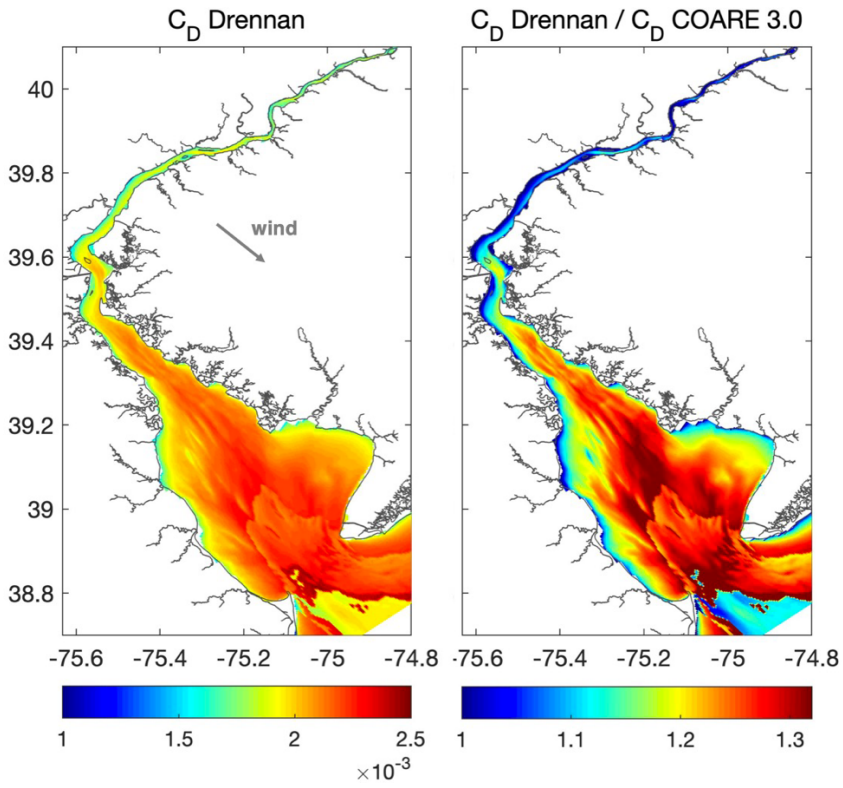

Figure 2.8 (Left) Surface drag coefficient for down-estuary winds based on the Drennan parameterization. (Right) increment factor with respect to the COARE 3.0 formulation.

2.5.2 Wind waves and bottom stress

Following the examination of air-sea wave coupling, we now consider the impact of waves in the bottom boundary layer. The spatial distribution of root-mean-squared (RMS) bottom current and wave stresses is shown in figure 2.9. Current stresses (τ_c, figure 2.9a) were relatively important in the thalweg north of 39.2 N ($\sim$ 1 N/m^2), consistent with the effect of topographic funneling on tidal current amplification (Friedrichs & Aubrey, 1994), and also in the bay's mouth due to the forced flow curvature as tides enter the bay. In the lower bay area, current stresses were 0.4 N/m^2 -0.6 N/m^2 in the deeper regions and <0.2 N/m^2 over shoals, which suggests that most of the momentum is conveyed in the relatively deep channel. In contrast, wave-induced stresses were only important in very shallow regions of the bay (figure 2.9b), especially over shoals and along linear ridges as reported

by Chen et al. (2018) under higher wind speeds. Wave stresses on top of ridges in the lower bay (~1 N/m^2) were comparable to the current stresses in relatively deeper water.

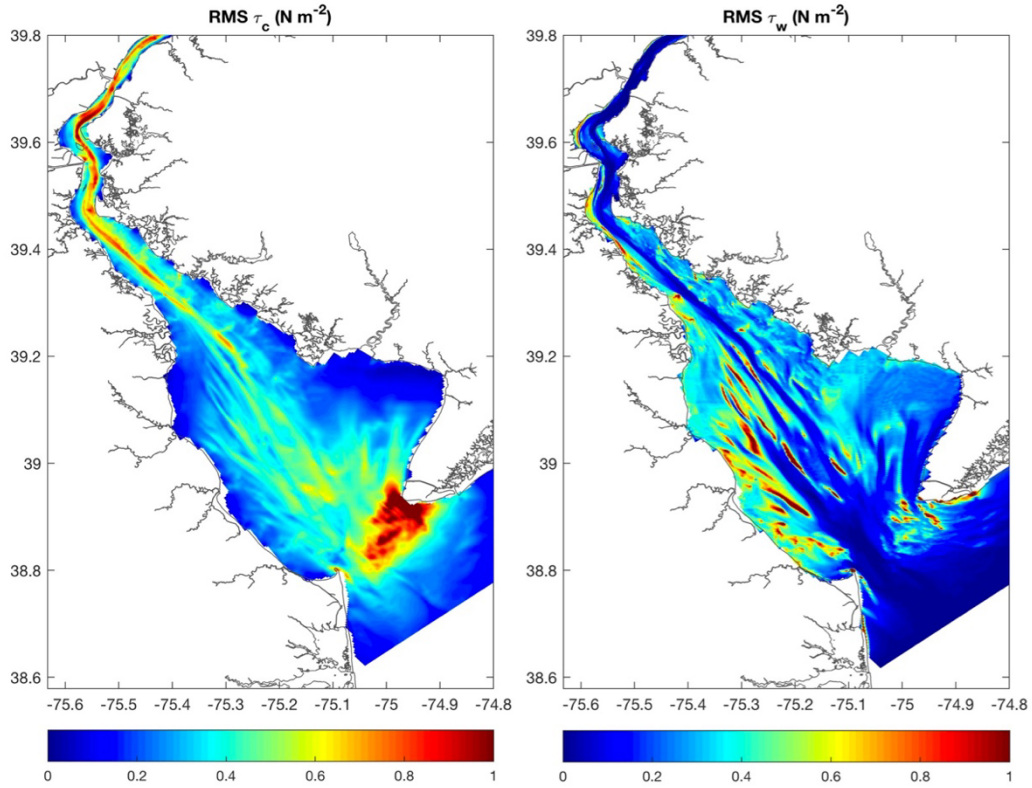

Figure 2.9 Root-mean-squared (a) current bed stress τ_c and (b) wave-induced bed stress τ_w under up-estuary winds

Since wave stresses were highly localized and over areas that do not convey most of the momentum, the impact of the enhanced bed drag on the overall tidally and wind-driven circulation was relatively small. A similar case was observed in San Francisco Bay where wave-current interactions in the bottom layer had a little impact on tidal propagation (Bricker, 2003). However, the spatial distribution of the wave stresses would have a direct impact in sediment resuspension and transport since the surface erosion flux is proportional to the difference between the maximum stress $\tau_{b,max}$ and the critical erosional stress for

each sediment class (sand, silt, or clay) present in the bed (Warner et al., 2008). The resulting wave-driven sediment erosion during storms would contribute to the along- and cross-bay sediment budgets of the bay, which are usually dominated by mean advection and tidal pumping (Sommerfield & Wong, 2011; McSweeney et al., 2016a). In addition, enhanced water column turbidity due to waves could impact light availability and biological productivity at storm time scales Cho (2007); (McSweeney et al., 2016b), but the response of bed sediment to wave forcing is outside the scope of this work.

2.5.3 Water column momentum budget

In the previous two sections we analyzed the variability of surface and bottom stresses in the context of wind generated waves. Next we explore the spatial distribution of the mean (tidally and depth-averaged) momentum budget in the coupled and uncoupled runs under up-estuary winds. One of the main features of the coupled model is the inclusion of the Stokes drift in the velocity field. In the Delaware, the mean surface Stokes velocity was 0.16 m/s on shallow flats and 0.18 m/s in relatively deeper areas of the lower bay (figure 2.10), similar to the results of the idealized model assessment, and consistent with Kenyon (1969) who reported that the magnitude of the surface Stokes drift is 1% to 3% of the wind speed. Since the Stokes velocity drops exponentially in the vertical, the associated water mass transport was confined to the upper 10-15% of the water column (vertical e-folding scale ~1.5 m). The model also indicates weak tidal modulation (about 10%) of the Stokes drift in the basin given the modest response of the wave field to currents, especially in the deep channel.

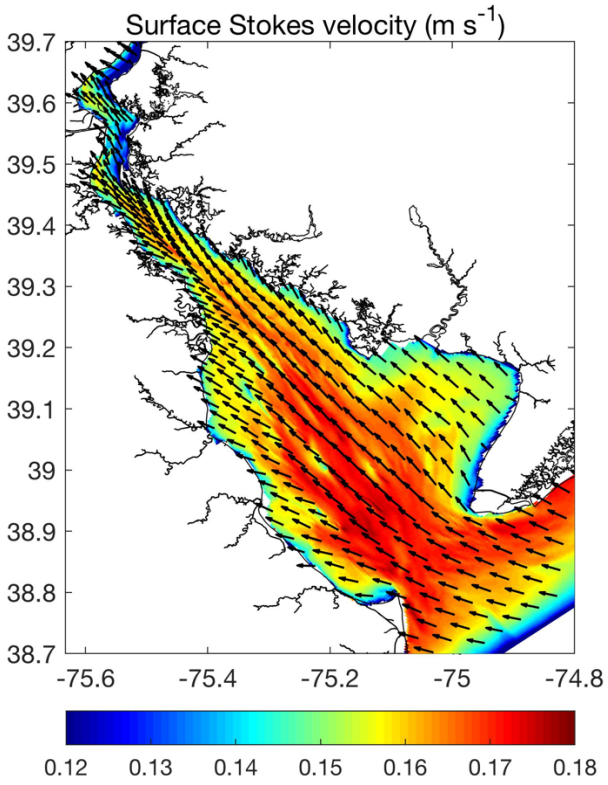

Figure 2.10 Tidally-averaged surface Stokes velocity (arrows) with magnitude in colors (m/s) for the coupled, up-estuary wind run.

The leading order momentum terms in the bay are the surface stress, pressure gradient force and, to a lesser extent, bottom stress (SSTR, PGF, BSTR) during the modeled wind event. Their spatial distribution is shown in figure 2.11 for the scenarios with and without waves. In the case with no waves, the SSTR term was modulated by topography given its inverse relationship with depth ($\tau_s/\rho h$), and its magnitude was ~1.5 x 10^{-4} m/s^2 in shallow shoals and ~0.5 x 10^{-4} m/s^2 in the deeper channel. When waves were considered, the SSTR magnitude increased by a factor of 1.1-1.3, consistent with the increase in surface drag presented in section 2.4.1. The spatial pattern of PGF mirrored the SSTR with nearly similar values, which suggests that the main momentum balance was between these two terms. As a result, the increase in SSTR under wind waves was reflected in an adjustment in the PGF,

which also increased by factors between 1.1-1.3 with respect to the run with no waves (figure 2.11, bottom row). The along-thalweg mean elevation increased by about 11% (0.66 m to 0.72 m over the thalweg length, 190 km).

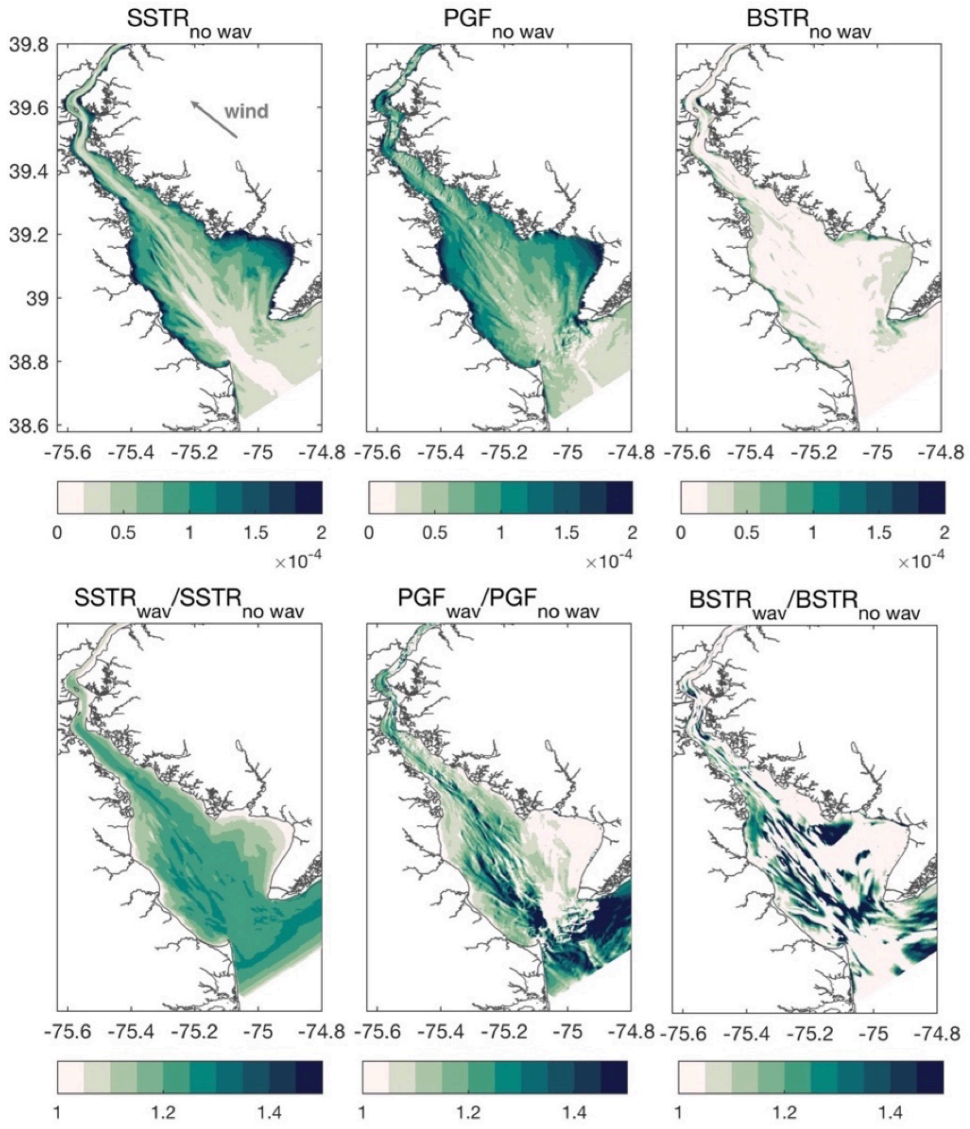

Figure 2.11 Leading order momentum balance terms in the bay. (Top row) tidally and depth averaged surface stress, pressure gradient force, and bottom stress terms (SSTR, PGF, and BSTR) in the scenario of up-estuary winds with no waves. (Bottom row) increment factor for each term when waves are included in the model. The magnitude of each term is color coded (m/s^2).

The phase-averaged momentum equations in the vortex force formalism (equations 2.6-2.7) indicate that waves can also contribute to the PGF by incorporating the gradient of the quasi-static elevation and of the Bernoulli head, neither of which were significant here. The BSTR term was on the same order of magnitude as the SSTR and PGF, but it was comparatively small throughout the basin and its magnitude did not exceed 0.5 x 10^{-4} m/s^2 on shallow shoals and 0.16 x 10^{-4} m/s^2 in the deep channel for the uncoupled run. The BSTR increment factor under waves was ~1.2-1.3, mainly in relatively shallow areas and shoals, but the leading balance between PGF and SSTR still held for most of the basin.

The spatial distribution of horizontal vortex forces, breaking forces, and Stokes-Coriolis forces (HJVF, BRK, and StkCOR) is shown in figure 2.12. Vortex forces were present in areas of relatively high lateral shear (i.e. along the edges of linear ridges and at bathymetric transitions from shoals to deeper channels), but the overall contribution to the budget was modest and an order of magnitude smaller than the leading order terms. The StkCOR term, which scales with $fu_{st}/h \approx 10^{-4} \cdot 10^{-1}/10^{0} = 10^{-6}$ m/s^2, was also small compared to leading order O(10^{-4} m/s^2) terms. In contrast, breaking forces were O(10^{-4} m/s^2) on highly localized shallow ridges and nearshore regions in the lower bay, and zero in the rest of the basin. As described previously, the magnitude of the BRK term only depends on the depth-limited wave breaking dissipation (S_{br}), which is a function of the topographically constrained factor $\beta = H_{rms}/\gamma h$ ($\gamma = 0.8$ is the breaker parameter). According to the bore model by Battjes and Janssen (1978) used in this study, the fraction of depth-limited breaking waves is set to zero on grid points where $\beta \leq 0.2$. Values of β in Delaware Bay during the simulated storms range from 0.05 in the channel and 0.15 on shallow flats, which explains the highly localized spatial distribution of the breaking term.

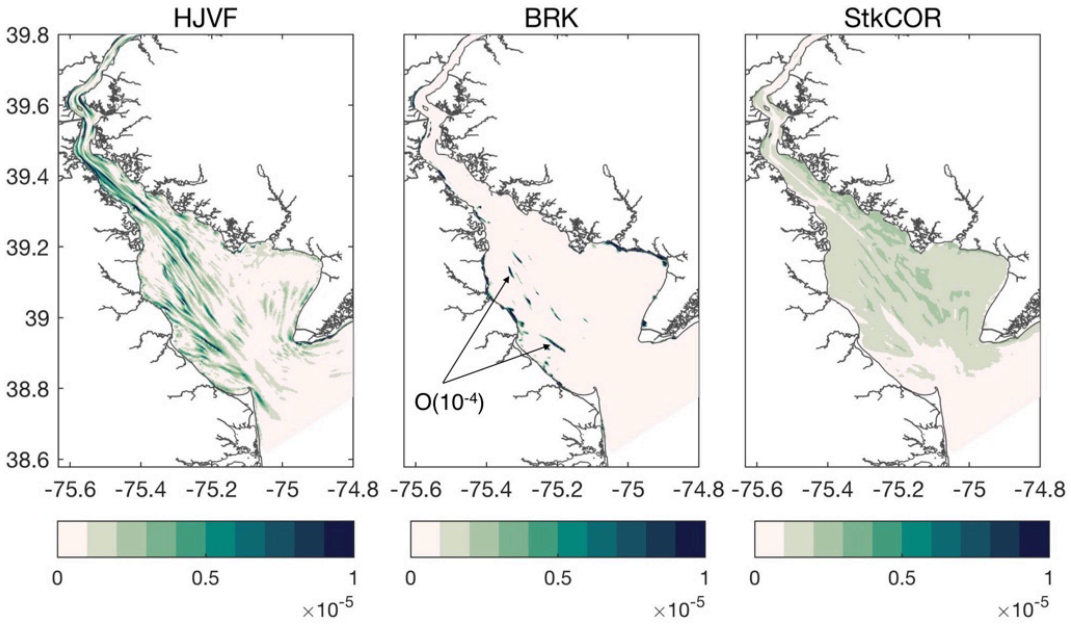

Figure 2.12 Wave induced momentum budget terms in the bay: horizontal vortex forces, breaking force, and Stokes-Coriolis force (HJVF, BRK, StkCOR). The magnitude of each term is color coded (m/s^2). Note these terms are $O(10^{-5})$.

Analysis of the momentum budget with and without waves indicates that even if wave-induced forces are small in shallow basins, waves can impact the mean momentum budget by altering drag and by incorporating Stokes drift to the velocity field. The role of waves on drag can be important in systems such as Delaware Bay because of the broad spatial distribution of the wave height and age. The Delaware differs from other coastal systems such as back-barrier estuaries, tidal inlets, and coral reefs (see e.g. (Uchiyama et al., 2010; Olabarrieta et al., 2011; Olabarrieta et al., 2014; Beudin et al., 2017; Rogers et al., 2017)) in that that waves are mainly local and wind-generated instead of remote (Chen et al., 2018), and in that the bathymetric distribution is the result of both natural and anthropogenic processes. The latter leads to distinct patterns in the wave-driven momentum budget. Steep bathymetric transitions from shoals to dredged channels

generate velocity gradients that interact with the Stokes drift to create local vortex forces. In the Delaware, wave breaking forces are zero at the relatively deep mouth (>20 m deep, 20 km wide) and are only important on shallow, linear ridges inside the embayment due to local waves. The opposite is true for example in New River inlet where the mouth is relatively shallow (5 m deep, 1 km wide), which forces remote waves to break and inject momentum to the water column, enhancing subtidal flows (Wargula et al., 2014).

2.5.4 Subtidal exchange

While the contribution of Stokes-Coriolis, breaking, and vortex forces to the mean budget was modest, now we explore how subtidal flows can change mainly due to the increases in surface drag and the inclusion of Stokes drift. In this section, we consider all benchmark and coupled runs since the residual patterns are sensitive to wind direction (up and down-estuary winds, with and without waves). The horizontal transport (m^3/s) was calculated in northward (T_N) and eastward (T_E) components at each grid point through the product of the depth-dependent velocity, the fixed grid cell width ($\Delta x, \Delta y$), and the time-varying vertical thickness (δ) according to:

$$T_E(x,y,t) = \sum_{i=1}^{20} u_{iE}^{l}(x,y,z,t)\ \delta_i\ (x,y,z,t)\ \Delta y \tag{2.14}$$

$$T_N(x,y,t) = \sum_{i=1}^{20} u_{iN}^{l}(x,y,z,t)\ \delta_i\ (x,y,z,t)\ \Delta x \tag{2.15}$$

where u_{iE} and u_{iN} are the eastward and northward Lagrangian velocities at the i-th layer, and the summation is performed over the 20 vertical levels. This method calculates the transport by following the time-varying water column thickness instead of utilizing the resting basin depth. To compute the residual exchange, each component was averaged over the duration of the wind event (5 days), and the results are shown in figure 2.13 for the spatial patterns and in figure 2.14 for the mean transport through two cross-sections of the bay.

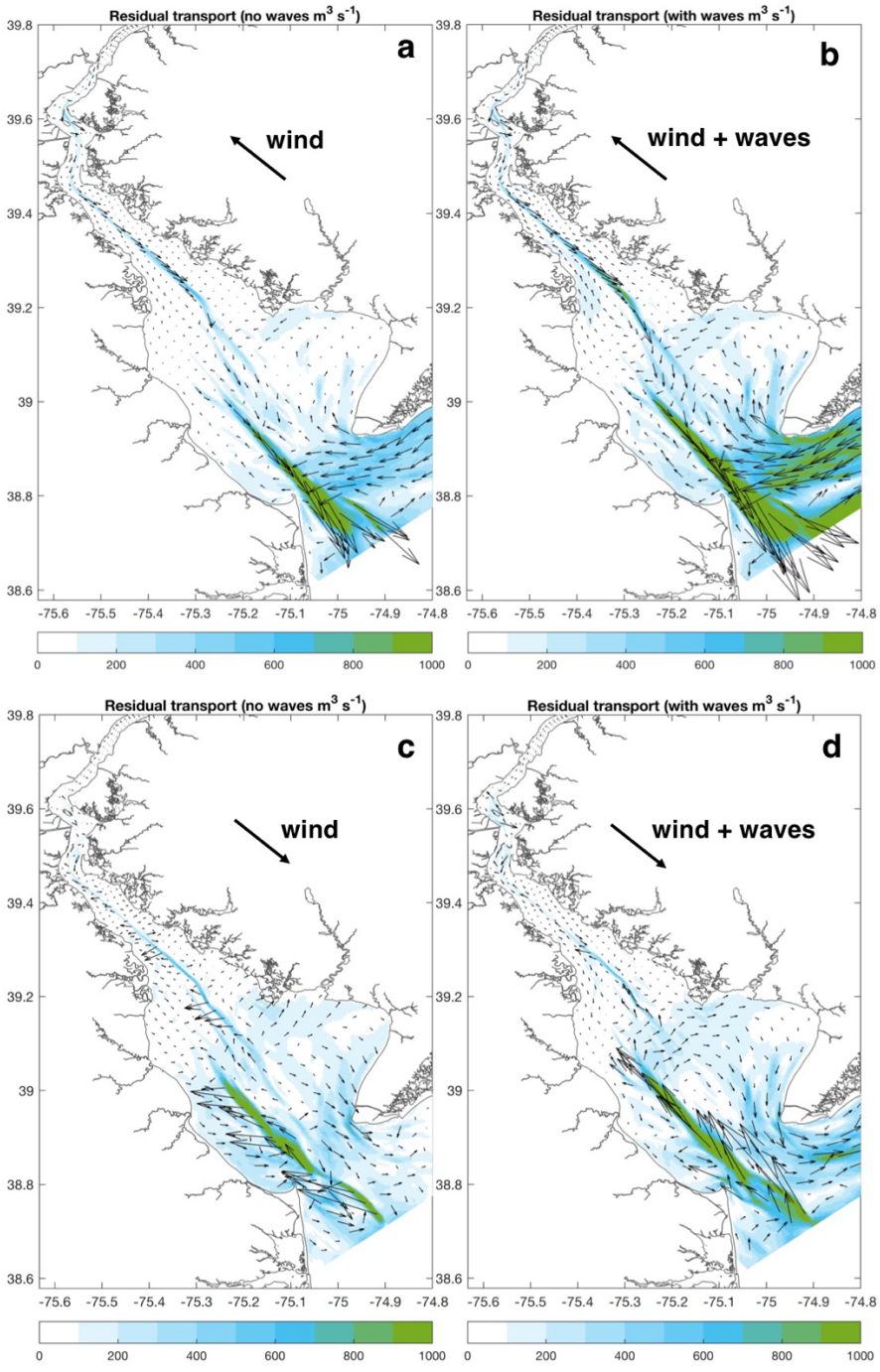

Figure 2.13 Modeled residual circulation (arrows) for the up-estuary (a, b) and down-estuary wind and wind-wave scenarios (c, d). Residual transport magnitude is shown in colors.

For the up-estuary wind-only scenario, the subtidal transport features a laterally sheared circulation with inflow in the flanks and outflow in the deeper channels. The obtained laterally sheared mean flow is consistent with the expected residual pattern in a long basin with tides (Li & O'Donnell, 2005; Winant, 2008), and in a shallow, wind-driven basin with sloping bathymetry where the flow is downwind in the shallows and upwind in the channel (Csanady, 1973; Signell et al., 1990). The subtidal bay-ocean exchange here is facilitated by a counterclockwise gyre in the lower bay. When waves are incorporated to the up-estuary wind scenario (figure 2.13b), the subtidal inflow and outflow increase by a factor of 1.2-1.5. This increase can also be seen in figure 2.14 where the residual transport under wind waves across the mid and lower bay was 1.2-1.5 times the transport obtained in the wind-only cases. The role of waves in this departure can be explained mainly by the adjustment of the pressure gradient force to the increased surface stress and by the up-estuary wave-induced Stokes transport.

In the down-estuary wind scenario (figure 2.13c) the transport pattern indicates inflow in the deep thalweg and outflow in the flanks, and the subtidal exchange magnitude is smaller than in the case with up-estuary winds by nearly 30%. Note that in the up-estuary wind case the wind-driven flow enhances the tidal residual circulation (i.e. both lead to inflow in shallow water and outflow in the channel) while the down-estuary wind driven circulation is in the opposite direction of the tidal residual. When waves are included in the down-estuary wind case (figure 2.13d), the magnitude of the exchange increases in response to the adjustment between PGF and SSTR. However, that increase in magnitude was not as noticeable as in the up-estuary wind-wave case since the wind driven circulation still goes against the direction of the tidal residual. For example, the peak transport in the

thalweg was ~2500 m^3/s for the up-estuary wind-wave case and about 2000 m^3/s for the down-estuary wind-wave case.

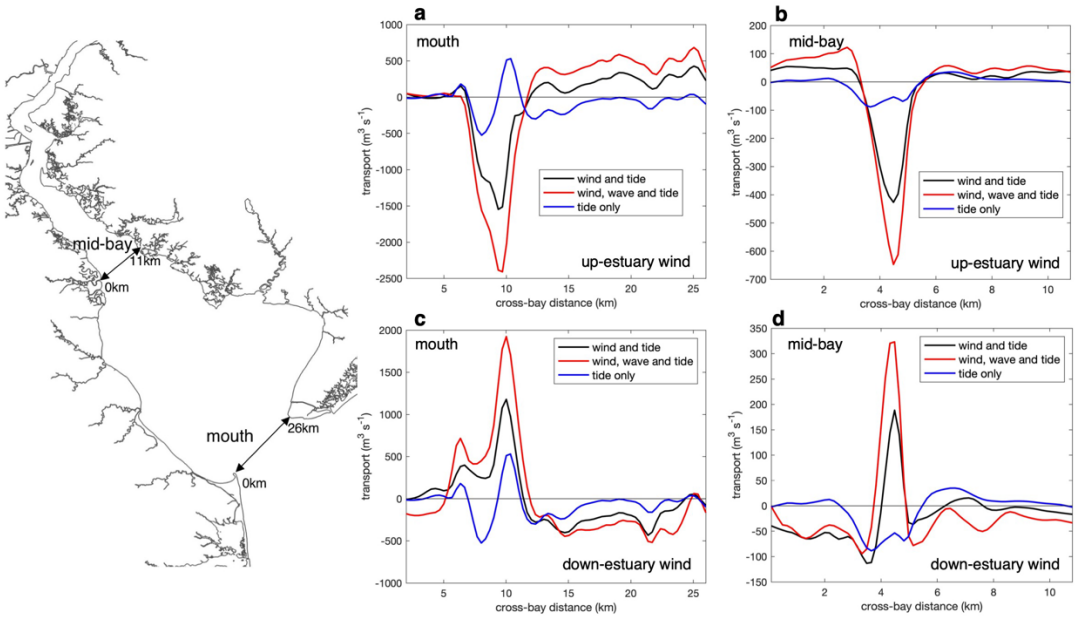

Figure 2.14 Depth-integrated residual exchange at two cross-bay transects for the modeled up-estuary (a, b) and down-estuary (c, d) wind scenarios. Transect locations are shown on the map. Transport values are plotted for the coupled scenario (wind, wave and tide) and for the uncoupled one (wind and tide). The residual transport in the absence of wind and waves (labeled as tide-only) is shown in all panels for reference.

2.6 Summary and conclusions

In this work we used a numerical model to assess the impact of wind generated waves on boundary layer stresses, wave-induced forces, and residual circulation in shallow coastal plain estuaries with Delaware Bay as a generalizable example. An assessment of the vortex force formalism in an idealized basin was performed to explore the impact of wave energy dissipation on circulation. Model results suggest that the whitecapping-induced breaking

force double counts the contribution of the wind stress in the Reynolds-averaged momentum budget. Therefore, we altered the original model formulation to prevent whitecapping from generating breaking forces. This modification is consistent with previous studies on nearshore currents and with additional options to compute breaking forces in the model, which only consider the depth-limited breaking dissipation for the force. Instead, we considered the impact of waves on the surface drag coefficient by using a parameterization that is suitable for young, wind-driven seas where the wave field evolution is limited by local topography. When a wave-induced surface drag formulation was employed, the drag coefficient increased by a factor of 1.3 with respect to a drag coefficient that is only a function of wind speed. While 'bulk' surface drag formulations have been extensively used for a range of marine environments, here we show that they do not capture the spatial variability that has been reported in previous observational studies of air-sea fluxes in estuaries and similar fetch-limited environments. In estuaries such as Delaware Bay, the impact of waves on surface drag is significant for subtidal exchange at storm time scales. Tidally averaged horizontal transport patterns differ by a factor up to 1.5 when waves are included, and are sensitive to wind direction. Regarding the momentum budget, vortex forces were present at bathymetric transitions from shoals to channels given their dependency on velocity gradients, but their contribution to the budget was quite modest and an order of magnitude smaller than the leading order terms (surface stress, bottom stress, and pressure gradient). Stokes-Coriolis forces were also negligible and did not significantly contribute to the mean budget. The breaking force (i.e. from depth-limited breaking dissipation) term was leading order only on steep ridges in the lower bay, therefore its net impact in the basin momentum distribution was also small. Results here motivate the consideration of wave coupling and the usage of a suitable wave-

induced surface drag coefficient formulation in studies of storm-driven circulation in estuaries.

Chapter 3 - Impact of Historical Channel Deepening on Tidal Hydraulics in the Delaware Estuary

3.1 Abstract

Tidal amplification and damping in estuaries, which result from the competition of friction and convergence, are strongly dependent on basin morphology and shoreline configuration. Humans have significantly altered the morphology of estuaries and tidal rivers through the creation of shipping channels and coastal structures, and the response of tides to these modifications has implications for flooding, pollutant dispersion, and sediment transport. In this study, we assess the impact of long-term channel deepening on the barotropic dynamics of the Delaware Estuary, a convergent estuary on the east coast of the United States. Historical (1848) and modern (2014) depth soundings are digitized and gridded for use in a numerical model of the bay. Numerical simulations indicate a doubling in tidal range near the tidal limit, shifts in the arrival time of high water, and changes in elevation-velocity phase. A historical increase in the upstream conveyance and transmission of energy is consistent with bigger amplitudes, swifter currents, and more progressive wave dynamics in the shipping channel. A scaling analysis of momentum and continuity equations indicates that frictional effects depend on local depth to the 3/2 power.

3.2 Introduction

Over the last century, the increasing demand for ecosystem services has accelerated the anthropogenic intervention of rivers and estuaries through the construction of coastal structures, floodplains, and shipping channels (Oliveira et al., 2006; Liria et al., 2009;

Morelli & Gasparon, 2015; Marmin et al., 2016; Wang et al., 2016). In the United States, the need for navigation in many urbanized estuaries led to extensive dredging and coastal engineering programs beginning in the mid-1800s. Early nineteenth-century reports on tidal river training, which consisted mainly of channel deepening and shoreline armoring, reveal an emphasis on navigational hazards with little or no insight into the response of tides to anthropogenic intervention (Brooks, 1841). For tidal hydraulics in rivers, analytical frameworks based on the momentum and continuity equations constrained by channel geometry were introduced in subsequent studies, highlighting the role of convergence, friction, and intertidal storage on barotropic tidal propagation (LeBlond, 1978; Aubrey & Speer, 1985; Speer & Aubrey, 1985; Lanzoni & Seminara, 1998). Central to these studies is the notion that friction and nonlinear effects in shallow water are key in the landward transformation of the offshore tide. Friedrichs and Madsen (1992) also emphasized the importance of friction and found that tidal dynamics in many shallow embayments can be described with a zero-inertia equation wherein friction balances the pressure gradient force. Under that balance, the tidal elevation is governed by a diffusion equation in which the diffusion coefficient encapsulates friction and the nonlinearities induced by time-varying width and depth.

Although the introduction of analytical frameworks was not specifically motivated by the need to understand human interventions in estuaries, channel deepening can be effectively represented in scaled momentum and continuity equations as a change in depth or friction. A major advantage of this approach is that it can help elucidate the role of morphology on tidal flows at a relatively low computational cost. Previous studies have employed simplified scaled equations to examine the impact of dredging on tides, for

example in the Ems river (Chernetsky et al., 2010), Modaomen estuary (Cai et al., 2012a), Newark Bay (Chant et al., 2018) and in several estuaries including the Hudson River and Bristol Channel (Cai et al., 2012b). Although analytical frameworks are extensively used, caution must be taken in estuaries where localized nonlinear effects are difficult to represent mathematically. On the other hand, the implementation of simple and computationally expensive numerical models to assess the tidal response to dredging and other anthropogenic alterations involves additional challenges related to the retrieval and digitization of long-term records of currents or water level, which are necessary to assess model performance. Research on this topic can also be hampered when historical bathymetric charts are unavailable, or when the available ones do not have the resolution, areal coverage, or vertical datum consistency to allow a reasonable comparison of scenarios before and after dredging.

Recent efforts have been made to recover lost-and-forgotten water level measurements along the United States coastlines (Talke & Jay, 2017). Quality-checked historical spatial data and time series can be used to help determine the impact of dredging not only on tidal flows but on storm surges (Familkhalili & Talke, 2016), to evaluate storm tide trends (Talke et al., 2014) and to improve statistical predictions for future extreme events (Orton et al., 2018). Bathymetric reconstruction and long-term time series have informed the assessment of dredging on tides and river-tide interaction in a number of estuaries. For example, in the Hudson River estuary, United States, channel deepening led to a doubling of the tidal range near the tidal limit, generated asymmetries in high and low water, and reduced the risk for flooding due to an increase in the conveyance of river discharge (Ralston et al., 2019). In the Ems River estuary, Netherlands, dredging programs between 1980 and 2005

led to amplified tidal elevation along the channel. Even though the effect of dredging on tides has been studied in recent years, little is known about the effects of increased channel conveyance on tides in strongly convergent systems. There are also knowledge gaps on the effect of dredging on tidal energy fluxes imposed by shifts in elevation and velocity phase, which are important parameters for inundation dynamics (Holleman & Stacey, 2014). The expected increase in ship traffic at major ports of the world coincides with a period of rising sea levels, therefore exploring the trajectories of coupled human-estuarine dynamics becomes critical for sustainability. In this study, we focus on the effects of historical dredging on momentum-continuity dynamics and tidal energy fluxes in a strongly convergent system. In the following sections we present a brief overview of the mechanisms that control barotropic tidal propagation in estuaries and indicate how channel deepening can alter those dynamics.

3.2.1 Tidal amplification, damping, and distortion

Upon entering semi-enclosed basins and rivers, tidal waves can be dampened or amplified due to the competition between friction and convergence (Friedrichs & Aubrey, 1994). A landward increase in tidal range is observed in hypersynchronous systems where the amplifying effect of convergence outcompetes the damping effect of friction. The opposite is true in hyposynchronous estuaries where friction is more important than convergence, which causes the tidal range to decrease. In cases where friction and convergence have nearly equal and opposite effects, the tidal range remains nearly constant along the channel and the conditions are synchronous (de Miranda et al., 2017), or 'ideal' (Cai et al., 2012b). Anthropogenic channel deepening can fundamentally alter the relationship between friction and convergence by reducing hydraulic drag in the thalweg,

and the net effect is to amplify the tidal elevation and current speed. The reduced drag and greater depth also tend to increase the propagation speed of the tidal wave, leading to shifts in the timing of high and low water along the channel.

Although the linkage between increased depth and reduced friction conceptually explains the main impact of dredging on tides, additional feedbacks exist in systems where differences in intertidal storage and wetted width are significant between ebb and flood. The role of width (w) and depth (h) on barotropic dynamics can be examined through the tidal phase speed c, which in shallow, funnel-shaped estuaries is proportional to the ratio h/w (Friedrichs, 2010). In estuaries with negligible intertidal storage, w remains nearly unchanged over tidal cycles and c is only controlled by changes in h. The rising tide is faster than the falling in that scenario, the flood duration is shorter than the ebb, and the system is flood-dominant. If w is much larger at high tide that at low tide due to the presence of intertidal flats or storage areas, the falling tide is faster than the rising, the ebb duration is shorter than the flood, and ebb-dominant conditions are observed. The tidal asymmetry factor (γ), which arises from a Taylor series expansion of c, can be used to quantify the magnitude of the duration asymmetry (see e.g. Friedrichs (2010) and Nidzieko (2010):

$$\gamma = \frac{a}{\langle h \rangle} - \frac{1}{2}\frac{\Delta w}{\langle w \rangle} \tag{3.1}$$

where a is the elevation amplitude and the brackets denote a tidal average. Flood-dominant conditions are observed when $\gamma > 0$, and ebb dominance when $\gamma < 0$. Equation 3.1 offers some conceptual insight into the trajectories of tidal systems to anthropogenic intervention. For example, shoreline hardening or softening (e.g. groin installation or

marsh restoration) may change tidal dynamics through their potential impact on intertidal storage ($\Delta w/w$), while dredging tends to reduce flood dominance through an increase in $\langle h \rangle$. However, since dredging can also lead to increased amplitude through a reduction of drag, the impact of deepening on tidal asymmetries cannot be inferred from deepening alone. The relationship between dredging and tidal asymmetries can be further complicated by gradual changes in bed drag due to the generation of sand waves, for example as observed in the Seto Sea, Japan (Knaapen & Hulscher, 2002).

3.2.2 Tidal energy flux

As discussed previously, the offshore tide can undergo frictional distortion upon entering estuaries and tidal rivers, with depth as one of the main controlling variables. Tidal flow over rough topographic features such as channels and shallow ridges can lead to hotspots in energy dissipation (Kang & Fringer, 2012) which can alter the transmission of energy upstream. While tidal elevation amplitude in estuaries depends on friction and convergence, the analysis of tidal energy fluxes can offer complementary information on how tides adjust to a deeper channel. For example, a direct comparison of friction and convergence via scaling analyses does not offer insight into how the cross-channel structure of depth-averaged currents, elevation, and phase determine the amount of energy that is transferred upstream or locally dissipated into heat. From fundamental fluid dynamics (Cummins & Oey, 1997; Holleman & Stacey, 2014), it can be shown that tidal energy fluxes are given by $\rho g h \langle \bar{u} \eta \rangle$, where ρ is the water density, g is the gravitational acceleration, η is the time varying water level, $\bar{u}$ the depth-averaged current speed, and the brackets denote a time average over tidal cycles. The phase lag between $\bar{u}$ and η is critical for the magnitude of the flux since the product $\langle \bar{u} \eta \rangle$ is zero when velocity and elevation are in quadrature. In

estuaries, shoreline configuration, bathymetry and freshwater discharges can alter the phase lag between current speed and elevation (Friedrichs, 2010), and thus affect the energy flux distribution. Although reports on energy fluxes in estuaries are not new (Stacey & Valle-Levinson, 2006; Zhong & Li, 2006; MacCready et al., 2009), little is known about the effect of dredging on energy transmission and dissipation. Recent studies on tidal energetics in estuaries have been carried out in the context of inundation and sea level rise, for example in San Francisco Bay (Holleman & Stacey, 2014) and in the bays of Chesapeake and Delaware (Lee et al., 2017). In those investigations, current and projected depth and shoreline distributions are employed by numerical models to assess the response of tides to a range of sea level rise scenarios. In their models, anthropogenic inputs are mainly represented as new intertidal areas, some of them product of extensive marsh restoration, or as channelization in the form of 'shoreline hardening'. The analysis in our study is retrospective rather than prospective and can offer another vantage point from which to assess the trajectories of estuaries to anthropogenic basin alterations.

3.2.3 Study goals

The main goal of this study is to explore how long-term anthropogenic channel deepening can affect barotropic tidal dynamics in strongly convergent estuaries. The example here is the Delaware Estuary, whose morphology encapsulates a range of features that make it generalizable to other systems such as a wide and funnel-shaped bay and an unstratified tidal river. The approach here incorporates historical bathymetric reconstruction, analytical models, and the application of a 3D numerical model. We specifically aim to i) assess the effect of channel deepening on tidal amplification, damping, and distortion via analysis of the continuity and momentum equations, and ii) examine

how deepening can change tidal phase and energy fluxes in a highly altered estuary. Results herein complement existing studies that have explored how dredging has altered river-tide interactions, storm surge propagation, and estuarine turbidity maximum dynamics in other systems (Liria et al., 2009; Chernetsky et al., 2010; Familkhalili & Talke, 2016; Devlin et al., 2017; Ralston et al., 2019). This paper is organized as follows: section 3.2 describes the study region and provides context for channel deepening; section 3.3 outlines the methods and describes the numerical model, section 3.4 presents model results and the discussion, and section 3.5 the conclusions.

3.3 Methods and hydrodynamic model

We conducted a series of numerical experiments with realistic bathymetry and idealized tidal and freshwater forcing to analyze the effect of dredging on tidal hydraulics. Historical and modern bathymetric data was interpolated onto a high-resolution curvilinear grid of the bay (1276 x 184 nodes, 20 vertical levels), for the Regional Ocean Modeling System, ROMS (Haidvogel et al., 2008). ROMS solves the Reynolds-Averaged Navier-Stokes equations as described by Shchepetkin and McWilliams (2005). Grid stretching allowed reasonable spacing in the lower bay (400 m) and a high coastline and bathymetric resolution in the landward sections of the system (6 m). Smoothing of bathymetry (Shapiro, 1970) was performed to avoid numerical instabilities in the computation. Boundary conditions for salinity and elevation were obtained from the Mid-Atlantic Ocean Climatological and Hydrographic Atlas (MOCHA, Levin et al. (2018)), and were prescribed at the open oceanic boundaries. The bottom friction scheme consists of logarithmic drag law with a uniform bottom roughness length of 1 mm. The model is forced with tidal

constituents from the ADCIRC database (Luettich et al., 1992). Surface wind data was obtained from the Philadelphia Airport Station, and river discharge for the Delaware River was prescribed at the head of the tides with US Geological Survey data at Trenton (station #01463500). The period for the model assessment was September 2014 in which a relatively low river discharge in the Delaware river (~100 m^3/s) was recorded. The choice for this time period is also consistent with the last time the modern grid was updated with USACE and NOAA depth soundings. Comparison of modeled results and observations of tidal elevation at gauges maintained by NOAA along the estuary (figure 3.1) reveal reasonable predictive model skill.

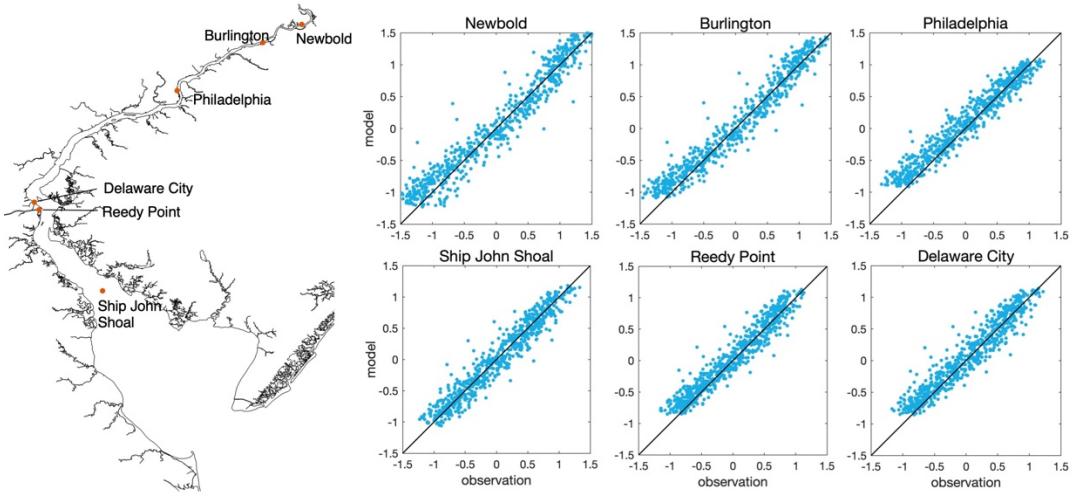

Figure 3.1 Comparison of modeled and observed tidal elevation at six locations in the Delaware estuary (meters). Station locations are shown on the map. The solid black line on the panels has slope equal to 1.

Since there is no spatial coverage of tidal elevation in 1848 in the estuary as a whole, no model skill assessment was carried out for the historical scenario. Once we obtained reasonable model skill for the modern case, we used the same model setup to explore historical conditions. An assumption of this approach is that changes in thalweg depth and

channel width are more important for barotropic dynamics than other shifts, for example in the spatiotemporal variability of bottom roughness. Following the model assessment, we ran simulations with idealized tidal forcing (Luettich et al., 1992) and constant river discharge for the annual mean (350 m^3/s) and typical freshet conditions (2000 m^3/s). Simulations were performed for both the historical and modern scenarios. Tidally varying variables were extracted from model results through least squares fitting to the trigonometric function:

$$X = A \sin \omega t + B \cos \omega t = X_0 \cos(\omega t + \phi) \tag{3.2}$$

where X is the variable for the tidal constituent (e.g. elevation or current speed), A and B are constants, ϕ is the phase lag and $X_0 = \sqrt{A^2 + B^2}$ is the amplitude. Model output was also employed to interpret momentum and continuity dynamics via analytical frameworks (Friedrichs & Aubrey, 1994; Friedrichs, 2010).

3.4 Results and discussion

In this section we analyze the tidal response of the bay to anthropogenic alterations based on numerical model output. Since the system is dominated by semidiurnal (M2) variations (Parker, 1984; Aristizabal & Chant, 2013), we only consider that constituent in the analysis. We report historical changes in tidal elevation amplitude, currents, and phase, followed by a discussion on how these shifts had an impact on energy fluxes. A scaling analysis is also performed to discuss the impact of anthropogenic alterations on momentum dynamics.

3.4.1 Channel deepening, tidal elevation amplitude, and asymmetries

Model results indicate that channel deepening significantly modified the time-varying elevation and current response along the system, especially in the tidal river. Shifts in tidal amplitude and travel time for the M2 tidal wave are shown in figure 3.4. Regarding tidal amplitude (figure 3.4a), both historical and modern scenarios exhibit an alternation of landward amplification, damping, and amplification, consistent with relatively modern observations in the Delaware (Parker, 1984; Walters, 1997). However, shallower depths in the 1800s favored enhanced attenuation along the upper estuary and tidal river. The increased conveyance caused by dredging led to increments in tidal amplitude by factors of 1.06 in the lower estuary (0-60 km), 1.27 in the upper estuary and tidal river (60-150 km), and 2.3 at the head of the tides (km > 180). These shifts are in close agreement with DiLorenzo et al. (1993), who used a simplified model to evaluate the impact of the most recent deepening from 40 ft to 45 ft (12.2 m to 13.7m) on M2 tidal elevation. The doubling in tidal range in the Delaware Estuary is similar to that observed in the upper Hudson River Estuary at Albany, New York (Ralston et al., 2019). A more modest response was reported for the Ems estuary (factor 1.4) after dredging programs between 1980 and 2005 (Chernetsky et al., 2010). Although dredging led to bigger tides in the Hudson, Ems, and Delaware, the response in the Delaware did not involve a shift from hyposynchronous to hypersynchronous conditions under mean river discharge. Instead, the tidal range increases in both scenarios landward from kilometer 150, but with significantly more damping in the historical case. A comparable response was reported in Tampa Bay where pre-dredging hypersynchronous conditions became more hypersynchronous after channel deepening (Zhu et al., 2015).

The travel time of the M2 high water (HW) also changed after channel deepening but mostly in the upper estuary and tidal river (figure 3.4c). The landward increase in arrival time is indicative of a wave that propagates up-estuary, and the inverse slope of the curve is the phase speed, c_m. HW takes about 5.5 hours to propagate from the mouth to 150 km upstream (c_m~7.6 m/s) in both scenarios. This phase speed remains nearly constant in the modern case until the landward limit. In the pre-dredging scenario, c_m drops by about 80% to 1.5 m/s from kilometer 150 to 160. This segment of the tidal river is near Philadelphia, an area of a highly localized width constriction and two river bends. We will show in later sections that this sharp reduction in phase speed is because of elevated friction through the constriction. From kilometer 160 to the head of tides, the arrival time in 1848 is nearly uniform, therefore HW occurs at about the same time and the wave appears standing. Spatially uniform arrival times were also observed in the upstream segment of the Guadalquivir river, Spain, where a dam in favors standing tidal conditions (Díez-Minguito et al., 2012).

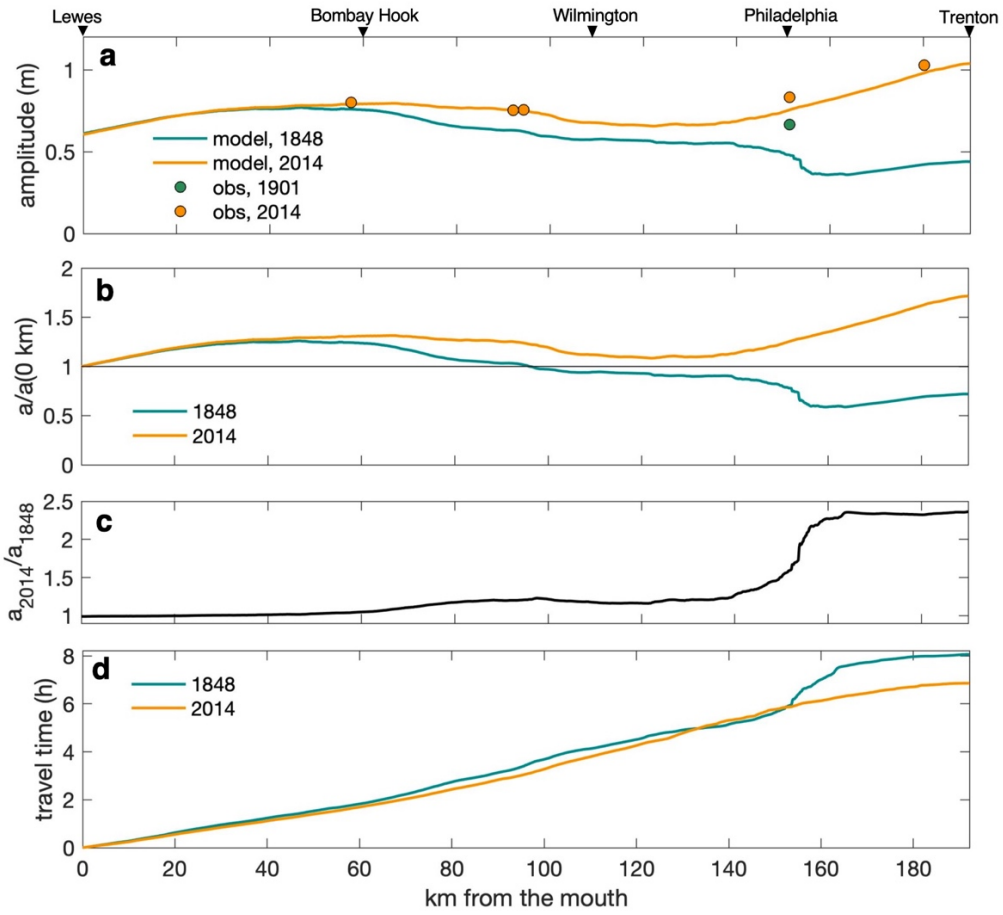

Figure 3.2 (a) Modeled M2 elevation amplitude along the channel. Amplitudes in 1901 and 2014 are plotted for reference based on harmonic analysis of NOAA data (stations 8545530 and 8545240), (b) ratio between modern and historical amplitude (a_{2014}/a_{1848}), and (c) travel time of high water in hours. The location of Lewes, Bombay Hook (BH), Wilmington, Philadelphia, and Trenton (head of the tides) are also shown.

Since the main response in amplitude took place in the tidal river, we now consider the response under high (e.g. freshet) river discharge ($Q_r = 2000$ m^3/s) at the head of tides (figure 3.3). The six-fold increase in Q_r from the mean led to nearly synchronous conditions over a 20 km segment seaward from the head of the tides in both 1848 and 2014. This local adjustment from landward amplification to equilibrium with convergence corresponds to a reduction in amplitude of 33% in 1848 and 19% in 2014. For each of these cases, width convergence remained nearly the same and thus the drop in amplitude

along the tidal river is due to increased friction. Tidal damping under fluvial-tidal interactions has been studied previously, for example by examining the role of the river velocity and alternating tidal velocities on the vertical stress divergence term in the momentum equation (Godin, 1985). The sensitivity of tidal amplitude to increasing river discharge in our modern model is consistent with observations made in 1979 and presented by Parker (1991) prior to the most recent deepening from 40 ft to 45 ft. In Parker's study, a nine-fold increase in Q_r at Trenton (130 m^3/s to 1156 m^3/s) reduced M2 elevation amplitude by 25%. Dredging alters the sensitivity of tidal amplitude to river discharge in that the increased conveyance reduces river velocity and therefore its frictional effect. The latter is consistent with the stronger modulation of amplitude by river discharge in the 1848 scenario. Besides amplitude modulation, the river slope is also affected by channel deepening. The mean momentum balance near the head of tides is approximately between the pressure gradient force caused by the river slope and friction. Following Godin (1985), this balance can be written as:

$$-g\frac{\partial \eta_0}{\partial x} = C_D \frac{u_0^2}{h+\eta_0} \tag{3.3}$$

where η_0 is the residual water elevation, $\partial\eta_0/\partial x$ is the river slope, g is the gravitational acceleration, C_D is the drag coefficient, u_0 is the river velocity, and h is depth. The river slope near Trenton is nearly the same in both 1848 and 2014 under median river discharge (figure 3.5b). Based on equation 3.3, an unchanged slope suggests that, for the median river discharge, the impact of dredging on η_0 and $C_D u_0^2$ is such that $C_D u_0^2/(h+\eta_0)$ remained nearly constant in both 1848 and 2014. Under higher river discharge, $\partial\eta_0/\partial x$ was noticeably steeper (factor of 4) in 1848 but only in the segment from 150 to 160 km from

the mouth, which coincides with the location where the phase speed and tidal amplitude also drop.

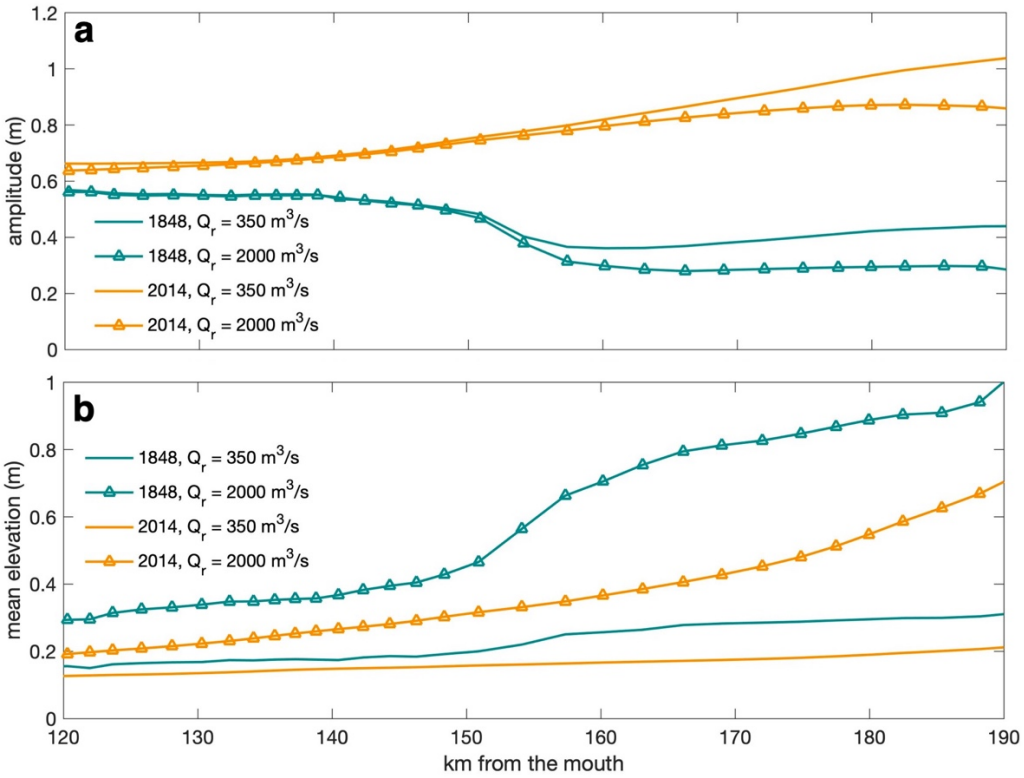

Figure 3.3 Effect of river discharge (Q_r) at the head of the tides near Trenton on (a) M2 tidal elevation amplitude and (b) mean elevation.

Model results of tidal amplitude under mean and high river discharge can be used to assess the role of channel deepening on tidal distortion and asymmetries following equation 3.1. Intertidal effects on barotropic tidal dynamics are negligible here ($\Delta w/w \sim 0$) and thus the conditions are flood dominant ($\gamma \approx a/h > 0$) and historical shifts are more pronounced in the upper tidal river. Estimates of the asymmetry factor near the head of tides are shown in table 3.1. In 1848 and 2014, γ decreased by 33% and 25% under higher river discharge compared with mean discharge, consistent with increased river velocities

introducing ebb dominance to the system. Note that the effect of Q_r on γ is more pronounced in 1848 than in 2014 because the smaller channel conveyance in the pre-dredge scenario leads to a stronger river velocity.

Asymmetry factor (scenario)	$Q_r = 350$ m^3/s	$Q_r = 2000$ m^3/s	% change
γ (1848)	0.06	0.04	-33%
γ (2014)	0.08	0.06	-25%

Table 3.1 Effect of channel deepening and river discharge on tidal asymmetries in the tidal river near Trenton.

3.4.2 Channel deepening and tidal currents

While significant shifts in elevation amplitude took place mostly between Philadelphia and Trenton, the response of tidal currents to deepening was noticeable in a longer segment from Bombay Hook to the head of tides. To analyze tidal current patterns, we obtained time series of M2 velocity at each grid point as $U\cos(\omega t + \phi_u)$, where U is the current amplitude and ϕ_u is the current phase. Unlike tidal elevation amplitude, the spatial distribution of U is quite sensitive to the lateral bathymetric distribution, therefore we show the velocity amplitude on shoals (U_{sho}) (e.g the minimum in the cross-section) and in the thalweg (U_{tha}) in figure 3.4. Historical shifts in U_{tha} are negligible in the lower estuary from the mouth to Bombay Hook (km 60), but differences become increasingly noticeable upstream. Near Bombay Hook, U_{tha} is roughly 1 m/s for both scenarios. In 1848, tidal velocity drops to 0.5 m/s and then to a local minimum (~0.3 m/s) at km 130 before Philadelphia. The current amplitude then increases locally through Philadelphia (km 140-150) by a factor of 4.3 (1 m/s). In 2014, U_{tha} is about 1 m/s from kilometers 60 to 120, but with localized departures in the order of 0.25 m/s introduced by the bathymetric

variability of the dredged channel. In the upper tidal river, U_{tha} drops in both scenarios from about 1 m/s to 0.2 m/s albeit more rapidly in 1848, possibly due to enhanced friction in a shallower channel. In contrast to the changes in U_{tha}, the current amplitude on shoals (U_{sho}) remained comparatively small along the estuary (0 – 0.2 m/s).

The noticeable channel-shoal differences in U motivate a brief examination of the phasing of currents, ϕ_u. As with U, we show the along-channel distribution of ϕ_u in the thalweg (tha) and on shoals (sho, figure 3.5). Values of ϕ_u are 45° to 90° greater over shoals than in the channel, which indicates that currents change sooner over shallow regions than in the thalweg. In the thalweg, a landward decrease in phase describes the progression of peak M2 currents up the estuary. Historical shifts in ϕ_u are significant landward from km 120 where differences increase from 5° to about 50° near the tidal limit. For the M2, this shift corresponds to a time difference in the arrival of peak currents of about 1.5 h in the upper tidal river.

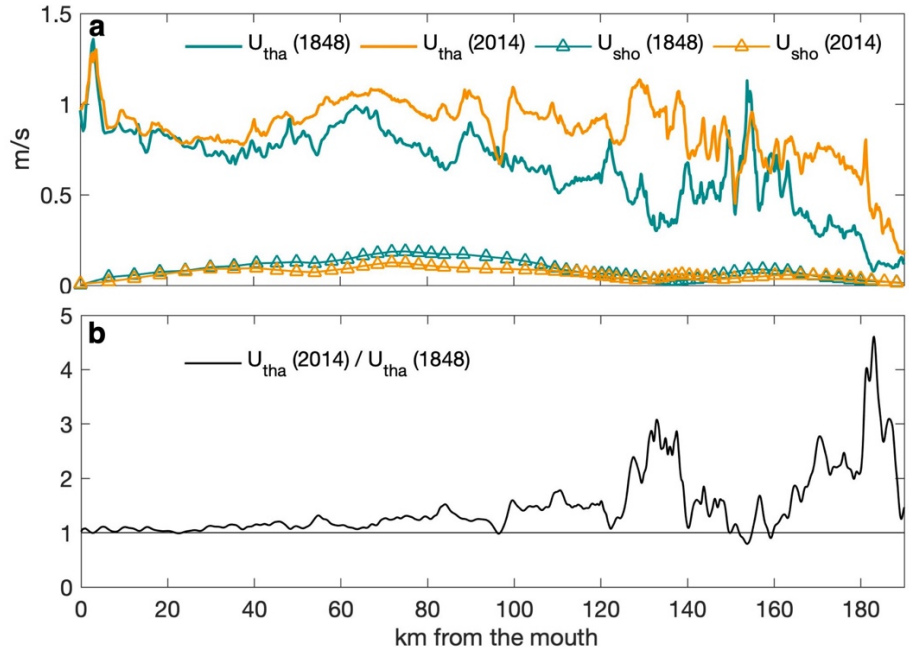

Figure 3.4 (a) Modeled along-channel tidal current amplitude in the thalweg (solid lines) and shoals (triangles) for both modeled scenarios. (b) Tidal current amplitude ratio between modeled scenarios (thalweg).

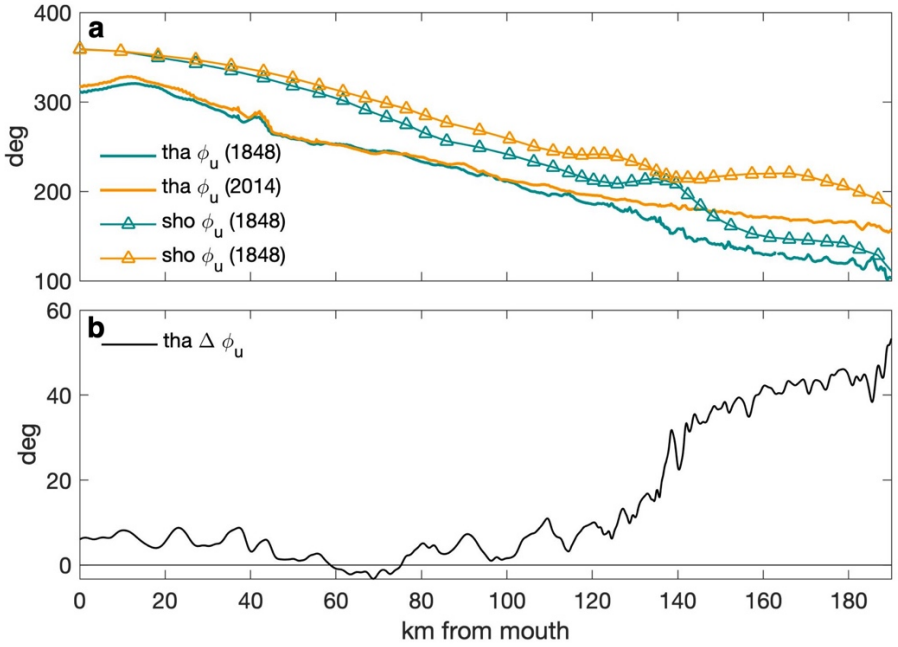

Figure 3.5 Modeled along-channel tidal current phase in the thalweg (solid lines) and on shoals (triangles) (b) Difference in current phase between modeled scenarios (thalweg).

3.4.3 Analytical framework for tidal elevation

Following an examination on how dredging changes tidal elevation and currents in the Delaware, we analyze the barotropic momentum equation to quantify the role of channel deepening on the competition between convergence and friction under mean river discharge. Although there are a number of suitable analytical approaches (Lanzoni & Seminara, 1998; Savenije et al., 2008; Cai et al., 2012b) here we consider the scaled momentum equation for convergent, near-equilibrium estuaries (Friedrichs, 2010). First, we characterize convergence by fitting the along-channel width (w) variation to exponential functions that take the form

$$w(x) = w_0 \exp\left(-\frac{x}{L_w}\right) \tag{3.4}$$

where x is the along-channel coordinate (positive upstream) and w_0 is the width at $x = 0$. The metric for convergence here is L_w, which tends to zero in strongly convergent systems and to infinity in channels with constant width. The metric for landward amplification or damping can be obtained from exponential fits to elevation amplitude along segments of the estuary, $a(x)$:

$$a(x) = a_0 \exp\left(\frac{x}{L_a}\right) \tag{3.5}$$

where a_0 is the amplitude at $x = 0$ and the e-folding length scale L_a indicates landward damping ($L_a < 0$) or amplification ($L_a > 0$). The hydraulic drag r, which represents friction, can be expressed as:

$$r = \frac{8C_D}{3\pi}\frac{U}{h} \tag{3.6}$$

$C_D = 3 \cdot 10^{-3}$ is the quadratic drag coefficient and the $8/3\pi$ factor arises from the Fourier series expansion of the bottom friction term in the momentum equation. Recalling that ω is the M2 tidal frequency, Friedrichs (2010) shows that:

$$\frac{L_a^{-1}}{k} = \frac{(kL_w)^{-1} - (r/\omega)}{2 + (r/\omega)(kL_w)^{-1}} \tag{3.7}$$

The numerator on the right-hand side of (3.7) quantifies the effect of convergence $(kL_w)^{-1}$ and friction (r/ω) on the sign and magnitude of L_a^{-1}. Substituting $\omega/k = c$ in (3.7), it can be shown that tidal amplitude increases upstream ($L_a^{-1} > 0$) when $c/r > L_w$ and decreases ($L_a^{-1} < 0$) when $c/r < L_w$. The phase speed can be estimated as $c = \sqrt{gh}$, and the ratio c/r is a function of depth to the 3/2 power divided by the tidal current amplitude,

$$\frac{c}{r} = \left(\frac{3\pi\sqrt{g}}{8C_D}\right)\frac{h^{\frac{3}{2}}}{U} \tag{3.8}$$

In the Delaware Estuary, historical changes in L_w are modest compared to shifts in c/r induced by dredging. In the strongly convergent bay from the mouth to Bombay Hook (km 80), $L_w = 60$ km, and roughly 75 km in the tidal river between Bombay Hook and Trenton. Through Philadelphia (km 140-260) where a highly localized attenuation of tidal

amplitude was modeled in 1848, c/r changed from 43 km (< 75 km) to 105 km (>75 km) in 2014, consistent with a shift from hyposynchronous to hypersynchronous conditions, and with a change from damping to amplification. Near the head of the tides, $c/r = 76$ km in the historical case, only slightly larger than the convergence length scale in agreement with slightly hyposynchronous conditions, and consistent with the relatively constant tidal amplitude in this reach. In contrast, $c/r = 105$ km in the modern estuary, indicative of significant landward amplification. Similar conclusions can be obtained by investigating the solution of the following linearized momentum equation for barotropic flows with friction:

$$\frac{\partial \bar{u}}{\partial t} = -g\frac{\partial \eta}{\partial x} + C_D\frac{u_b|u_b|}{h} \tag{3.9}$$

where $\bar{u}$ and u_b are the depth-averaged and near-bed velocities, and x is the landward coordinate. Constrained by continuity and through an expansion of u_b in a cosine Fourier series, an analytical solution for η is (Friedrichs & Aubrey, 1994):

$$\eta(x,t) = a_0 e^{\mu k x}\cos(kx - \omega t) \tag{3.10}$$

μ is a constant factor to account for landward attenuation of the tidal amplitude. In convergent systems, the effective μ depends on the competition between convergence and friction, and thus $\mu < 0$ would indicate that friction dominates over convergence. Friedrichs and Aubrey (1994) use observations of tidal amplitude along a number of convergent estuaries to estimate this factor simply as $\mu = (kL_a)^{-1}$. We find that the strong frictional

attenuation of tidal amplitude near Philadelphia in 1848 corresponds to $\mu = -1.4$ while the observed amplification in 2014 is described by $\mu = 0.4$.

3.4.4 Elevation-velocity phase and energy fluxes

In this section we use gridded bathymetric data and the modeled response in amplitude and phase to explore the impact of dredging on tidal energy fluxes in the estuary. As mentioned earlier, the along-channel energy flux at each point is $\rho g h \langle \bar{u}\eta \rangle$. We calculate the cross-sectionally integrated energy fluxes (F) as a function of distance from the mouth (x -coordinate) as:

$$F(x) = \rho g h \int_0^{w(x)} \langle u\eta \rangle dl \tag{3.11}$$

where dl is a differential of width, $\bar{u}, \eta$ are the time-varying depth-averaged current speed and elevation, and $w(x)$ is the width at each along-thalweg point. Although dredging tends to amplify u and η, it is $\phi_{u\eta}$, the phase lag between elevation and currents, what ultimately determines the magnitude of F. Following the parlance of Holleman and Stacey (2014), F is maximized in progressive conditions ($\phi_{u\eta} = 0°$) and zero in standing conditions when velocity and elevation are in quadrature ($\phi_{u\eta} = 90°$). Model results of elevation-velocity phase lag are shown in figure 3.6. Common to the historical and modeled scenarios is a channel-shoal asymmetry in $\phi_{u\eta}$ in most of the lower bay where velocity leads elevation by nearly 90° over shoals and ~45° in the deep channel, which indicates that most of the tidal energy is conveyed in the deeper, more progressive channel. Mid-estuary between Bombay Hook and Wilmington (60-110 km) velocity leads elevation in the channel by about 40° in

1848 and by 30° in 2014, consistent with a shift into more progressive dynamics after dredging. A localized minimum ($\phi_{u\eta}$~25°) was observed near Philadelphia (km 150) in the historical scenario, possibly due to friction bringing channel velocity and elevation closer to phase. Landward from Philadelphia, $\phi_{u\eta}$ increases rapidly from 25° to ~80° in the channel and close to 90° over shoals. In the modern channel, $\phi_{u\eta}$ also increases from 30° to about 80° but over a longer segment from Wilmington to Trenton and without undergoing a sharp reduction at lateral constrictions near Philadelphia.

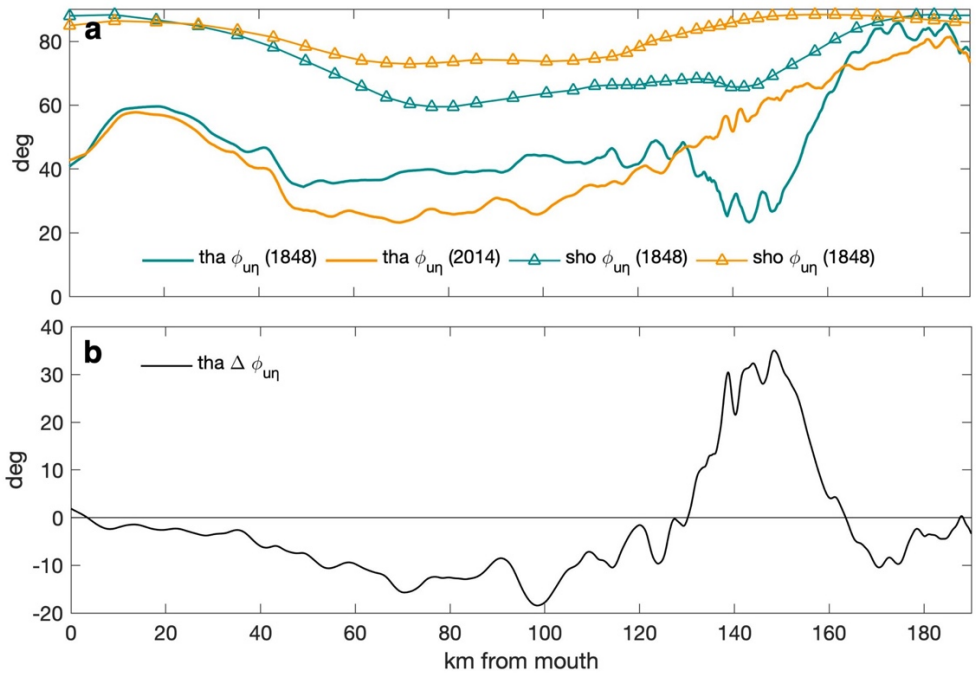

Figure 3.6 (a) Along-estuary phase lag between velocity and elevation in the thalweg (solid lines) and over shoals (triangles) for both modeled scenarios. (b) Departure in the elevation-velocity phase lag after channel deepening (thalweg).

The fully integrated picture on the impact of dredging on energy fluxes is shown in figure 3.7 where we show the variation of F as a function of distance from the mouth as well as the rate of change of flux along the estuary ($\partial F/\partial x$, positive values indicate energy

dissipation). The flux at the mouth is ~350 MW, in close agreement with a study on sea level rise and tidal energy fluxes in the Delaware (Lee et al., 2017). In the lower and upper estuary, the flux magnitude in 2014 is roughly 20 MW greater than in 1848 (km 50-100), consistent with a historical shift towards bigger amplitudes, swifter currents, and more progressive dynamics in the channel. Interestingly, the increment in flux due to dredging is similar to projected changes in energy flux under 1 m of sea level rise and shoreline hardening in Delaware Bay (Lee et al., 2017). In other words, the response of the flux in the Delaware due to the doubling of shipping channel depth is similar to the projected shift in flux in a scenario under 1 meter of sea level rise with no intertidal storage.

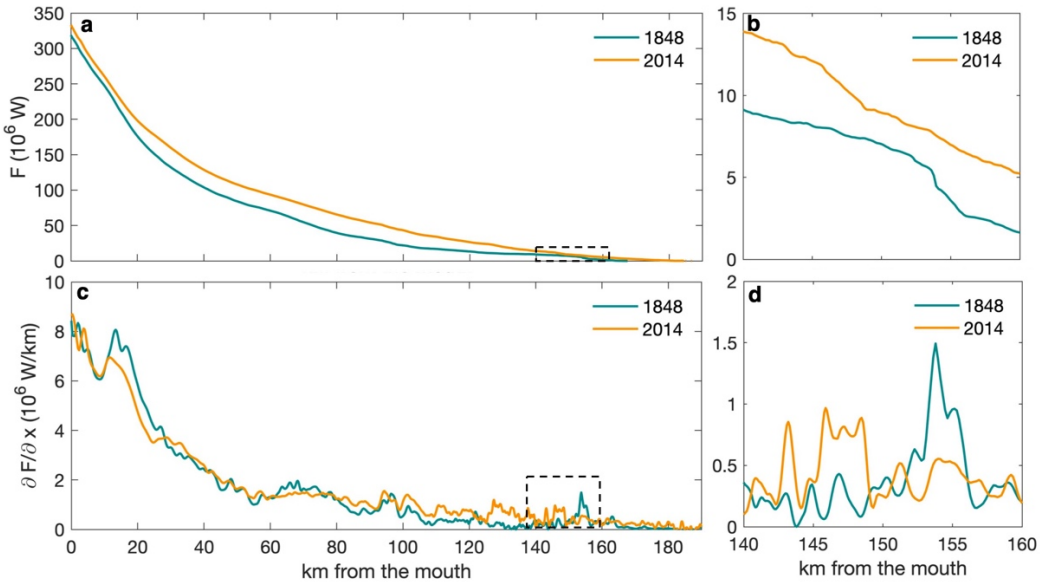

Figure 3.7 (a) Cross-section integrated tidal energy flux as a function of distance from the mouth. (b) Close-up of fluxes between kilometers 140 and 160 through Philadelphia. (c) rate of change of energy flux along the estuary, and (d) rate of change of flux in the same segment show in (b).

Since noticeable shifts in phase speed and tidal amplitude took place near Philadelphia, we take a close-up look into the 140-160 km segment (Figure 3.7b, d). Spatial patterns of

fluxes in that region are also shown in figure 3.8. The landward energy flux passing through km 140 was 8.2 MW in 1848 and 11.6 MW in 2014, and the increase between scenarios is a consequence of a less frictional and more progressive channel. At the end of the segment (km ~160), frictional dissipation causes the flux to drop by 90% in 1848 and by 65% in 2014 with respect to the flux that enters at 140 km. Consistent with the scaling analysis in the previous section, the localized reduction in tidal amplitude in 1848 through 140-160 km coincides with the largest value of $\partial F/\partial x$ in the tidal river. Tidal flows through the localized constriction near Philadelphia led to rates of $\partial F/\partial x$~1.5 MW/km in 1848 compared to 1.0 MW/km in 2014.

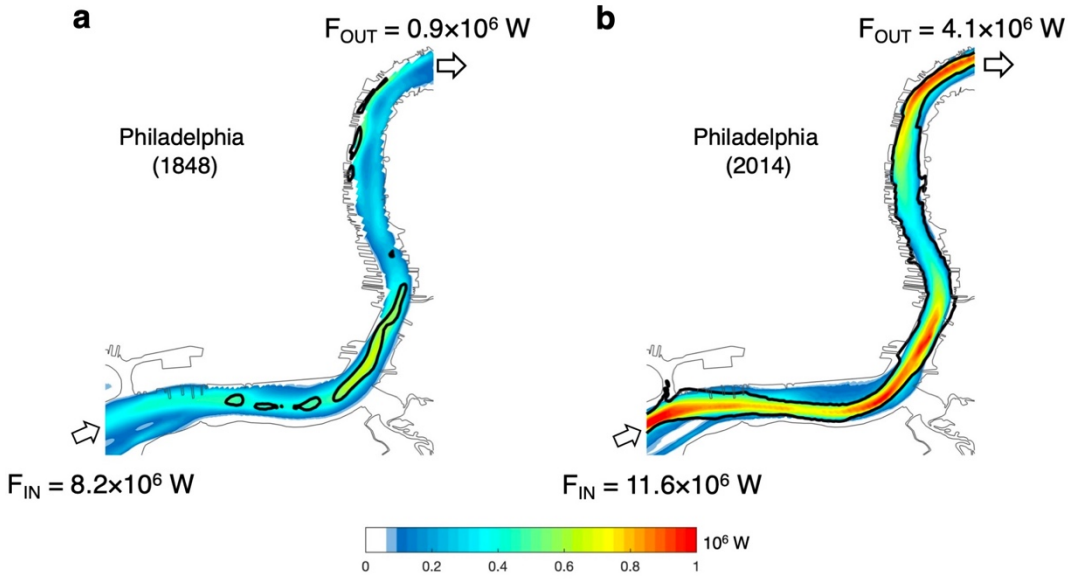

Figure 3.8 Spatial structure of the tidal energy flux in (a) 1848 and (b) 2014. Energy fluxes into and out of the river segments are also shown. The 10m isobath is drawn in both figures to highlight the role of channel deepening on energy flux transmission. Note significantly shallower conditions and reduced flux transmission in 1848.

3.5 Summary and conclusions

A numerical model with historical (1848) and modern (2014) bathymetry was implemented to study the impact of shipping-channel construction and maintenance dredging in convergent estuaries, using the Delaware Estuary as a case study area. In both cases, results indicate that tidal amplitude increases from the mouth in the lower estuary, decreases landward in most of the upper estuary, and then is amplified in the tidal river. The main effect of channel deepening was to reduce hydraulic drag, which increased tidal elevation amplitude in the modern estuary, especially near the tidal limit where the tidal range doubled. A one-dimensional analytical framework of barotropic dynamics was used in addition to the numerical model to explore changes in the competition between convergence and friction through scaling analyses. The analytical model demonstrated that convergence outcompetes friction in both the historical and modern scenarios in the upper reaches of the estuary, in contrast to other estuaries in which dredging led to shifts from landward damping to amplification. However, frictional effects were more important in the historical Delaware Estuary as evidenced by the modest amplification of tidal range near the head of the tides. Changes in the arrival time of high water are increasingly important in the upstream direction, with the biggest adjustment observed near Philadelphia where friction significantly reduced phase speed in 1848. Examination of the elevation-current phase structure reveals that increased channel conveyance led to more progressive dynamics in the shipping channel, and correspondingly greater tidal energy flux. Along with faster currents and larger tidal ranges in the modern estuary, an important consequence of dredging is an increase in upstream energy flux by about 20 MW. This

historical shift in energy flux is similar to the projected change in flux in modeled scenarios under 1 meter of sea level rise and shoreline hardening (Lee et al., 2017).

Chapter 4 - Changes to Suspended Sediment Concentration and Trapping in the Delaware Estuary Associated with Dredging

4.1 Abstract

We present a modeling study on the impact of historical channel deepening on suspended sediment concentration, erosion and deposition patterns, and fluxes in the Delaware Estuary. In both 1848 and 2014, turbidity maxima developed along the estuary mainly at lateral bathymetric transitions from shoals to channels instead of only in the thalweg. The location of sediment deposition areas shifted landward after channel deepening due to the migration of the salt intrusion, with potential implications on shifts in sediment supply to subtidal flanks and wetlands. The mean advection of sediment was landward in the channels and seaward over shoals in the saline estuary, and the opposite in the tidal river in both scenarios. Flood dominance due to tidal distortion led to landward sediment pumping in both 1848 and 2014, with bigger fluxes in the modern case due to increased bed stresses and higher suspended sediment concentration.

4.2 Background

Urbanized estuaries of the world are under constant anthropogenic pressure due to the demand of services such as recreation and transportation. The need for navigation through tidal rivers, inlets, and harbors in coastal cities has been reported since the late 1800s and has increased along with urbanization, economic development, and population growth (Wheeler, 1893; Boerema & Meire, 2017). While the services provided by navigational channels are evident, relatively little is known about the adjustment of sediment fluxes and

trapping to anthropogenic basin modifications. Sediment dynamics are closely linked to hydrodynamic processes, which increased channel depth can alter by causing shifts in tidal currents, salt intrusion, stratification, and storm surge conveyance (Chernetsky et al., 2010; Friedrichs, 2010; Familkhalili & Talke, 2016; Ralston et al., 2019). Historical bathymetric charts and long-term in-situ observations have been used to assess the impact of channel deepening on tidal currents, mean river slope, storm surge propagation, and salt dynamics in urbanized estuaries such as Cape Fear River, Newark Bay, and Hudson River (Familkhalili & Talke, 2016; Chant et al., 2018; Ralston & Geyer, 2019; Ralston et al., 2019). In comparison, the response of sediment transport to dredging remains scarcely studied. Sediment fluxes regulate estuarine basin morphology, pollutant trapping, and wetland sustainability (Dyer, 1995; Ganju et al., 2005; Horowitz et al., 2014), and the role of humans in these dynamics has become increasingly relevant in the Anthropocene.

Notable exceptions in the research gap on dredging and sediment dynamics correspond to European estuaries such as the Ems in the Netherlands and the Gironde in France. In the Ems river, 4 to 10-fold increases in the mean suspended sediment concentration are attributed to channel deepening (de Jonge, 1983; de Jonge et al., 2014; van Maren et al., 2015). More recently, simplified 1D models were developed to assess the impact of dredging on mud and sand transport in prismatic and weakly convergent tidal channels, with the Rotterdam Waterway as an example (van Rijn & Grasmeijer, 2018; van Rijn et al., 2018). The authors found that a 10-20% depth increase of the already deep (> 15 m) waterway in Rotterdam would have a marginal effect on depth-integrated sand fluxes and deposition patterns. These models were intended to provide a computationally feasible option to determine how channel deepening would impact sediment transport patterns in

an engineering context, but their applicability may be limited in systems with significant bathymetric variability or strong shoreline convergence. In urbanized estuaries such as the Hudson and the Delaware, sediment fluxes and trapping are modulated by complex channel-shoal topography (Ralston et al., 2012; McSweeney et al., 2016a), which may not be accurately represented by 1D models. In the following sections we present a brief overview of sediment dynamics in estuaries as well as an overview of the main salt and sediment dynamics in the modern Delaware Bay based on previous studies.

4.2.1 Dredging and Sediment Dynamics in Estuaries

In estuaries, the transport and fate of sediment particles is modulated by riverine and marine supply, bed composition, and also by barotropic and baroclinic hydrodynamic processes that are constrained by morphology and bathymetry. One of the main characteristics of sediment dynamics in estuaries is the generation of Estuarine Turbidity Maxima (ETM), which some authors define as regions of localized maxima in suspended sediment concentration (SSC). Typically, ETMs can be found at the salt intrusion limit, in the freshwater zone (i.e. in the tidal river), and at specific topographic features of the basin (Burchard et al., 2018). The limit of salt intrusion is often associated with a region of axial flow convergence (i.e. a null point) which is hydrodynamically favorable for the consolidation of a bottom sediment pool. Steady theory (Monismith et al., 2002; Ralston et al., 2008) indicates that the salt intrusion length (L_x) is a function of cross-sectional area (A), channel depth (h) and river discharge (Q_r) as $L_x \propto A^{1/3} h^{5/3} Q^{-1/3}$. Since channel deepening is essentially an increase in A and h, it is expected that L_x will also increase and that the associated ETM will move landward. Beyond the salt intrusion limit, the development of ETMs in the fresh tidal river can be due to tidal asymmetries in velocity

caused by the frictional deformation of the offshore tide, see for example the case of the Gironde (Allen et al., 1980). Topographic features such as channel contractions, holes, straits, and localized lateral transitions in depth (axial or lateral) are often associated with gradients in bed stress, salinity, and stratification, which can ultimately lead to the formation of ETMs. See for example model results and observations in the Hudson estuary where topographic variability leads to the formation of multiple turbidity maxima at intermediate salinities rather than at a single location near the salt intrusion limit (Ralston et al., 2012).

Sediment fluxes, which govern the spatiotemporal variability of SSC in estuaries, depend on both tidally averaged (mean advection) and tidally varying (pumping) processes (Sommerfield & Wong, 2011). Here, the mean advection of sediment refers to the flux induced by the residual baroclinic and barotropic circulation acting on the mean SSC. The baroclinic circulation corresponds to the classical estuarine exchange with seaward flow near the surface and landward near the bed. Steady theory based on a balance between the pressure gradient force and friction indicates that the magnitude of this exchange (denoted as U in this chapter) is a function of the along-channel salinity gradient ($\partial S/\partial x$), eddy viscosity (A_v), and depth as $U \propto (A_v)^{-1}(\partial S/\partial x)h^3$ (Hansen & Rattray, 1965). It is reasonable then to expect deepening to increase U through the h^3 dependence. However, the response can be more complicated since deepening may also lead to adjustments in eddy viscosity and salinity gradient (Chant et al., 2018; Ralston & Geyer, 2019). The baroclinic exchange flow can also be laterally sheared in channel-shoal systems and feature landward flow in the channel and seaward flow over shoals. This adjustment depends on the lateral depth distribution, Coriolis, density gradient, and basin width through a

parameter space determined by local Kelvin and Ekman numbers (Valle-Levinson et al., 2003). The residual barotropic circulation develops due to the mean seaward pressure gradient induced by the landward Stokes transport (Ianniello, 1979; Valle-Levinson, 2011). In typical estuaries with channel-shoal topography, the structure of the residual barotropic circulation depends on the basin length (L) relative to a quarter tidal wavelength ($L_\theta/4$). In short estuaries ($4L/L_\theta < 0.7$) the residual barotropic flow is seaward in the channel and landward on shoals, and in long systems ($4L/L_\theta > 0.7$) the flow is landward on shoals and seaward in the channel (Li & O'Donnell, 2005). Tidally varying (pumping) sediment fluxes arise from correlated tidal fluctuations of velocity and SSC (Becherer et al., 2016; McSweeney et al., 2016a) and account for the sediment response to tidal asymmetries in velocity due to tidal distortion and to the tidal variability of stratification.

4.2.2 Salinity and SSC in the Delaware Estuary

It is instructive to mention that previous studies have focused on tidal, salt, and sediment dynamics in the relatively modern Delaware Estuary. A recent modeling study of salt fluxes with bathymetry from 1998 found that L_x in the bay is proportional to $Q_r^{-0.11}$, which is a weaker response than the expectation from theory in which $L_x \propto Q_r^{-1/3}$ (Aristizabal & Chant, 2013). The authors attribute this departure to the geometric configuration of the estuary and to the dependence of salt fluxes (i.e. steady shear dispersion and tidal oscillatory flux) and mixing to variability in Q_r. Regarding tides and basin geometry, the length of the basin in $L = 215$ km and the tidal wavelength is $L_\theta = 365$ km (Friedrichs & Aubrey, 1994), therefore the estuary is long ($4L/L_\theta > 0.7$) in the parlance of Li and O'Donnell (2005) and the expected residual barotropic flow is landward over shoals and seaward in the deep channel.

Studies of sediment dynamics in the bay have quantified and reported advective and pumping fluxes based on in-situ measurements and numerical modeling. In the estuarine channel, the mean advection is dominated by the exchange flow while pumping fluxes are driven by settling lag, tidal asymmetries in velocity, and river discharge (Sommerfield & Wong, 2011). An observational study by McSweeney et al. (2016a) reported that mean advection and pumping account for 70% and 30% of the total axial sediment flux, respectively. The same study highlighted the importance of the cross-estuary velocity field on sediment dynamics, which are mainly governed by mean lateral advection. Although sedimentary processes have been studied in the modern bay, the effect of historical dredging on sediment processes remains scarcely studied.

The main goal here is to explore the effect of channel deepening on sediment dynamics in urbanized estuaries with complex topography. We use a coupled circulation and sediment transport model to explore the response of SSC, sediment fluxes, and erosion-deposition patterns to historical dredging in the Delaware estuary, a highly urbanized system on the east coast of the U.S. Comparison with other estuarine systems is facilitated in this study since we consider both the saline reaches of the estuary and the tidal river.

4.3 Methods

4.3.1 Coupled Hydrodynamic and Sediment model

We use the Regional Ocean Modeling System, ROMS (Shchepetkin & McWilliams, 2005; Haidvogel et al., 2008) and the Community Sediment Transport Modeling System, CSTMS (Warner et al., 2008). Digitized historical (1848) and modern (2014) bathymetry

files are employed by the hydrodynamic model as described in chapter 3. Astronomical tidal forcing was obtained from the ADCIRC database (Luettich et al., 1992) and the discharge in the Delaware River at Trenton was set to the median value of 350 m^3/s with no tributaries.

Sediment parameters and initial conditions for sediment are based on a previous modeling and observational study in which CSTMS was calibrated to reflect in-situ collected data (McSweeney, 2017). Three non-cohesive sediment classes with different settling velocities (w_s) are considered and correspond to medium sand, fine sand, and mud (w_s = 40, 3, and 1 mm/s, respectively). Critical stresses for erosion are, in the same order, set to 0.5, 0.1 and 0.05 Pa. The initial bed composition is 60% medium sand, 25% fine sand, and 15% mud, and the bed is allowed to evolve under high erodibility during the model spin-up period to speed up convergence. Riverine sediment loading (Q_s) in the Delaware river was estimated following Nash (1994) as $Q_s = 0.01 Q_r^{1.8}$ (ton/day) with medium sand, fine sand, and mud fractions set to 20%, 75%, and 5% respectively. For further details on the sediment model setup the reader is referred to McSweeney (2017).

4.3.2 Sediment flux decomposition

To obtain sediment fluxes, we express the instantaneous velocity (u) and sediment concentration (C) fields in tidally averaged and fluctuating components as follows:

$$u = \langle u \rangle + u' \tag{4.1}$$

$$C = \langle C \rangle + C' \tag{4.2}$$

where the brackets denote a tidal average (e.g a 36-h lowpass Lanczos filter) and apostrophes indicate fluctuations around the mean. The mean advective sediment flux (F_A) is computed following Sommerfield and Wong (2011):

$$F_A = \langle u \rangle \langle C \rangle \tag{4.3}$$

F_A includes the flux induced by the exchange flow and by the barotropic residual circulation patterns described in the background section. Fluxes due to tidal pumping (F_P) arise from correlated fluctuations around the mean and are computed as (McSweeney et al., 2016a):

$$F_P = \langle u'C' \rangle \tag{4.4}$$

Positive values of F_A and F_P denote landward transport of sediment and seaward when negative.

4.4 Results and discussion

In this section we present model results of salt intrusion, bed stress, and SSC before and after channel deepening, and highlight shifts in the location of ETMs along the estuary. Changes in erosion and deposition patterns and in advective and pumping (axial) fluxes are also discussed in the context of channel deepening. Although we incorporate the hydrodynamic response to deepening in the analysis, a full assessment of the baroclinic response to deepening such as that conducted in recent studies (Chant et al., 2018; Ralston

& Geyer, 2019) is beyond the scope of this work. To focus on the impact of dredging, we only consider modeled scenarios under mean river discharge (350 m^3/s), but acknowledge that seasonal variability is important for sediment dynamics in the bay (McSweeney, 2017).

4.4.1 Effect of dredging on along-channel salinity, bed stress, and SSC

Model results indicate an increase in L_x (defined here as the location of the bottom 2 psu isohaline in the thalweg) from 75 km in 1848 to 100 km in 2014 (factor 1.3, figure 4.1). The adjustment of the salt field to deepening here is similar to that in the Hudson estuary where L_x also increased by a factor of 1.3 over a range of Q_r (Ralston & Geyer, 2019). Consistent with the increased salt intrusion is a 30% drop in the mean along-channel salinity gradient, which we scale as $\partial S/\partial x \sim s_{ocn}/L_x$ where s_{ocn} is the ocean salinity.

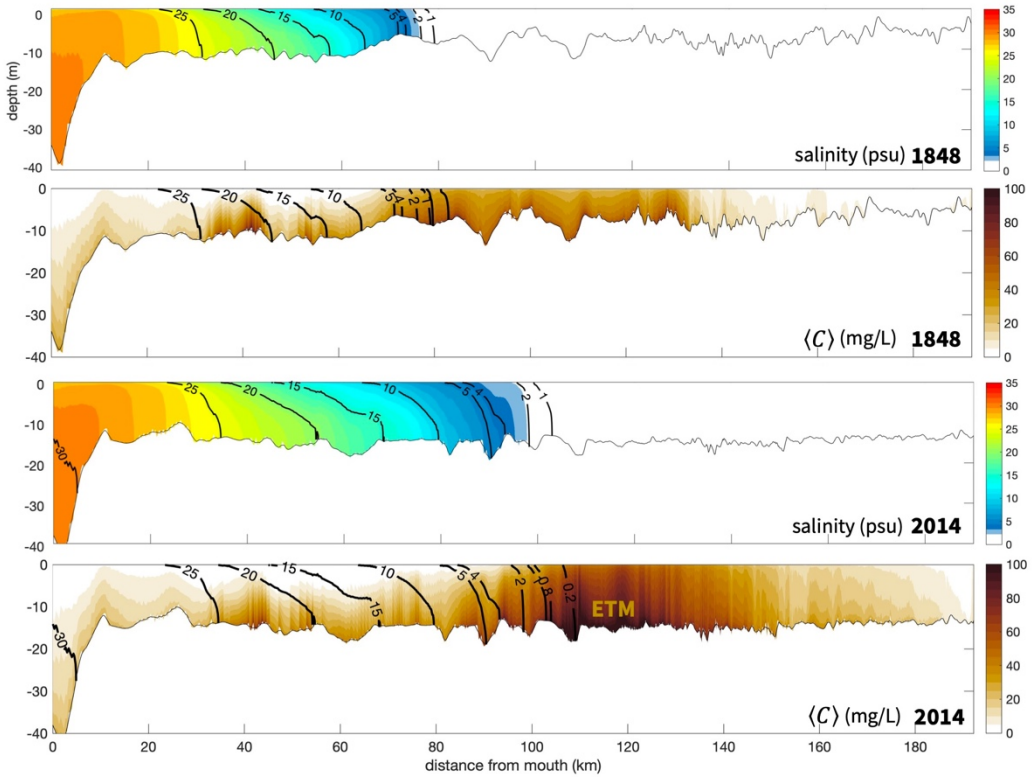

Figure 4.1 Mean along-channel salinity and SSC (colors, psu and mg/L) in 1848 and 2014 under median river discharge at Trenton (350 m^3/s).

Channel deepening had a negligible effect on bed stresses (τ_b) in the lower estuary (0-80 km) but changes are noticeable in the upper estuary and tidal river where the width of the shipping channel is roughly 30%-20% of the total width (figure 4.2). In the pre-dredge scenario, bed stresses were ~0.5-07 Pa on average in the channel and increased to ~1 Pa after deepening, although there is significant variability induced by local topographic undulations in the thalweg. A comparison of root-mean-squared (rms) τ_b between 2014 and 1848 reveals differences in the order of 0.6-1.0 Pa in the thalweg, and indicates that the stress more than doubled in some areas. The general pattern in the tidal river landward km 100 is that the rms τ_b is about twice as large in the modern scenario, with the exception of a segment of a local width constriction (km 150-160) where the stress remained the same after deepening. The doubling of τ_b increases sediment fluxes from the bed to the

water column and alters the bed composition, facilitating horizontal transport and trapping in low energy areas.

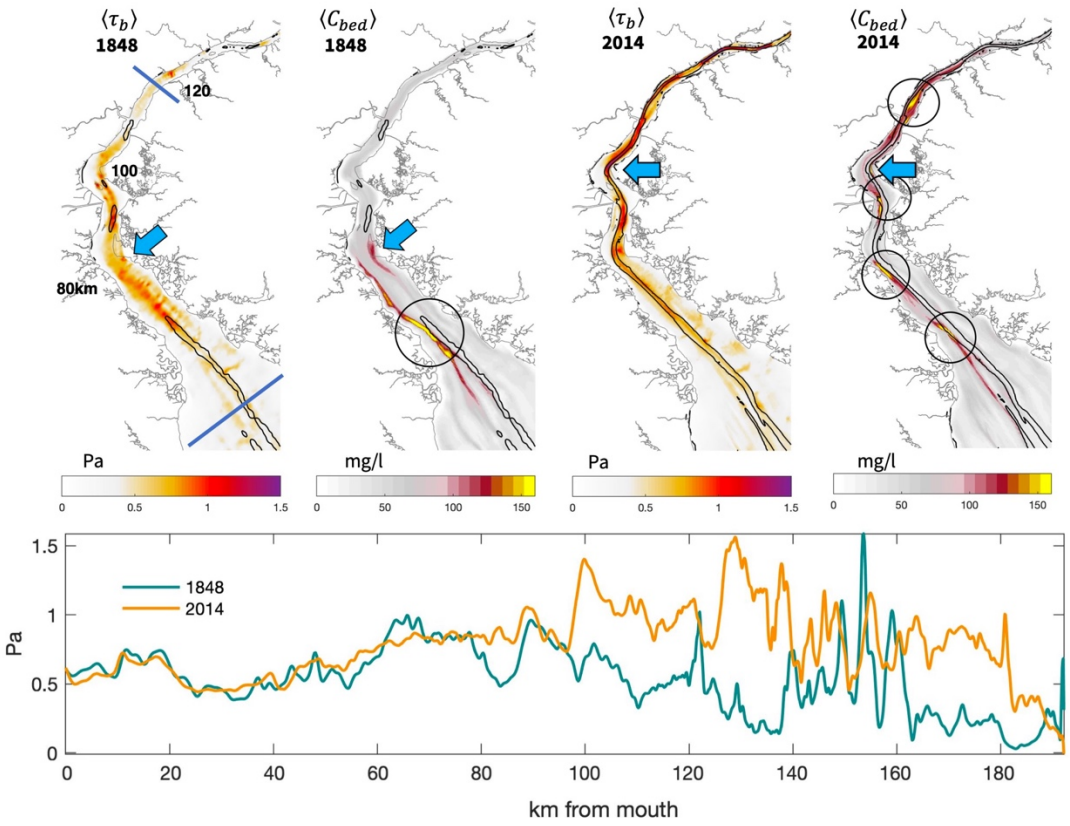

Figure 4.2 (Top) spatial structure of the mean stress magnitude $\langle \tau_b \rangle$ and near-bed SSC $\langle C_{bed} \rangle$ for each modeled scenario. Blue lines denote transects near Bombay Hook and Wilmington, and black circles highlight the location of turbidity maxima ($\langle C_{bed} \rangle$>150 mg/l). (Bottom) root-mean-squared bed stresses in the thalweg from the mouth to the head of the tides.

Changes to the near bed sediment concentration as well as the axial distribution of SSC in the estuary are shown in figures 4.1 and 4.2 (top). In 1848, the maximum near-bed sediment concentration (i.e. the main ETM) is found between 60 and 80 km. This ETM can be seen more clearly in the areal plot (4.2 top) and not in the along-thalweg section (figure 4.1) because it is located at a lateral bathymetric transition from shoal to channel on the

Delaware side (west) rather than in the deep thalweg. Although the axial coordinate of this ETM coincides with the salt intrusion length, the lateral distribution of sediment concentration suggests that both lateral and axial processes modulate SSC in the estuary, in agreement with findings in the modern estuary by McSweeney et al. (2016a). In 2014, the main ETM is about 25-30 km landward from the position in 1848, consistent with the increase in salt intrusion length after channel deepening. The main ETM in the post-dredge scenario is located in a narrower section of the river (km 100-120), and the near-bed sediment concentration is relatively high both on shoals and in the shipping channel. Comparison of the pre and post-dredge scenarios reveals an increase in near bed sediment concentration of up to 80 mg/l between 100 and 120 km, coincident with the area where bed stresses more than doubled (see black circles in figure 4.2). In 2014, secondary ETMs can also be found seaward from the main ETM and at lateral topographic transitions, similar to the main ETM in 1848.

4.4.2 Dredging and cross-estuary patterns of SSC, erosion, and deposition

For insight into the cross-channel structure of the main and secondary ETMs in the estuary, we present results of lateral salinity and turbidity patterns over a tidal cycle at km 60 near Bombay Hook (figure 4.3 for 1848 and 4.4 for 2014). In the historical case, lateral salinity gradients develop in two deep channels during late flood, and the maximum turbidity is found on lateral slopes from shoals to channels where cross-estuary salinity gradients are formed. These lateral gradients are such that conditions are saltier in the channel and fresher over shallower areas due to the differential along-channel advection of salt. During late flood when conditions are relatively well mixed and two local SSC maxima of about 150 mg/l extend halfway up the water column. During mid ebb,

stratification suppresses turbidity to ~50 mg/l and the lateral salt fronts weaken. In late ebb minutes before the onset of the flood, the lateral salt fronts form again and SSC increases over lateral channel slopes.

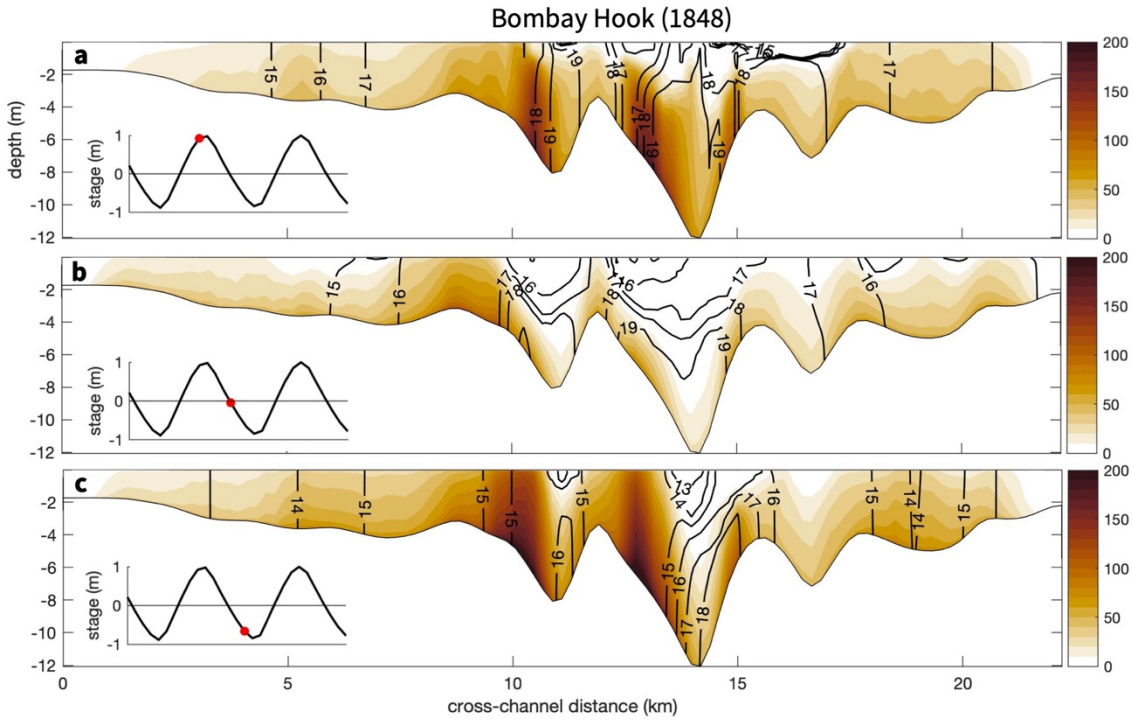

Figure 4.3 Modeled cross-estuary SSC (colors, mg/l) and salinity (contours, psu) at Bombay Hook in 1848 during (a) late flood, (b) mid ebb and (c) late ebb. Tidal stage (m) is shown in all panels.

In 2014, (figure 4.4), the tidal variability of salinity and sediment concentration across the channel is similar to that in 1848 in that there are lateral salinity gradients that drive sediment towards topographic transitions. However, note that the salinity of these fronts is 20-21 psu in contrast the 1848 cross section (18-19 psu), consistent with the landward migration of the salinity intrusion.

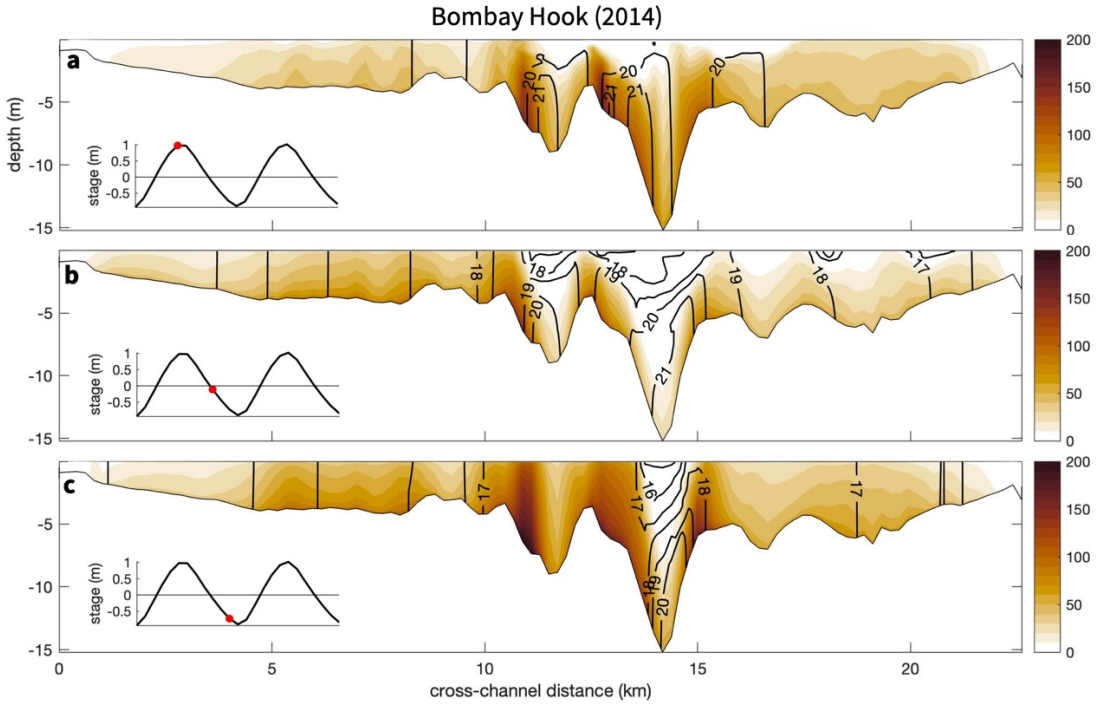

Figure 4.4 Same legend as figure 4.3 but in the 2014 scenario.

The lateral coupling between sediment and salinity shown in figures 4.3 and 4.4 corresponds with areal patterns of deposition and erosion in the estuary (figure 4.5). The bed thickness evolution over 1 month reveals net deposition on shoals and on lateral slopes while erosion dominated in the channel. This channel-shoal asymmetry in bed thickness change is also consistent with the lateral gradients in bed stress shown in figure 4.2 (top). Together, bed change patterns and the lateral dynamics in the saline estuary suggest that sediment particles are resuspended during flood and advected laterally mainly due to cross-channel density gradients. Through this mechanism, the near bed sediment transport is from a high to a low energy region (i.e. from the channel to a lateral topographic transition) where deposition ultimately occurs when the water column is stratified. To locate the segments along the estuary where deposition is more likely to occur, we computed the total mass of sediment that accumulated and eroded in the along-channel direction and obtained the net deposition per unit length (figure 4.5c). Model results indicate that there are several

segments of the estuary where sediment deposition is likely to occur rather than just at the limit of the salinity intrusion for each case. In 1848, there are three depositional zones (i.e. 'hotspots' with deposition>50 ton/km) in the saline estuary between kilometers 50 and 75 while in 2014 there are two in zones the 75-100km segment with the same magnitude (max 100 ton/km). These results suggest that channel deepening mainly led to the landward migration of the estuarine sediment trapping zones.

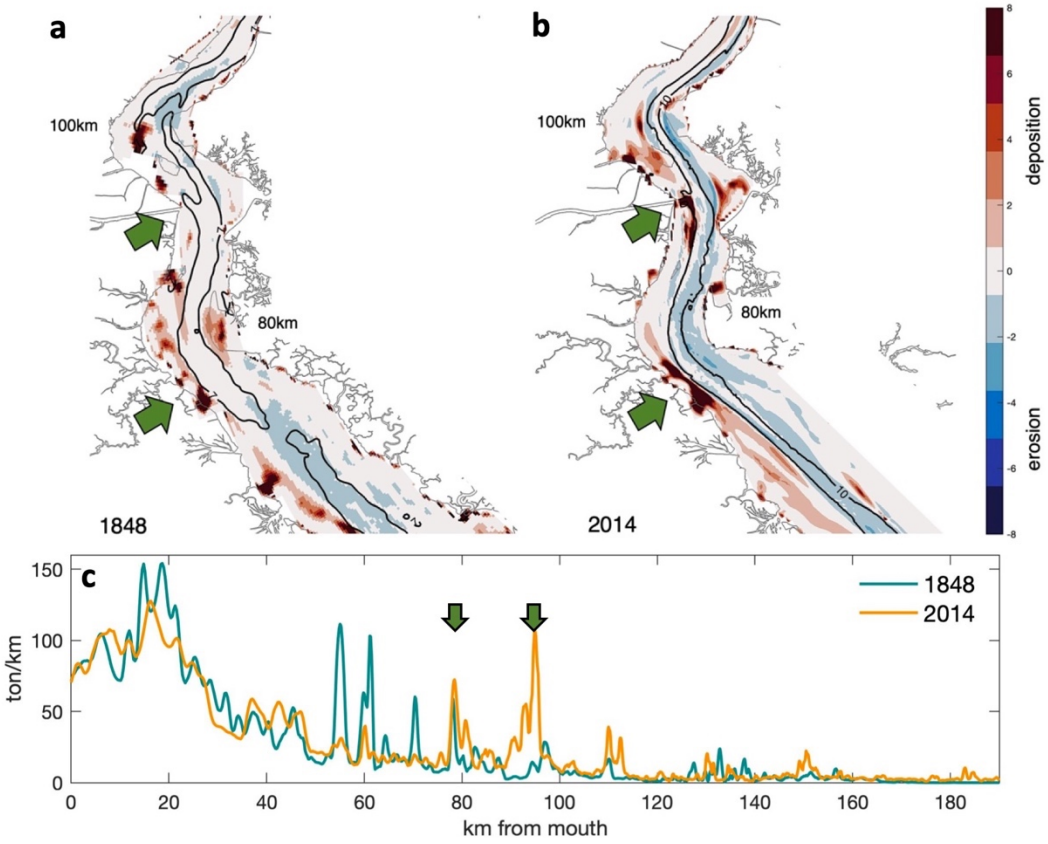

Figure 4.5 Change in bed thickness after a 1-month run in (a) 1848 and (b) 2014. Blue and red denote erosion and deposition, respectively (mm). Two green arrows are drawn to highlight enhanced deposition in the 2014 scenario, but are also plotted in (a) for reference. (c) Cross-section integrated net sediment deposition along the estuary in ton/km (i.e. deposition – erosion). Peaks in sediment trapping (green arrows) are the same shown on (a) and (b).

Historical changes in sediment transport from channel to shoals motivate a discussion of sediment supply to nearshore wetlands of the bay, some of which have undergone extensive shoreline retreat over the last century. For example, in figure 4.6a we show the location of a tidal gauge at the mouth of Leipsic Creek on the Delaware coast that was in operation in 1882 (purple diamond, coordinates shown). This is a snapshot of a tidal record notebook retrieved from the U.S. National Archives and Records Administration. In figure 4.6b, the yellow pin (Google Earth) shows that the gauge location in May 2019 is about 900 m into the bay, and provides evidence of shoreline erosion from the late 1800s to 2019. Model results in this study (4.6 c-f) reveal diminished sediment deposition in the same area in 2014 compared to 1848, as well as a smaller fraction of fine sediment (i.e.. mud) on the flanks near. The latter is indicative of a reduction in lateral sediment supply at this specific location. A recent study of salt marsh dynamics found that even modest shifts in sediment supply can, regardless of the sea level rise scenario, make the difference from marsh accretion to loss (Fagherazzi et al., 2013). Although it would be premature to attribute the observed shoreline retreat to channel deepening (our model runs neglect seasonal variability in riverine sediment supply), we anticipate these results to motivate further studies on the effect of dredging on marsh sediment budgets.

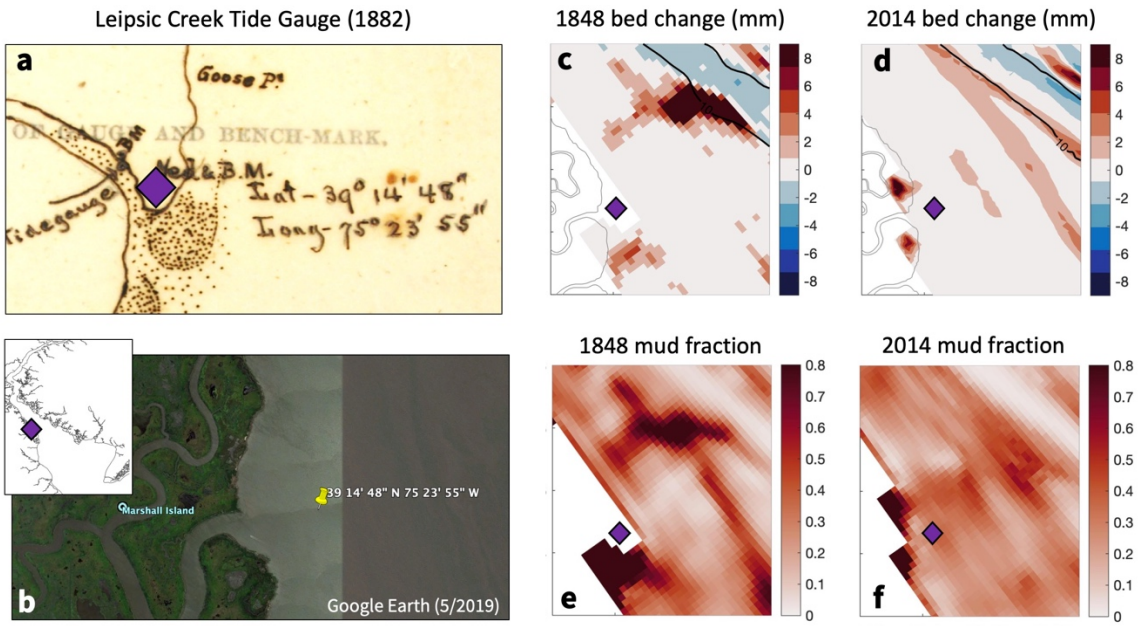

Figure 4.6 Observed shoreline retreat and modeled changes to sediment supply near Marshall Island wetland. (a) Coordinates of a tidal gauge in Leipsic creek (Delaware coastline) in 1882, (b) same coordinates in 2019 from Google Earth, (c-d) modeled bed change in 1848 and 2014 after a 1-month run, and (e-f) modeled mud fraction in 1848 and 2014 at the end of the run. The purple marker denotes the location of the tidal gauge in 1882. Snapshot in (a) was retrieved from the U.S. National Archives and Records Administration.

4.4.3 Impact of dredging on the advection and tidal pumping of sediment

In the previous sections, we showed that sediment trapping occurs at topographic transitions associated with lateral salinity gradients. Channel deepening caused a landward migration of the trapping zones, which are linked to several ETMs along the channel rather than to the main ETM. Since the lateral depth distribution is key for sediment dynamics, next we consider the role of topography on shifts in the exchange flow as well as in the mean advection and tidal pumping of sediment. In this last part we seek to integrate channel deepening with the residual circulation in the discussion of sediment dynamics, and highlight differences in the response to dredging in both the saline and unstratified reaches of the estuary.

To examine changes to the exchange flow in the channel, we calculate the bulk subtidal shear (ΔU), defined as the difference between the peak seaward and landward residual velocities (Chant et al., 2018). Model results of the vertical structure of the exchange flow and ΔU along the channel are shown in figure 4.7. The maximum ΔU was found between kilometers 45 and 55 in both modeled scenarios, with an increase after deepening by a factor of about 1-1.25 in that segment. In both 1848 and 2014, the magnitude of the subtidal shear drops from the maximum value to about zero at the location of the salt front.

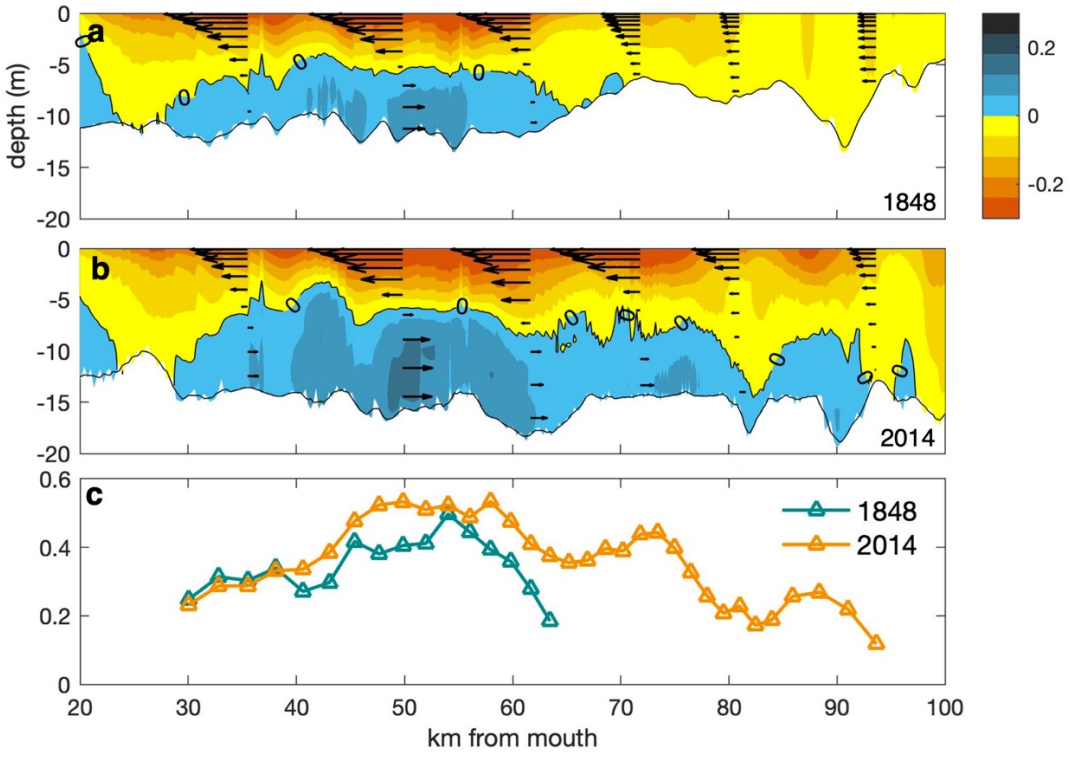

Figure 4.7 Mean along-channel velocity in (a) 1848 and (b) 2014 in the estuary (units m/s). (c) Subtidal shear (ΔU) in each modeled scenario (see text for definition).

Mean SSC $\langle C \rangle$, residual along-estuary velocity $\langle u \rangle$, and mean advective sediment fluxes (F_A) through sections near Bombay Hook and Wilmington are shown on figures 4.8 and 4.9. In Bombay Hook, F_A mimics the classical exchange flow pattern with landward flux

near the bed and seaward near the surface in both 1848 and 2014, although the cross-channel depth distribution led to significant departures from purely vertically sheared exchange (Valle-Levinson, 2011). Topographic variability here leads to landward fluxes in the main and secondary channels and seaward over shoals. Differences in mean advection between 1848 and 2014 at Bombay Hook are not significant even though the along-channel salt gradient decreased through the increase in L_x. In contrast, the historical shift in Wilmington was noteworthy. In 1848, the mean advection there was landward over shallow areas and seaward in the deep channel and the conditions were unstratified. As indicated in the introduction, the residual barotropic circulation in 'long' channel-shoal estuaries is seaward in the channel and landward over shoals, consistent with patterns in F_A in Wilmington (1848). In 2014, patterns in the mean advection also mimic barotropic dynamics but the magnitude of the flux increased following the elevated $\langle C \rangle$. This departure is possibly due to the response of the residual flow to the steepening of the residual water elevation due to the tidal Stokes drift (see chapter 3).

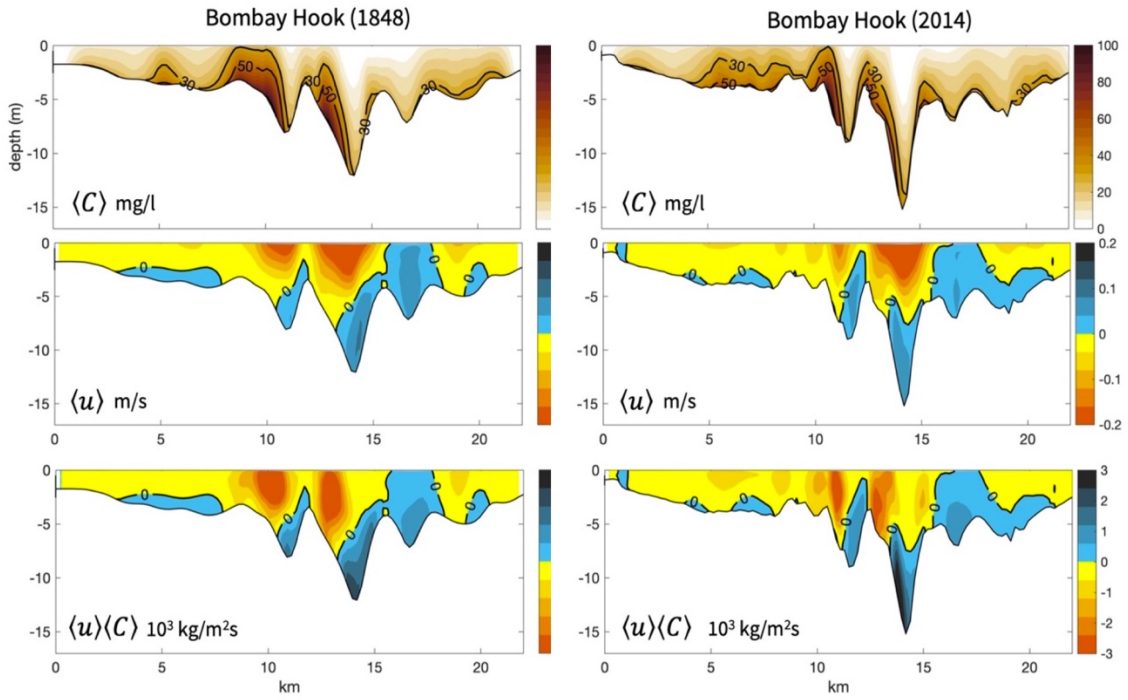

Figure 4.8 (Top) Mean sediment concentration, (middle) residual velocity, and (bottom) mean advection of sediment in Bombay Hook in (left) 1848 and (right) 2014 Positive values of velocity and flux denote the landward direction.

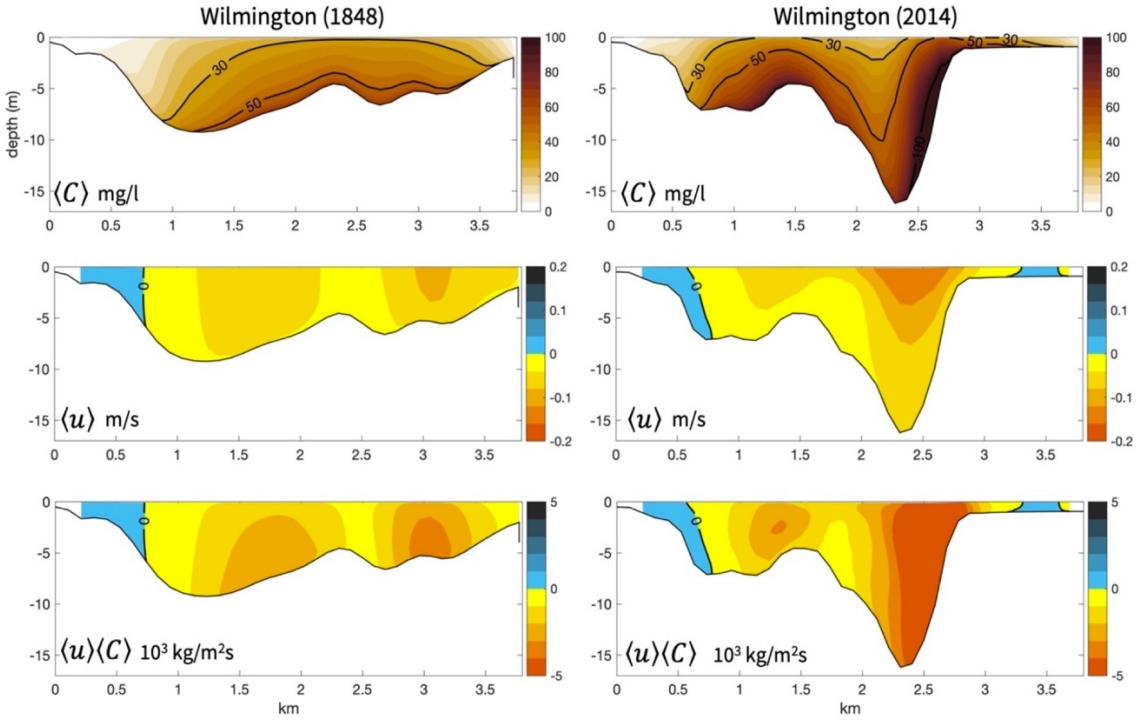

Figure 4.9 Same legend as figure 4.8 but in Wilmington.

Fluxes due to tidal pumping (F_P, figure 4.10) are strongly dependent on tidal asymmetries in velocity and SSC as reported by Sommerfield and Wong (2011). In the estuary, SSC increases during the flood and decreases in ebb. The tidal asymmetry in SSC in conjunction with flood dominant conditions (see chapter 3), leads to landward tidal pumping of sediment through correlated fluctuations in velocity and sediment concentration. In Bombay Hook, F_P is landward in the channel and seaward near the surface, and the lateral depth distribution seems to determine the transition between landward and seaward pumping. The laterally sheared pattern here is possibly caused by asymmetries in stratification and by near-surface ebb-dominance caused by river discharge. In contrast, pumping fluxes are predominately landward in Wilmington for both modeled scenarios.

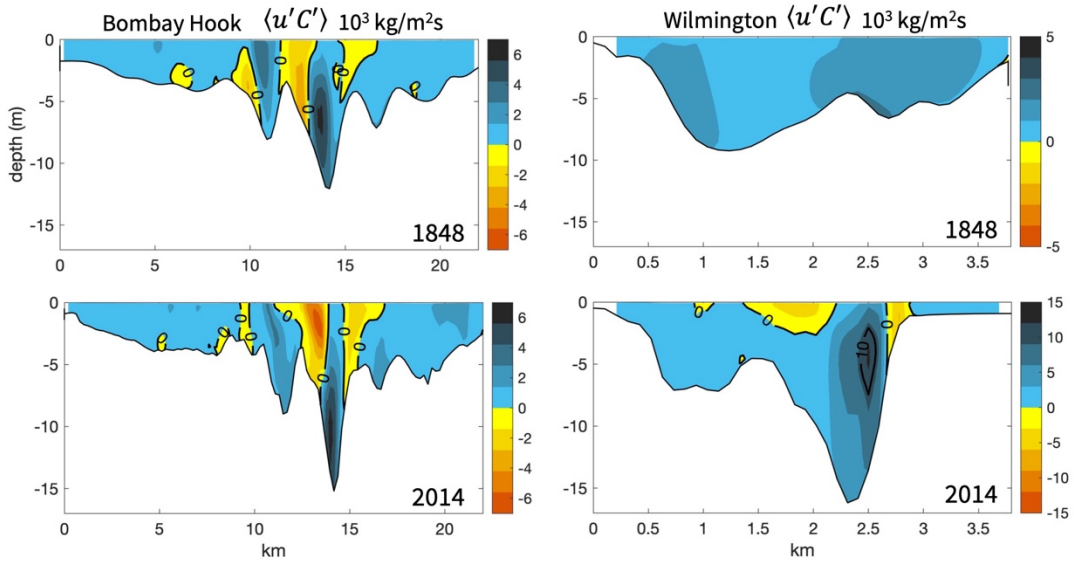

Figure 4.10 Tidal pumping fluxes in (left) Bombay Hook and (right) Wilmington for the (top) 1848 and (bottom) 2014 scenarios.

4.5 Summary and conclusions

In this study we evaluated the impact of channel deepening on SSC, sediment trapping, and fluxes (particularly mean advection and tidal pumping) in the Delaware Estuary. We considered both the saline and unstratified reaches of the system for a broader perspective on anthropogenic geomorphic change on estuarine sediment dynamics. To evaluate the response of sediment to dredging, we briefly explored the adjustment of the exchange flow, salt intrusion, stratification, and bed stresses in the system under mean river discharge conditions. The salt intrusion length increased by a factor of 1.3. Bed stresses increased and more than doubled in some areas after deepening, consistent with a reduction in hydraulic drag. The modeled sediment response is closely tied to shifts in hydrodynamics. SSC increased from 1848 to 2014 mainly due increases bed stresses. In both 1848 and 2014, primary and secondary turbidity maxima developed along stratified reaches of the estuary and were located mainly at lateral bathymetric transitions rather than at one single location at the limit of the salt intrusion. The location of sediment deposition areas shifted landward after channel deepening, but the magnitude of the trapping did not dramatically change. In terms of fluxes, the mean advection was landward in the channels and seaward over shoals in the saline estuary, and the opposite pattern was observed in the tidal river. Pumping fluxes were predominately landward in both the saline and fresh segments of the system due to flood dominance, and increased in 2014 due to swifter tidal currents and larger sediment resuspension.

Chapter 5 - Conclusions

In this thesis we employed numerical models of waves, currents, and sediment transport with historical and modern bathymetry to study the effect of channel deepening on wind waves, barotropic tides, and sediment dynamics in the Delaware Estuary.

The coupled model revealed that Stokes-Coriolis, vortex, and breaking forces only had a minor contribution to the leading momentum balance during a typical storm, which was mainly between vertical stress divergence and pressure gradient force. However, we highlight that local wind waves increase the surface drag coefficient by up to 30% during typical storm conditions with respect to drag formulations that neglect the spatial variability of the wave field. Wind and wave direction are also critical for the magnitude of the depth-integrated subtidal exchange. We adjusted the model to prevent whitecapping wave dissipation from creating breaking forces since that contribution is already included in the wind stress. Results here are generalizable to young seas in estuaries.

Second, we examined the role of channel deepening on tidal amplification and flux transmission. Model results revealed a doubling in tidal range near the head of the tides, consistent with a reduction in hydraulic drag and relatively unchanged width convergence. Tidal current amplitude along the channel doubled in some areas and were strongly modulated by undulations in channel topography. Channel deepening also altered the arrival time of high water in the system, especially in the tidal river where high water arrives about an hour earlier now than in the mid 1800s. The tidal wave became more progressive after deepening and tidal energy fluxes increased.

The last part consisted of a modeling study on the effect of channel deepening on suspended sediment concentration and fluxes. The salt intrusion length increased by a factor of 1.3. Bed stresses increased and more than doubled in some areas after deepening, consistent with a reduction in bed drag. In both modeled scenarios, main and secondary turbidity maxima developed along the estuary and were located mainly at lateral transitions rather than at one single location at the limit of the salt intrusion. The location of sediment deposition areas shifted landward after channel deepening, but the magnitude of the trapping did not dramatically change. Patterns in the mean advection of sediment were controlled by the classical exchange flow mechanism in the saline estuary and by the residual barotropic circulation in the fresh, tidal river. Pumping fluxes were predominately landward due to flood dominance caused by the frictional distortion of the tidal wave.

Acknowledgement of Previous Publications

Chapter 2 has been published:

Pareja-Roman L.F; Chant, R. J., Ralston, D. K (2019). Effects of Locally Generated Wind Waves on the Momentum Budget and Subtidal Exchange in a Coastal Plain Estuary. Journal of Geophysical Research: Oceans. https://doi.org/10.1029/2018JC014585

Chapter 3 is currently under review under the title:

Pareja-Roman L.F; Chant, R. J. Sommerfield, C. Impact of Dredging on Tidal Hydraulics in Delaware Bay and Tidal River. (For: Journal of Geophysical Research: Oceans)

References

Aiki, H., & Greatbatch, R. J. (2014). A New Expression for the Form Stress Term in the Vertically Lagrangian Mean Framework for the Effect of Surface Waves on the Upper- Ocean Circulation. *J Phys Oceanogr, 44*(1), 3-23. doi: 10.1175/Jpo-D-12-0228.1

Allen, G. P., Salomon, J. C., Bassoullet, P., Du Penhoat, Y., & de Grandpré, C. (1980). Effects of tides on mixing and suspended sediment transport in macrotidal estuaries. *Sediment. Geol., 26*(1), 69-90. doi: https://doi.org/10.1016/0037-0738(80)90006-8

Ardhuin, F., Chapron, B., & Elfouhaily, T. (2004). Waves and the air-sea momentum budget: Implications for ocean circulation modeling. *J Phys Oceanogr, 34*(7), 1741-1755. doi: Doi 10.1175/1520-0485(2004)034<1741:Watamb>2.0.Co;2

Aristizabal, M., & Chant, R. (2013). A Numerical Study of Salt Fluxes in Delaware Bay Estuary. *J Phys Oceanogr, 43*(8), 1572-1588. doi: 10.1175/Jpo-D-12-0124.1

Aubrey, D. G., & Speer, P. E. (1985). A Study of Non-Linear Tidal Propagation in Shallow Inlet Estuarine Systems .1. Observations. *Estuar Coast Shelf S, 21*(2), 185-205. doi: Doi 10.1016/0272-7714(85)90096-4

Battjes, J. A., & Janssen, P. F. M. (1978). Energy Loss and Set-Up Due to Breaking of Random Waves. *Coastal Engineering 1978*.

Becherer, J., Floser, G., Umlauf, L., & Burchard, H. (2016). Estuarine circulation versus tidal pumping: Sediment transport in a well-mixed tidal inlet. *J Geophys Res-Oceans, 121*(8), 6251-6270. doi: 10.1002/2016jc011640

Beudin, A., Ganju, N. K., Defne, Z., & Aretxabaleta, A. L. (2017). Physical response of a back-barrier estuary to a post-tropical cyclone. *J Geophys Res-Oceans, 122*(7), 5888-5904. doi: 10.1002/2016jc012344

Blood, W. (1918). Hog Island: The Greatest Shipyard in the World. *Transactions of the Institute of Naval Architects and Marine Engineers*.

Boerema, A., & Meire, P. (2017). Management for estuarine ecosystem services: A review. *Ecol Eng, 98*, 172-182. doi: https://doi.org/10.1016/j.ecoleng.2016.10.051

Booij, N., Ris, R. C., & Holthuijsen, L. H. (1999). A third-generation wave model for coastal regions - 1. Model description and validation. *J Geophys Res-Oceans, 104*(C4), 7649-7666. doi: Doi 10.1029/98jc02622

Bricker, J. D. (2003). Bed drag coefficient variability under wind waves in a tidal estuary : field measurements and numerical modeling. In S. G. Monismith (Ed.).

Bricker, J. D., Inagaki, S., & Monismith, S. G. (2004). Modelling the effects of bed drag coefficient variability under wind waves in South San Francisco Bay. *Estuarine and Coastal Modeling, Proceedings*, 89-107.

Brooks, W. A. (1841). *Treatise on the improvement of the navigation of rivers*: Oxford University.

Burchard, H., Schuttelaars, H. M., & Ralston, D. K. (2018). Sediment Trapping in Estuaries. *Annual review of marine science, 10*(1), 371-395. doi: 10.1146/annurev-marine-010816-060535

Cai, H., Savenije Hubert, H. G., Yang, Q., Ou, S., & Lei, Y. (2012a). Influence of River Discharge and Dredging on Tidal Wave Propagation: Modaomen Estuary Case.

Journal of Hydraulic Engineering, 138(10), 885-896. doi: 10.1061/(ASCE)HY.1943-7900.0000594

Cai, H. Y., Savenije, H. H. G., & Toffolon, M. (2012b). A new analytical framework for assessing the effect of sea-level rise and dredging on tidal damping in estuaries. *J Geophys Res-Oceans, 117*. doi: Artn C09023
10.1029/2012jc008000

Carniel, S., Warner, J. C., Chiggiato, J., & Sclavo, M. (2009). Investigating the impact of surface wave breaking on modeling the trajectories of drifters in the northern Adriatic Sea during a wind-storm event. *Ocean Model. Online, 30*(2-3), 225-239. doi: 10.1016/j.ocemod.2009.07.001

Cavaleri, L., & Malanotte-Rizzoli, P. (1981). Wind wave prediction in shallow water: Theory and applications. *Journal of Geophysical Research: Oceans, 86*(C11), 10961-10973. doi: doi:10.1029/JC086iC11p10961

Chant, R. J., Sommerfield, C. K., & Talke, S. A. (2018). Impact of Channel Deepening on Tidal and Gravitational Circulation in a Highly Engineered Estuarine Basin. *Estuar Coast, 41*(6), 1587-1600. doi: 10.1007/s12237-018-0379-6

Charnock, H. (1955). Wind stress on a water surface. *Quarterly Journal of the Royal Meteorological Society, 81*(350), 639-640. doi: 10.1002/qj.49708135027

Chen, J.-L., Ralston, D. K., Geyer, W. R., Sommerfield, C. K., & Chant, R. J. (2018). Wave Generation, Dissipation, and Disequilibrium in an Embayment With Complex Bathymetry. *Journal of Geophysical Research: Oceans, 123*. doi: doi:10.1029/2018JC014381

Chernetsky, A. S., Schuttelaars, H. M., & Talke, S. A. (2010). The effect of tidal asymmetry and temporal settling lag on sediment trapping in tidal estuaries. *Ocean Dynamics, 60*(5), 1219-1241. doi: 10.1007/s10236-010-0329-8

Cho, H. J. (2007). Effects of Prevailing Winds on Turbidity of a Shallow Estuary. *Int. J. Env. Res. Public Health, 4*(2), 185-192.

Church, J. C., & Thornton, E. B. (1993). Effects of breaking wave induced turbulence within a longshore current model. *Coastal Engineering, 20*(1), 1-28. doi: https://doi.org/10.1016/0378-3839(93)90053-B

Craig, P. D., & Banner, M. L. (1994). Modeling Wave-Enhanced Turbulence in the Ocean Surface Layer. *J Phys Oceanogr, 24*(12), 2546-2559. doi: 10.1175/1520-0485(1994)024<2546:mwetit>2.0.co;2

Craik, A. D. D., & Leibovich, S. (1976). A rational model for Langmuir circulations. *J Fluid Mech, 73*(3), 401-426. doi: doi:10.1017/S0022112076001420

Csanady, G. T. (1973). Wind-Induced Barotropic Motions in Long Lakes. *J Phys Oceanogr, 3*(4), 429-438. doi: 10.1175/1520-0485(1973)003<0429:wibmil>2.0.co;2

Cummins, P. F., & Oey, L.-Y. (1997). Simulation of Barotropic and Baroclinic Tides off Northern British Columbia. *J Phys Oceanogr, 27*(5), 762-781. doi: 10.1175/1520-0485(1997)027<0762:SOBABT>2.0.CO;2

de Jonge, V. N. (1983). Relations Between Annual Dredging Activities, Suspended Matter Concentrations, and the Development of the Tidal Regime in the Ems Estuary. *Can. J. Fish. Aquat. Sci., 40*(S1), s289-s300. doi: 10.1139/f83-290

de Jonge, V. N., Schuttelaars, H. M., van Beusekom, J. E. E., Talke, S. A., & de Swart, H. E. (2014). The influence of channel deepening on estuarine turbidity levels and dynamics, as exemplified by the Ems estuary. *Estuar. Coast. Shelf Sci., 139*, 46-59. doi: https://doi.org/10.1016/j.ecss.2013.12.030

Dean, R. G., & Dalrymple, R. A. (2001). *Coastal Processes with Engineering Applications*. Cambridge: Cambridge University Press.

Devlin, A. T., Jay, D. A., Talke, S. A., Zaron, E. D., Pan, J. Y., & Lin, H. (2017). Coupling of sea level and tidal range changes, with implications for future water levels. *Scientific reports, 7*. doi: ARTN 17021
10.1038/s41598-017-17056-z

Díez-Minguito, M., Baquerizo, A., Ortega-Sánchez, M., Navarro, G., & Losada, M. (2012). Tide transformation in the Guadalquivir estuary (SW Spain) and process-based zonation. *Journal of Geophysical Research: Oceans, 117*(C3).

DiLorenzo, J., Huang, P., Uewellyn Thatcher, M., & O Najarian, T. (1993). Dredging impacts of Delaware estuary tides *3rd International Conference, Estuarine and Coastal Modeling* (pp. 86): American Society of Civil Engineers.

Dingemans, M. W., Radder, A. C., & De Vriend, H. J. (1987). Computation of the driving forces of wave-induced currents. *Coastal Engineering, 11*(5), 539-563. doi: https://doi.org/10.1016/0378-3839(87)90026-3

Donelan, M. A. (1990). Air-Sea Interaction. In B. Le Mehaute & D. M. Hanes (Eds.), *The Sea* (Vol. 9, pp. 239-292). New York: John Wiley.

Donelan, M. A., Hamilton, J., & Hui, W. (1985). Directional spectra of wind-generated ocean waves. *Philosophical Transactions of the Royal Society of London. Series A. Mathematical and Physical Sciences, 315*(1534), 509. doi: 10.1098/rsta.1985.0054

Drennan, W. M., Graber, H. C., Hauser, D., & Quentin, C. (2003). On the wave age dependence of wind stress over pure wind seas. *Journal of Geophysical Research: Oceans, 108*(C3). doi: doi:10.1029/2000JC000715

Drennan, W. M., Taylor, P. K., & Yelland, M. J. (2005). Parameterizing the sea surface roughness. *J Phys Oceanogr, 35*(5), 835-848. doi: Doi 10.1175/Jpo2704.1

Dyer, K. R. (1995). Chapter 14 Sediment Transport Processes in Estuaries. In G. M. E. Perillo (Ed.), *Developments in Sedimentology* (Vol. 53, pp. 423-449): Elsevier.

Dzwonkowski, B., Wong, K. C., & Ullman, W. J. (2014). Water Level and Velocity Characteristics of a Salt Marsh Channel in the Murderkill Estuary, Delaware. *Journal of Coastal Research, 30*(1), 63-74. doi: 10.2112/Jcoastres-D-12-00161.1

Edson, J. B., Jampana, V., Weller, R. A., Bigorre, S. P., Plueddemann, A. J., Fairall, C. W., . . . Hersbach, H. (2013). On the Exchange of Momentum over the Open Ocean. *J Phys Oceanogr, 43*(8), 1589-1610. doi: 10.1175/JPO-D-12-0173.1

Elsey-Quirk, T. (2016). Impact of Hurricane Sandy on salt marshes of New jersey. *Estuar Coast Shelf S, 183*, 235-248. doi: 10.1016/j.ecss.2016.09.006

Fagherazzi, S., Mariotti, G., Wiberg, P., & McGlathery, K. (2013). Marsh Collapse Does Not Require Sea Level Rise. *Oceanography, 26*(3), 70-77. doi: 10.5670/oceanog.2013.47

Fairall, C. W., Bradley, E. F., Hare, J. E., Grachev, A. A., & Edson, J. B. (2003). Bulk parameterization of air-sea fluxes: Updates and verification for the COARE algorithm. *J. Clim., 16*(4), 571-591. doi: Doi 10.1175/1520-0442(2003)016<0571:Bpoasf>2.0.Co;2

Fairall, C. W., Bradley, E. F., Rogers, D. P., Edson, J. B., & Young, G. S. (1996). Bulk parameterization of air-sea fluxes for Tropical Ocean Global Atmosphere Coupled Ocean Atmosphere Response Experiment. *J Geophys Res-Oceans, 101*(C2), 3747-3764. doi: Doi 10.1029/95jc03205

Familkhalili, R., & Talke, S. A. (2016). The effect of channel deepening on tides and storm surge: A case study of Wilmington, NC. *Geophys Res Lett, 43*(17), 9138-9147. doi: 10.1002/2016gl069494

Fisher, A. W., Sanford, L. P., Scully, M. E., & Suttles, S. E. (2017). Surface Wave Effects on the Translation of Wind Stress across the Air–Sea Interface in a Fetch-Limited, Coastal Embayment. *J Phys Oceanogr, 47*(8), 1921-1939. doi: 10.1175/JPO-D-16-0146.1

Fisher, A. W., Sanford, L. P., & Suttles, S. E. (2015). Wind Stress Dynamics in Chesapeake Bay: Spatiotemporal Variability and Wave Dependence in a Fetch-Limited Environment. *J Phys Oceanogr, 45*(10), 2679-2696. doi: 10.1175/Jpo-D-15-0004.1

Friedrichs, C. (2010). Barotropic tides in channelized estuaries. In A. Valle-Levinson (Ed.), *Contemporary Issues in Estuarine Physics* (pp. 27-61). Cambridge: Cambridge University Press.

Friedrichs, C. T., & Aubrey, D. G. (1994). Tidal Propagation in Strongly Convergent Channels. *J Geophys Res-Oceans, 99*(C2), 3321-3336. doi: Doi 10.1029/93jc03219

Friedrichs, C. T., & Madsen, O. S. (1992). Nonlinear Diffusion of the Tidal Signal in Frictionally Dominated Embayments. *J Geophys Res-Oceans, 97*(C4), 5637-5650. doi: Doi 10.1029/92jc00354

Ganju, N. K., Schoellhamer, D. H., & Bergamaschi, B. A. (2005). Suspended sediment fluxes in a tidal wetland: Measurement, controlling factors, and error analysis. *Estuaries, 28*(6), 812-822. doi: 10.1007/BF02696011

Garcia-Nava, H., Ocampo-Torres, F. J., & Hwang, P. A. (2012). On the parameterization of the drag coefficient in mixed seas. *Sci Mar, 76*, 177-186. doi: 10.3989/scimar.03615.19F

Garvine, R. W. (1985). A simple model of estuarine subtidal fluctuations forced by local and remote wind stress. *Journal of Geophysical Research: Oceans, 90*(C6), 11945-11948. doi: 10.1029/JC090iC06p11945

Geyer, W. R. (1997). Influence of wind on dynamics and flushing of shallow estuaries. *Estuar Coast Shelf S, 44*(6), 713-722. doi: DOI 10.1006/ecss.1996.0140

Godin, G. (1985). Modification of River Tides by the Discharge. *J Waterw Port C-Asce, 111*(2), 257-274. doi: Doi 10.1061/(Asce)0733-950x(1985)111:2(257)

Grant, W. D., & Madsen, O. S. (1982). Movable Bed Roughness in Unsteady Oscillatory Flow. *J Geophys Res-Oc Atm, 87*(Nc1), 469-481. doi: DOI 10.1029/JC087iC01p00469

Haidvogel, D. B., Arango, H., Budgell, W. P., Cornuelle, B. D., Curchitser, E., Di Lorenzo, E., . . . Wilkin, J. (2008). Ocean forecasting in terrain-following coordinates: Formulation and skill assessment of the Regional Ocean Modeling System. *J. Comput. Phys., 227*(7), 3595-3624. doi: 10.1016/j.jcp.2007.06.016

Hansen, D., & Rattray, M. (1965). Gravitational circulation in straits and estuaries. *J. Mar. Res., 23*, 104-122.

Hansen, D., & Rattray, M. (1966). New dimensions in estuary classification. *Limnology and Oceanography, 11*, 319-326.

Henrie, K., & Valle-Levinson, A. (2014). Subtidal variability in water levels inside a subtropical estuary. *J Geophys Res-Oceans, 119*(11), 7483-7492. doi: 10.1002/2014jc009829

Holleman, R. C., & Stacey, M. T. (2014). Coupling of Sea Level Rise, Tidal Amplification, and Inundation. *J Phys Oceanogr, 44*(5), 1439-1455. doi: 10.1175/Jpo-D-13-0214.1

Holthuijsen, L. H. (2007). *Waves in Oceanic and Coastal Waters*. Cambridge: Cambridge University Press.

Holthuijsen, L. H. (2010). *Waves in Oceanic and Coastal Waters*: Cambridge University Press.

Horowitz, A. J., Elrick, K. A., Smith, J. J., & Stephens, V. C. (2014). The effects of Hurricane Irene and Tropical Storm Lee on the bed sediment geochemistry of U.S. Atlantic coastal rivers. *Hydrological Processes, 28*(3), 1250-1259. doi: 10.1002/hyp.9635

Hughes, C. P., & Veron, D. E. (2015). Characterization of Low-Level Winds of Southern and Coastal Delaware. *Journal of Applied Meteorology and Climatology, 54*(1), 77-93. doi: 10.1175/jamc-d-14-0011.1

Hunter, J. R., & Hearn, C. J. (1987). Lateral and Vertical Variations in the Wind-Driven Circulation in Long, Shallow Lakes. *J Geophys Res-Oceans, 92*(C12), 13106-13114. doi: DOI 10.1029/JC092iC12p13106

Ianniello, J. P. (1979). Tidally Induced Residual Currents in Estuaries of Variable Breadth and Depth. *J Phys Oceanogr, 9*(5), 962-974. doi: 10.1175/1520-0485(1979)009<0962:TIRCIE>2.0.CO;2

Jackson, N. L. (1995). Wind and Waves - Influence of Local and Nonlocal Waves on Mesoscale Beach Behavior in Estuarine Environments. *Ann Assoc Am Geogr, 85*(1), 21-37.

Jenkins, R. L., III. (2015). *Surface wave analysis based on a hydrodynamic modeling system for the Delaware coastal environment.* (1596864 M.S.), University of Delaware, Ann Arbor. ProQuest Dissertations & Theses Global database.

Johnson, H. K., & Vested, H. J. (1992). Effects of Water Waves on Wind Shear Stress for Current Modeling. *J Atmos Ocean Tech, 9*(6), 850-861. doi: 10.1175/1520-0426(1992)009<0850:Eowwow>2.0.Co;2

Jones, N. L., & Monismith, S. G. (2008). The influence of whitecapping waves on the vertical structure of turbulence in a shallow estuarine embayment. *J Phys Oceanogr, 38*(7), 1563-1580. doi: 10.1175/2007jpo3766.1

Kang, D., & Fringer, O. (2012). Energetics of Barotropic and Baroclinic Tides in the Monterey Bay Area. *J Phys Oceanogr, 42*(2), 272-290. doi: 10.1175/JPO-D-11-039.1

Kenyon, K. (1969). Stokes drift for random gravity waves. *J. Geophys. Res., 74*(28), 6991-6994. doi: 10.1029/JC074i028p06991

Kitaigorodskii, S. A. (1973). *The Physics of Air-sea Interaction*: Israel Program for Scientific Translations.

Knaapen, M. A. F., & Hulscher, S. J. M. H. (2002). Regeneration of sand waves after dredging. *Coastal Engineering, 46*(4), 277-289. doi: https://doi.org/10.1016/S0378-3839(02)00090-X

Komen, G. J., Hasselmann, K., & Hasselmann, K. (1984). On the Existence of a Fully Developed Wind-Sea Spectrum. *Journal of Physical Oceanography, 14*(8), 1271-1285. doi: 10.1175/1520-0485(1984)014<1271:Oteoaf>2.0.Co;2

Kukulka, T., Jenkins, R. L., Kirby, J. T., Shi, F., & Scarborough, R. W. (2017). Surface Wave Dynamics in Delaware Bay and Its Adjacent Coastal Shelf. *Journal of Geophysical Research: Oceans, 122*(11), 8683-8706. doi: 10.1002/2017JC013370

Kumar, N., Voulgaris, G., & Warner, J. C. (2011). Implementation and modification of a three-dimensional radiation stress formulation for surf zone and rip-current applications. *Coastal Engineering, 58*(12), 1097-1117. doi: https://doi.org/10.1016/j.coastaleng.2011.06.009

Kumar, N., Voulgaris, G., Warner, J. C., & Olabarrieta, M. (2012). Implementation of the vortex force formalism in the coupled ocean-atmosphere-wave-sediment transport (COAWST) modeling system for inner shelf and surf zone applications. *Ocean Model. Online, 47*, 65-95. doi: 10.1016/j.ocemod.2012.01.003

Lanzoni, S., & Seminara, G. (1998). On tide propagation in convergent estuaries. *J Geophys Res-Oceans, 103*(C13), 30793-30812. doi: Doi 10.1029/1998jc900015

Large, W. G., & Pond, S. (1981). Open Ocean Momentum Flux Measurements in Moderate to Strong Winds. *J Phys Oceanogr, 11*(3), 324-336. doi: Doi 10.1175/1520-0485(1981)011<0324:Oomfmi>2.0.Co;2

LeBlond, P. H. (1978). On tidal propagation in shallow rivers. *Journal of Geophysical Research: Oceans, 83*(C9), 4717-4721. doi: doi:10.1029/JC083iC09p04717

Lee, S. B., Li, M., & Zhang, F. (2017). Impact of sea level rise on tidal range in Chesapeake and Delaware Bays. *J Geophys Res-Oceans, 122*(5), 3917-3938. doi: 10.1002/2016jc012597

Levin, J., Wilkin, J., Fleming, N., & Zavala-Garay, J. (2018). Mean circulation of the Mid-Atlantic Bight from a climatological data assimilative model. *Ocean Model. Online, 128*, 1-14. doi: https://doi.org/10.1016/j.ocemod.2018.05.003

Levin, P. S., & Möllmann, C. (2015). Marine ecosystem regime shifts: challenges and opportunities for ecosystem-based management. *Philosophical Transactions of the Royal Society B: Biological Sciences, 370*(1659), 20130275. doi: 10.1098/rstb.2013.0275

Li, C. Y., & O'Donnell, J. (2005). The effect of channel length on the residual circulation in tidally dominated channels. *J Phys Oceanogr, 35*(10), 1826-1840. doi: Doi 10.1175/Jpo2804.1

Li, M., Zhong, L., Boicourt, W. C., Zhang, S., & Zhang, D.-L. (2006). Hurricane-induced storm surges, currents and destratification in a semi-enclosed bay. *Geophys Res Lett, 33*(2). doi: doi:10.1029/2005GL024992

Liria, P., Garel, E., & Uriarte, A. (2009). The effects of dredging operations on the hydrodynamics of an ebb tidal delta: Oka Estuary, northern Spain. *Continental Shelf Research, 29*(16), 1983-1994. doi: 10.1016/j.csr.2009.01.014

Longuet-Higgins, M. S., & Stewart, R. w. (1964). Radiation stresses in water waves; a physical discussion, with applications. *Deep Sea Research and Oceanographic Abstracts, 11*(4), 529-562. doi: https://doi.org/10.1016/0011-7471(64)90001-4

Luettich, R. A., Westerink, J. J., & Scheffner, N. W. (1992). ADCIRC: An advanced three-dimensional circulation model for shelves, coasts and estuaries. Report 1: theory and methodology of ADCIRC-2DDI and ADCIRC-3DL *Dredging Research Program. Tehcnical Report DRP-92-6* (pp. 173). Vickburg, Miss: U.S. Army Corps of Engineers.

MacCready, P., Banas, N. S., Hickey, B. M., Dever, E. P., & Liu, Y. G. (2009). A model study of tide- and wind-induced mixing in the Columbia River Estuary and plume. *Continental Shelf Research, 29*(1), 278-291. doi: 10.1016/j.csr.2008.03.015

MacCready, P., & Geyer, W. R. (2010). Advances in Estuarine Physics. *Annual review of marine science, 2*, 35-58. doi: 10.1146/annurev-marine-120308-081015

Madsen, O. S., Poon, Y.-K., & Graber, H. C. (1988). Spectral wave attenuation by bottom friction: theory *Coastal Engineering Proceedings*(21). doi: 10.9753/icce.v21.%p

Marmin, S., Lesueur, P., Dauvin, J. C., Samson, S., Tournier, P., Lavanne, A. G., . . . Thouroude, C. (2016). An experimental study on dredge spoil of estuarine sediments in the bay of seine (France): A morphosedimentary assessment. *Continental Shelf Research, 116*, 89-102. doi: 10.1016/j.csr.2016.01.010

McSweeney, J. M. (2017). *Sediment transport dynamics in Delaware Estuary*. (Ph.D. Thesis), Rutgers University, New Brunswick, NJ. United States. .

McSweeney, J. M., Chant, R. J., & Sommerfield, C. K. (2016a). Lateral variability of sediment transport in the Delaware Estuary. *J Geophys Res-Oceans, 121*(1), 725-744. doi: 10.1002/2015jc010974

McSweeney, J. M., Chant, R. J., Wilkin, J. L., & Sommerfield, C. K. (2016b). Suspended-Sediment Impacts on Light-Limited Productivity in the Delaware Estuary. *Estuar Coast*. doi: 10.1007/s12237-016-0200-3

McWilliams, J. C., Restrepo, J. M., & Lane, E. M. (2004). An asymptotic theory for the interaction of waves and currents in coastal waters. *Journal of Fluid Mechanics, 511*, 135-178. doi: 10.1017/s0022112004009358

Mellor, G. (2010). Wave radiation stress. *Ocean Dynamics, 61*(5), 563-568. doi: 10.1007/s10236-010-0359-2

Monismith, S. G., Kimmerer, W., Burau, J. R., & Stacey, M. T. (2002). Structure and flow-induced variability of the subtidal salinity field in northern San Francisco Bay. *J Phys Oceanogr, 32*(11), 3003-3019. doi: Doi 10.1175/1520-0485(2002)032<3003:Safivo>2.0.Co;2

Morelli, G., & Gasparon, M. (2015). Depositional variability of estuarine intertidal sediments and implications for metal distribution: An example from Moreton Bay (Australia). *Continental Shelf Research, 108*, 41-54. doi: 10.1016/j.csr.2015.07.017

Nash, D. B. (1994). Effective Sediment-Transporting Discharge from Magnitude-Frequency Analysis. *J Geol, 102*(1), 79-95.

Nepf, H. M., & Monismith, S. G. (1991). Experimental-Study of Wave-Induced Longitudinal Vortices. *J Hydraul Eng-Asce, 117*(12), 1639-1649. doi: Doi 10.1061/(Asce)0733-9429(1991)117:12(1639)

Nidzieko, N. J. (2010). Tidal asymmetry in estuaries with mixed semidiurnal/diurnal tides. *J Geophys Res-Oceans, 115*. doi: Artn C08006
10.1029/2009jc005864

Olabarrieta, M., Geyer, W. R., & Kumar, N. (2014). The role of morphology and wave-current interaction at tidal inlets: An idealized modeling analysis. *J Geophys Res-Oceans, 119*(12), 8818-8837. doi: 10.1002/2014jc010191

Olabarrieta, M., Warner, J. C., Armstrong, B., Zambon, J. B., & He, R. Y. (2012). Ocean-atmosphere dynamics during Hurricane Ida and Nor'Ida: An application of the coupled ocean-atmosphere-wave-sediment transport (COAWST) modeling system. *Ocean Model. Online, 43-44*, 112-137. doi: 10.1016/j.ocemod.2011.12.008

Olabarrieta, M., Warner, J. C., & Kumar, N. (2011). Wave-current interaction in Willapa Bay. *J Geophys Res-Oceans, 116*. doi: Artn C12014
10.1029/2011jc007387

Oliveira, A., Fortunato, A. B., & Rego, J. R. L. (2006). Effect of morphological changes on the hydrodynamics and flushing properties of the Obidos lagoon (Portugal). *Continental Shelf Research, 26*(8), 917-942. doi: 10.1016/j.csr.2006.02.011

Oost, W. A., Komen, G. J., Jacobs, C. M. J., & Van Oort, C. (2002). New evidence for a relation between wind stress and wave age from measurements during ASGAMAGE. *Boundary-Layer Meteorology, 103*(3), 409-438. doi: 10.1023/A:1014913624535

Ortiz-Suslow, D. G., Haus, B. K., Williams, N. J., Laxague, N. J. M., Reniers, A. J. H. M., & Graber, H. C. (2015). The spatial-temporal variability of air-sea momentum fluxes

observed at a tidal inlet. *J Geophys Res-Oceans, 120*(2), 660-676. doi: 10.1002/2014jc010412

Orton, P. M., Conticello, F. R., Cioffi, F., Hall, T. M., Georgas, N., Lall, U., . . . MacManus, K. (2018). Flood hazard assessment from storm tides, rain and sea level rise for a tidal river estuary. *Nat. Hazards*. doi: 10.1007/s11069-018-3251-x

Parker, B. (1984). *Frictional Effects On Tidal Dynamics of Shallow Estuary*. (Ph.D.), Johns Hopkins University.

Parker, B. (1991). The relative importance of the various nonlinear mechanisms in a wide range of tidal interactions (review). In B. Parker (Ed.), *Tidal Hydrodynamics* (pp. 237-268). United States: John Wiley & Sons.

Perrie, W., Tang, C. L., Hu, Y., & DeTracy, B. M. (2003). The impact of waves on surface currents. *J Phys Oceanogr, 33*(10), 2126-2140. doi: Doi 10.1175/1520-0485(2003)033<2126:Tiowos>2.0.Co;2

Pritchard, D. W. (1956). The dynamic structure of a coastal plain estuary. *J. Mar. Res., 13*, 133-144.

Ralston, D. K., & Geyer, W. R. (2019). Response to channel deepening of the salinity intrusion, estuarine circulation, and stratification in an urbanized estuary. *Journal of Geophysical Research: Oceans, 0*(ja). doi: 10.1029/2019jc015006

Ralston, D. K., Geyer, W. R., & Lerczak, J. A. (2008). Subtidal salinity and velocity in the Hudson River estuary: Observations and modeling. *J Phys Oceanogr, 38*(4), 753-770. doi: 10.1175/2007jpo3808.1

Ralston, D. K., Geyer, W. R., & Warner, J. C. (2012). Bathymetric controls on sediment transport in the Hudson River estuary: Lateral asymmetry and frontal trapping. *J Geophys Res-Oceans, 117*. doi: Artn C10013
10.1029/2012jc008124

Ralston, D. K., Talke, S., Geyer, W. R., Al-Zubaidi, H. A. M., & Sommerfield, C. K. (2019). Bigger Tides, Less Flooding: Effects of Dredging on Barotropic Dynamics in a Highly Modified Estuary. *Journal of Geophysical Research: Oceans, 0*(0). doi: doi:10.1029/2018JC014313

Rogers, J. S., Monismith, S. G., Fringer, O. B., Koweek, D. A., & Dunbar, R. B. (2017). A coupled wave-hydrodynamic model of an atoll with high friction: Mechanisms for flow, connectivity, and ecological implications. *Ocean Modelling, 110*, 66-82. doi: 10.1016/j.ocemod.2016.12.012

Sanay, R., & Valle-Levinson, A. (2005). Wind-induced circulation in semienclosed homogeneous, rotating basins. *J Phys Oceanogr, 35*(12), 2520-2531. doi: Doi 10.1175/Jpo2831.1

Savenije, H. H. G., Toffolon, M., Haas, J., & Veling, E. J. M. (2008). Analytical description of tidal dynamics in convergent estuaries. *J Geophys Res-Oceans, 113*(C10). doi: Artn C10025
10.1029/2007jc004408

Savtchenko, A., Tang, S., Barber, R., & Wu, J. (1999). Air-sea interaction processes at light winds observed from a coastal tower. *Journal of Coastal Research, 15*(2), 444-456.

Scully, M. E., Friedrichs, C., & Brubaker, J. (2005). Control of estuarine stratification and mixing by wind-induced straining of the estuarine density field. *Estuaries, 28*(3), 321-326. doi: Doi 10.1007/Bf02693915

Scully, M. E., Geyer, W. R., & Lerczak, J. A. (2009). The Influence of Lateral Advection on the Residual Estuarine Circulation: A Numerical Modeling Study of the Hudson River Estuary. *J Phys Oceanogr, 39*(1), 107-124. doi: 10.1175/2008jpo3952.1

Scully, M. E., Trowbridge, J. H., Sherwood, C. R., Jones, K. R., & Traykovski, P. (2018). Direct Measurements of Mean Reynolds Stress and Ripple Roughness in the Presence of Energetic Forcing by Surface Waves. *Journal of Geophysical Research: Oceans, 123*(4), 2494-2512. doi: 10.1002/2017JC013252

Senior, A., & Green, M. O. (2002). Assessing human impacts on estuaries: it's a risky business. *Water & Atmosphere, 10*(2), 18-19.

Shapiro, R. (1970). Smoothing, filtering, and boundary effects. *Rev Geophys, 8*(2), 359-387. doi: 10.1029/RG008i002p00359

Shchepetkin, A. F., & McWilliams, J. C. (2005). The regional oceanic modeling system (ROMS): a split-explicit, free-surface, topography-following-coordinate oceanic model. *Ocean Model. Online, 9*(4), 347-404. doi: https://doi.org/10.1016/j.ocemod.2004.08.002

Signell, R. P., Beardsley, R. C., Graber, H. C., & Capotondi, A. (1990). Effect of Wave-Current Interaction on Wind-Driven Circulation in Narrow, Shallow Embayments. *J Geophys Res-Oceans, 95*(C6), 9671-9678. doi: DOI 10.1029/JC095iC06p09671

Signell, R. P., & List, J. H. (1997). Effect of wave-enhanced bottom friction on storm-driven circulation in Massachusetts Bay. *J Waterw Port C-Asce, 123*(5), 233-239. doi: Doi 10.1061/(Asce)0733-950x(1997)123:5(233)

Snyder, R. L., Dobson, F. W., Elliott, J. A., & Long, R. B. (1981). Array measurements of atmospheric pressure fluctuations above surface gravity waves. *J Fluid Mech, 102*, 1-59. doi: 10.1017/S0022112081002528

Sommerfield, C. K., & Wong, K.-C. (2011). Mechanisms of sediment flux and turbidity maintenance in the Delaware Estuary. *J. Geophys. Res., 116*(C1). doi: 10.1029/2010jc006462

Speer, P. E., & Aubrey, D. G. (1985). A Study of Non-Linear Tidal Propagation in Shallow Inlet Estuarine Systems .2. Theory. *Estuar Coast Shelf S, 21*(2), 207-224. doi: Doi 10.1016/0272-7714(85)90097-6

Stacey, M. W., & Valle-Levinson, A. (2006). Simulation and energy partition of the flow through Paso Galvarino, Chile. *J. Mar. Res., 64*(2), 249-266. doi: Doi 10.1357/002224006777606470

Styles, R., & Glenn, S. M. (2000). Modeling stratified wave and current bottom boundary layers on the continental shelf. *J Geophys Res-Oceans, 105*(C10), 24119-24139. doi: Doi 10.1029/2000jc900115

Styles, R., & Glenn, S. M. (2002). Modeling bottom roughness in the presence of wave-generated ripples. *J Geophys Res-Oceans, 107*(C8). doi: Artn 3110
10.1029/2001jc000864

Sullivan, P. P., Mcwilliams, J. C., & Melville, W. K. (2007). Surface gravity wave effects in the oceanic boundary layer: large-eddy simulation with vortex force and stochastic breakers. *J Fluid Mech, 593*, 405-452. doi: 10.1017/S002211200700897x

Talke, S. A., & Jay, D. A. (2017). Archival Water-Level Measurements: Recovering Historical Data to Help Design for the Future. *Civil and Environmental Engineering Faculty Publications and Presentations, 412*. doi: https://pdxscholar.library.pdx.edu/cengin_fac/412

Talke, S. A., Orton, P., & Jay, D. A. (2014). Increasing storm tides in New York Harbor, 1844–2013. *Geophys Res Lett, 41*(9), 3149-3155. doi: doi:10.1002/2014GL059574

Taylor, P. K., & Yelland, M. J. (2001). The dependence of sea surface roughness on the height and steepness of the waves. *J Phys Oceanogr, 31*(2), 572-590. doi: Doi 10.1175/1520-0485(2001)031<0572:Tdossr>2.0.Co;2

Thornton, E. B., & Guza, R. T. (1983). Transformation of Wave Height Distribution. *J Geophys Res-Oceans, 88*(Nc10), 5925-5938. doi: DOI 10.1029/JC088iC10p05925

Uchiyama, Y., McWilliams, J. C., & Shchepetkin, A. F. (2010). Wave-current interaction in an oceanic circulation model with a vortex-force formalism: Application to the surf zone. *Ocean Model. Online, 34*(1-2), 16-35. doi: 10.1016/j.ocemod.2010.04.002

Valle-Levinson, A. (2011). Large Estuaries (Effects of Rotation). *Treatise on Estuarine and Coastal Science, Vol 2: Water and Fine Sediment Circulation*, 123-140.

Valle-Levinson, A., Reyes, C., & Sanay, R. (2003). Effects of bathymetry, friction, and rotation on estuary-ocean exchange. *J Phys Oceanogr, 33*(11), 2375-2393. doi: Doi 10.1175/1520-0485(2003)033<2375:Eobfar>2.0.Co;2

van Maren, D. S., van Kessel, T., Cronin, K., & Sittoni, L. (2015). The impact of channel deepening and dredging on estuarine sediment concentration. *Continental Shelf Research, 95*, 1-14. doi: 10.1016/j.csr.2014.12.010

van Rijn, L., & Grasmeijer, B. (2018). Effect of channel deepening on tidal flow and sediment transport—part II: muddy channels. *Ocean Dynamics, 68*(11), 1481-1501. doi: 10.1007/s10236-018-1205-1

van Rijn, L., Grasmeijer, B., & Perk, L. (2018). Effect of channel deepening on tidal flow and sediment transport: part I—sandy channels. *Ocean Dynamics, 68*(11), 1457-1479. doi: 10.1007/s10236-018-1204-2

Wallace, R. B., Baumann, H., Grear, J. S., Aller, R. C., & Gobler, C. J. (2014). Coastal ocean acidification: The other eutrophication problem. *Estuar. Coast. Shelf Sci., 148*, 1-13. doi: http://dx.doi.org/10.1016/j.ecss.2014.05.027

Walters, R. A. (1997). A model study of tidal and residual flow in Delaware Bay and River. *Journal of Geophysical Research: Oceans, 102*(C6), 12689-12704. doi: 10.1029/97JC00612

Wang, X. H., Wang, D. P., Sun, Z. L., He, Z. G., Liu, H. J., Guan, W. B., . . . Zhu, J. R. (2016). International scientists discuss impact on China's estuarine and coastal environment by intensive anthropogenic activities - The 2nd workshop on sediment dynamics of muddy coasts and estuaries: Physics, biology and their interactions, Zhoushan, China, 23-26 October, 2015. *Estuar Coast Shelf S, 168*, Ii-Iii. doi: 10.1016/S0272-7714(15)00342-X

Wang, Z. B., Van Maren, D. S., Ding, P. X., Yang, S. L., Van Prooijen, B. C., De Vet, P. L. M., . . . He, Q. (2015). Human impacts on morphodynamic thresholds in estuarine systems. *Continental Shelf Research, 111*, 174-183. doi: 10.1016/j.csr.2015.08.009

Wargula, A., Raubenheimer, B., & Elgar, S. (2014). Wave-driven along-channel subtidal flows in a well-mixed ocean inlet. *Journal of Geophysical Research: Oceans, 119*(5), 2987-3001. doi: 10.1002/2014JC009839

Warner, J. C., Armstrong, B., He, R. Y., & Zambon, J. B. (2010). Development of a Coupled Ocean-Atmosphere-Wave-Sediment Transport (COAWST) Modeling System. *Ocean Model. Online, 35*(3), 230-244. doi: 10.1016/j.ocemod.2010.07.010

Warner, J. C., Sherwood, C. R., Arango, H. G., & Signell, R. P. (2005). Performance of four turbulence closure models implemented using a generic length scale method. *Ocean Model. Online, 8*(1), 81-113. doi: https://doi.org/10.1016/j.ocemod.2003.12.003

Warner, J. C., Sherwood, C. R., Signell, R. P., Harris, C. K., & Arango, H. G. (2008). Development of a three-dimensional, regional, coupled wave, current, and sediment-transport model. *Comput Geosci-Uk, 34*(10), 1284-1306. doi: 10.1016/j.cageo.2008.02.012

Waters, C. N., Zalasiewicz, J., Summerhayes, C., Barnosky, A. D., Poirier, C., Galuszka, A., . . . Wolfe, A. P. (2016). The Anthropocene is functionally and stratigraphically distinct from the Holocene. *Science, 351*(6269), 137-+. doi: 10.1126/science.aad2622

Wheeler, W. H. (1893). *Tidal rivers; their (1) hydraulics, (2) improvement, (3) navigation*. London, New York: Longmans, Green & Co.

Whitney, M. M., & Codiga, D. L. (2011). Response of a Large Stratified Estuary to Wind Events: Observations, Simulations, and Theory for Long Island Sound. *J Phys Oceanogr, 41*(7), 1308-1327. doi: 10.1175/2011jpo4552.1

Winant, C. D. (2008). Three-dimensional residual tidal circulation in an elongated, rotating basin. *J Phys Oceanogr, 38*(6), 1278-1295. doi: 10.1175/2007jpo3819.1

Wong, K. C., & Garvine, R. W. (1984). Observations of wind-induced, subtidal variability in the Delaware estuary. *Journal of Geophysical Research: Oceans, 89*(C6), 10589-10597. doi: 10.1029/JC089iC06p10589

Wu, J. (1982). Wind-Stress Coefficients over Sea-Surface from Breeze to Hurricane. *J Geophys Res-Oceans, 87*(Nc12), 9704-9706. doi: DOI 10.1029/JC087iC12p09704

Zhong, L., & Li, M. (2006). Tidal energy fluxes and dissipation in the Chesapeake Bay. *Continental Shelf Research, 26*(6), 752-770. doi: https://doi.org/10.1016/j.csr.2006.02.006

Zhu, J., Weisberg, R. H., Zheng, L. Y., & Han, S. Z. (2015). Influences of Channel Deepening and Widening on the Tidal and Nontidal Circulations of Tampa Bay. *Estuar Coast, 38*(1), 132-150. doi: 10.1007/s12237-014-9815-4